Sessile drops, interfaces, and fluid walls: microfluidic approaches to studying single cells

Joseph A. E. Morgan

St. Peter's College

University of Oxford

Thesis submitted for the degree of:

Doctor of Philosophy in Engineering Science

Academic supervisors

Prof. Edmond J. Walsh

Prof. Alfonso A. Castrejón-Pita

Michaelmas 2025

Table of Contents

Abstract

Microfluidic technologies are advancing rapidly and have been implemented across a wide range of biological applications, offering reduced reagent consumption, high-throughput screening, and *in vitro* modelling of cellular microenvironments. These systems have provided valuable insights into cellular behaviour and processes, yet adoption of microfluidic technologies by biologists remains limited. This is commonly attributed to complex device fabrication methods and restricted access to cells within enclosed microchannels. A promising new method to overcome these limitations is to replace solid plastic walls with fluid-fluid interfaces. In this approach, microfluidic environments are fabricated using cell-culture medium and immiscible oil, with the oil-medium interface forming fluid walls which confine the medium to any two-dimensional pattern. Such environments are fabricated in seconds within standard tissue-cultureware and are fully accessible through fluid-fluid interfaces. However, this presents significant engineering challenges; 1) interface curvatures and heights change in response to local pressures and volumes; 2) dynamic interfacial tension associated with adsorption and desorption of amphiphilic molecules to interfaces; 3) the need to create microchambers to isolate cells of interest. Combined, these challenges make characterisation and operation of fluid-walled microfluidics inherently complex.

This thesis investigates both static and dynamic microfluidic systems with fluid walls and explores applications in single-cell isolation and manipulation. First, use of a static system – a sessile drop – is developed and validated as a method to confirm monoclonality within a single-cell cloning workflow. Next, fluid walls are used to connect two drops (chambers) via a conduit to form a ‘dumbbell.’ This established design is applied to model metastasis of cancer cells as they are introduced to one chamber and their migration to the other is quantified. Fluid walls are reconfigured to isolate and retrieve the most migratory cells and machine learning is used to assess cell morphology during migration. Finally, the influence of dynamic changes in oil-medium interfacial tension on flow rates and equilibration times between connected chambers is characterised to provide a model to predict fluid-walled chamber behaviour with biological fluids. Together, this work broadens the possible applications of microfluidics with fluid walls and enhances understanding of the dynamic behaviour of such systems.

Acknowledgements

I am incredibly grateful to all those who have supported me over the past four years. The work in this thesis was made possible through their collective guidance and encouragement, for which I am truly thankful.

First and foremost, I would like to thank Prof. Edmond Walsh for his supervision. I am immensely grateful for his guidance and for making this research possible. I thank him for his invaluable mentorship and for teaching me to ask the right questions – I am incredibly fortunate to have had him as my supervisor.

I would also like to thank Prof. Alfonso Castrejón-Pita, my second supervisor, for his support and kindness over the past four years. I am very grateful for the opportunity to have been part of his research group; I thank him for his guidance and for being so welcoming.

Next, I would like to thank Prof. Peter Cook for hosting me in his lab in the Dunn School for the first three years of my research, for our many discussions and for teaching me what it means to be a scientist. I am also grateful to my fantastic colleagues and lab mates over the years – Federico, Alexi, Cristian and Cyril – for their support and good times both in and out of the lab.

I would like to thank my collaborators in Botnar – Dan, Claire and Rao – without whom this work would not have been possible. I am also grateful to everyone at iota sciences for their support, especially Bob, Ann Na, and Alex. I would also like to thank all my other collaborators, in particular Ricardo, Akansha, Charmaine and Aishwarya.

I am incredibly grateful to all my friends in Oxford and beyond who have supported and encouraged me over the past four years. In particular, Vik and Jake for being the best housemates I could have asked for. Also, thanks to James, the Pembroke gang, all my friends from St. Peter's MCR, and everyone else who supported me along the way. Special thanks also go to the boys – Giannos, Aled, Matt, Sam, Cass, Pegler, Chris, and the staff at Solomon's grill – for all the memories over the past four years. Most of all, thank you to Katie, for always encouraging me to keep going, for putting up with my many late nights at the lab, and for all the happiness along the way.

Finally, thank you to my family – Mum, Dad, Rhiannon and Thisbe – for their constant encouragement, unwavering support, and for always cheering me on.

Chapter 1: Introduction

Advances in microfluidic technologies have transformed many areas of biological research, enabling investigation of cellular processes at single-cell resolution and supporting the development of physiologically relevant *in vitro* models of cellular microenvironments [1]. Their advantages, including reduced reagent consumption, high throughput screening, and the ability of generate precise spatial and temporal gradients – have made microfluidics a powerful tool in modern experimental biology. This has been particularly impactful in the era of single-cell analysis. The rapid expansion of single-cell omics has created a high demand for technologies that facilitate reliable isolation, manipulation, and characterisation of single cells [2]. Microfluidic systems are ideally suited to enabling these advances and have become integral to many such workflows [3].

Despite these advantages, widespread adoption of microfluidic systems by biologists remains limited. This has been attributed to restricted access to cells and reagents enclosed within solid-walled microchannels, and concerns arising from the biocompatibility of polydimethylsiloxane (PDMS) – widely used in device fabrication [4]. Furthermore, while commercially available chips have improved the accessibility of microfluidics, fabrication of custom devices typically relies on complex lithography-based techniques, which may present a barrier to adoption by biologists. Closing the gap between engineering-driven microfluidic device design and the practical requirements of biologists therefore remains a well-recognised challenge [5].

In response, there has been growing interest in open microfluidics, in which at least one boundary is replaced by a fluid interface. The exposed interface provides direct access to cells and reagents, facilitates gas exchange, and mitigates bubble formation – a common issue in conventional microfluidics [6]. Although open microfluidics addresses some of the limitations associated with traditional devices, many platforms still depend on complex lithographic fabrication techniques, specialised surface patterning, or continued use of PDMS [7], [8], [9]

To overcome some of the remaining obstacles, a new class of microfluidics has emerged whereby solid plastic walls are replaced with continuous fluid-fluid interfaces. This technology, pioneered by Walsh et al. [10], exploits immiscible fluid-fluid interfaces to define microfluidic features. Microenvironments are formed directly within standard tissue culture-ware using only cell-culture medium overlaid with the immiscible and bio-inert fluorocarbon oil, FC40. The oil-medium interface creates 'fluid walls' that confine the medium to any two-dimensional design. Fluid walls enable unrestricted access to cells, eliminates the need for PDMS-based materials, and allow microenvironments to be reconfigured during experiments by creating new fluid walls [11]. Fully accessible microenvironments with fluid walls are made in seconds within standard tissue-cultureware, thereby offering biologists an appealing alternative to conventional solid-walled microfluidic chips which may impose practical constraints.

Microfluidics with fluid walls have been applied across an increasingly diverse range of biological workflows in recent years, including single-cell cloning, assaying macrophage chemotaxis, and culturing human neuronal circuits [12], [13], [14]. However, replacing solid plastic walls with fluid-fluid interfaces presents engineering challenges not encountered in conventional microfluidics. While pinned to the underlying substrate, fluid interfaces are free to deform in response to local changes in volume and pressure, complicating flow characterisation. As the biological applications of fluid walls expand, there is increasing need to deepen understanding of the behaviour and limitations of fluid-walled systems. While there has been significant progress in characterising these systems in recent years [15], [16], substantial opportunities remain to refine understanding of their dynamics and operational constraints.

This thesis investigates the characteristics of microfluidic systems with fluid walls, advancing understanding of their behaviour while demonstrating applications in single-cell isolation and manipulation. First, a static fluidic system – a sessile drop – is studied, and the strong optical properties of drops with low contact angles is exploited to verify monoclonality within a single-cell cloning workflow. Next, fluid walls are used to connect two drops

(chambers) via a conduit, creating a dynamic system. This configuration, which has been useful in previous biological studies [13], [14], is applied here to study cancer cell migration as cells migrate from one chamber to the other, and the reconfigurability of fluid walls is harnessed to isolate and retrieve the most migratory cells. Finally, the effect of protein adsorption to the oil-medium interface is investigated. The influence of adsorption-induced changes in interfacial tension on flow between interconnected fluid-walled chambers is quantified and incorporated into a predictive model for system behaviour. Together, this work provides researchers with tools to design new fluid-walled microfluidic systems, expands their potential applications, and advances understanding of their dynamic behaviour.

Objectives

This thesis addresses the following objectives:

1. Develop a static microfluidic method using sessile drops to verify monoclonality within a single-cell cloning workflow and validate this technique by comparing cloning efficiencies across multiple cell types.
2. Develop a dynamic fluid-walled microfluidic platform using dumbbell-shaped arrangements to study cancer cell migration and metastatic processes.
3. Establish a method to isolate and pick single cells from chambers with fluid walls for downstream analysis.
4. Investigate how dynamic changes in interfacial tension influence flow in fluid-walled microfluidics. Develop and validate a predictive model describing the impact on evolving chamber heights within dumbbells with fluid walls.

This thesis comprises 6 chapters that address each of the outlined objectives with a concluding chapter that discusses the work, relates it to each of the objectives, and outlines potential directions for future research.

Chapter 2 provides a brief literature review, beginning with an overview of the origins and evolution of microfluidic technologies and the key advantages and challenges associated with

traditional systems, with particular emphasis on single-cell manipulation. This provides context for the development of open microfluidic approaches that ultimately lead to the introduction of microfluidics with fluid walls.

Chapter 3 demonstrates how the simplest static microfluidic environment – a sessile drop – can be leveraged to verify monoclonality within a single-cell cloning workflow. By imaging cells within drops with low contact angles deposited in microtiter wells, users know with certainty if a well contains a single cell. The biocompatibility of the technique is verified by comparing cloning efficiencies across multiple cell types, including induced pluripotent stem cells. This work is published in *Biotechnology and Bioengineering*.

Chapter 4 presents a microfluidic platform with fluid walls for studying cancer cell migration. Two microfluidic chambers are connected by a thin fluid conduit forming a dumbbell shape. Cancer cells are infused into one chamber and a chemoattractant into the other, and their migration quantified. Fluid walls are then reconfigured to isolate the most migratory cells, and a method to reliably pick cells from fluid-walled chambers is developed. In addition, the excellent optics of fluid walls enables the use of machine-learning approaches to track changes in cell morphology during migration.

Chapter 5 investigates how dynamic changes in interfacial tension influence the equilibration behaviour of a dumbbell with fluid walls. Connected chambers equilibrate to different heights despite having identical footprints, attributed to spatial and temporal variations in interfacial tension as their interfaces expand and contract. A semi-analytical model describing flow between connected drops is developed and validated through a combination of microfluidic experiments and interfacial tension measurements.

Chapter 6 provides a discussion of the findings presented in the thesis, outlining how each of the objectives has been addressed, evaluating the advantages and limitations of the work, and proposed future research.

List of publications

The work presented in this thesis resulted in the following papers in press:

- **Morgan, J.A.E.**, Cook, P.R., Castrejón-Pita, A.A., and Walsh, E.J. (2025). Generation of clonal cultures of adherent or suspension cells using flat sessile drops for assurance of monoclonality. Biotechnology and Bioengineering, 122: 2739-2750.
- Nebuloni, F., **Morgan, J.A.E.**, Walsh, E.J., and Cook, P.R. (2023). A platform for modular assembly and feeding of micro-organoids on standard Petri dishes. Biology Open 12(5). (Not included for assessment in this thesis).

In addition, the papers presented in Chapters 4 and 5 are being prepared for submission:

- **Morgan, J.A.E.**, Cotton, D.T., Rao, S.R., Cook, P.R., Edwards, J.R., Castrejón-Pita, A.A., Edwards, C.M., and Walsh E.J. Identification and isolation of migratory subpopulations of cancer cells using microfluidics with fluid walls.
- **Morgan, J.A.E.**, Nebuloni, F., Cook, P.R., Castrejón-Pita, A.A., and Walsh, E.J. Dynamic interfacial tension effects in microfluidics with fluid walls.

Chapter 2: Literature Review

An introduction to microfluidics

Microfluidics is the science and technology of manipulating fluids at the micro- and nanoscale. The origins of microfluidics are closely tied to the broader development of microscale technologies, with the first practical implementations appearing in the 1980s through the development of microelectromechanical systems (MEMS) [17], [18]. Techniques developed in the fabrication of these devices paved the way for many of the methods widely adopted for microfluidic chip manufacture today [19]. Progress in microfluidics followed two major trajectories. The first was industry-driven, focusing on fluid management for analytical instruments, fluid jets and sprays, and inkjet printing [20]. The second centred on controlling fluid in microchannels for chemical and biological applications, enabling advances in gas chromatography, pathogen detection, and single-cell analysis [21], [22], [23]. Transitioning to the microscale provides significant benefits: reduced reagent consumption, lower cost, and shorter transport distances [24].

Consideration of the principles governing fluid behaviour highlights key differences between macro- and microscale flows. First, Reynolds Numbers, which represent the ratio between inertial and viscous forces ($Re = \frac{\rho v L}{\mu}$ where ρ is the fluid density, v velocity, L length scale – often hydraulic diameter of a microchannel – and μ the dynamic viscosity), are typically well below the turbulent threshold ($Re \ll 2300$), ensuring that viscous forces dominate inertial, and flow remains laminar [25]. Second, the small characteristic dimensions of microfluidic devices cause capillary forces to outweigh gravitational [26]. The combination of a laminar flow and low Bond number – the ratio between gravitational and capillary forces ($Bo = \frac{\Delta\rho g L^2}{\gamma}$ where $\Delta\rho$ is the density difference between phases, g gravitational acceleration, L length scale – for example the radius of curvature of a drop – and γ the interfacial tension) – results in predictable, stable flow profiles, giving users precise control over fluid manipulation.

These flow characteristics are exploited in *continuous-flow microfluidics*, where fluids move through microchannels without breaking continuity (**Figure 1A** [27]). At the low Reynolds numbers typical of these systems, the absence of hydrodynamic instability means that mixing occurs solely through molecular diffusion [28]. Continuous-flow circuits are widely used for cell perfusion, where low shear stress and solute diffusion are advantageous [29]. Another prominent microfluidic technique uses immiscible phases to divide streams into discrete drops (**Figure 1B** [30]), up to 20,000 drops per second [31]. Droplet microfluidics enables a large number of reactions without a concomitant increase in device complexity. Droplets function as discrete units, enabling parallel experiments and are used in diverse applications including chemical synthesis, droplet-based polymerase chain reaction (PCR), and single-cell isolation [32]. Further developments include *digital microfluidics* (**Figure 1C** [33]), where applied voltages modulate surface wettability (electrowetting) to move drops across surfaces [34].

The integration and miniaturisation of multiple lab process onto a single chip, referred to as Lab-on-a-Chip (LoC), is a leading area of microfluidic research. LoCs are a subcategory of MEMS, often described as micro total analysis systems (μTAS) and are used in a variety of applications including DNA/RNA detection and amplification, single-cell analysis and omics [35]. A specialised class of LoC systems, known as Organ-on-a-chip (**Figure 1D** [36]), aims to recreate physiological environments *in vitro* by mimicking tissue interfaces and mechanical interactions at the cellular level [37], Organ-on-a-chip platforms aim to better approximate human organ physiology, reducing reliance on animal testing and improving drug development pipelines [38].

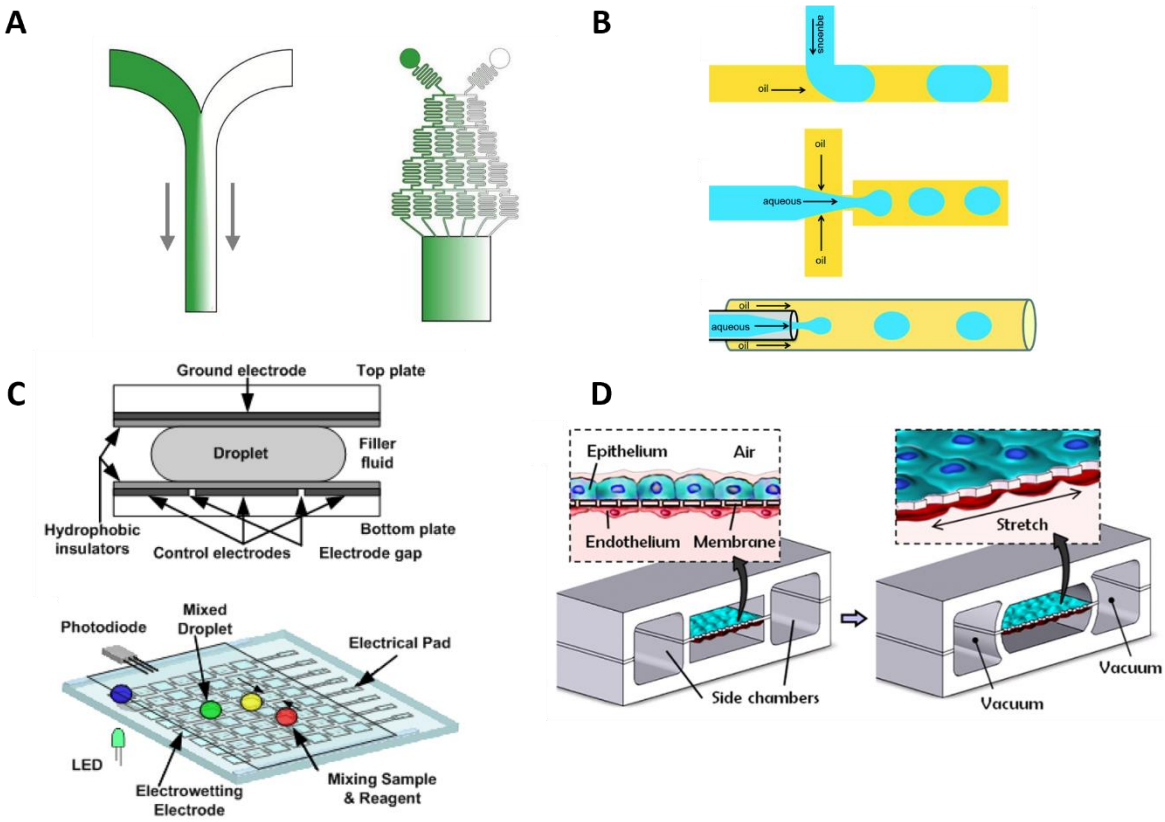

Figure 1. An overview of microfluidic methods and technologies. (A) An example of continuous flow microfluidics. One relatively simple and once more complex configuration used to obtain a gradient between two fluids (green and white) [27]. **(B)** Droplet microfluidics. Three common methods using immiscible phases to pinch a continuous fluid stream into discrete drops [30]. **(C)** A digital microfluidic platform where electrowetting is used to manipulate fluid drops [33]. **(D)** An example of an organ-on-a-chip, designed to mimic the alveolar-capillary interface in the lung (lung-on-a-chip [36]).

Microfluidic chip fabrication methods

Photolithography has been fundamental to the development of microfluidics, using light to produce patterned thin films on a substrate. In this process, a photoresist-coated substrate is exposed through a mask containing a desired geometric design, transferring that pattern to the photoresist and the underlying substrate [39]. Photolithography offers exceptional precision, enabling feature sizes in the micron to sub-micron range [40]. Soft lithography – an extension of photolithography – uses elastomeric materials such as polydimethylsiloxane (PDMS), commonly used in the fabrication of microfluidic devices due to its low cost, optical transparency, gas permeability, and thermosetting properties [41]. After a pattern is defined

using conventional photolithography, a master is produced, from which PDMS moulds can be cast and peeled to create microfluidic channels (**Figure 2A** [42]).

Etching techniques are also widely used and are categorised as wet or dry etching. In wet etching, material is chemically removed by immersing the substrate in a corrosive solution, while a hydrophobic mask protects regions to create the pattern. Dry etching removes material using gases or high-energy ion beams and is more commonly used for silicon and glass microfluidic chips [43]. Another method is micro-milling, whereby high-speed drill bits are used to fabricate 3D structures from a wide range of materials, with resolutions typically around 2 µm (**Figure 2B** [44]). However, micro-milling offers comparatively poor minimum feature size compared to lithographic methods, and tool vibrations can reduce precision and make sharp corners difficult to achieve [45] . While these conventional approaches remain popular, more recent fabrication strategies involving 3D printing and hybrid manufacturing are increasingly being introduced to improve scalability, resolution, reduce cost, and support rapid prototyping [46].

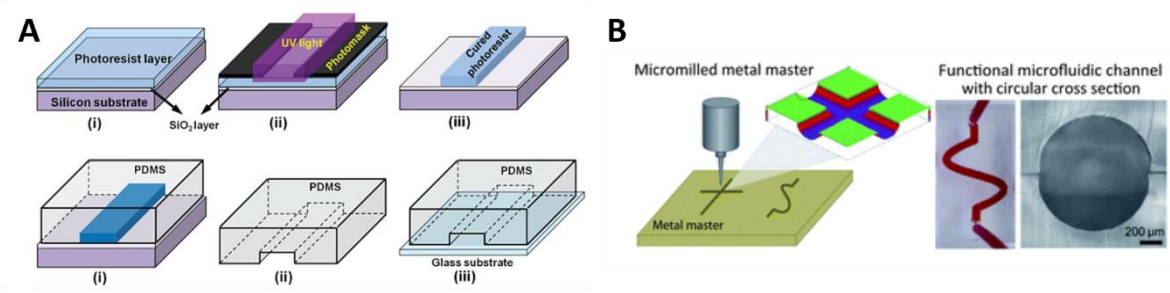

Figure 2. Examples of established microfluidic fabrication methods. (A) Soft lithography is one of the most widely used fabrication methods for microfluidic systems [42]. **(B)** Micro-milling is also used to create microchannels, an can be combined with other methods [44].

Conventional and microfluidic approaches to single-cell isolation

Isolation of single cells from a heterogenous population is a crucial step in many biological workflows, including gene-editing, stem-cell therapies, and the production of monoclonal antibodies [47]. The demand for efficient single-cell isolation has driven the development of a wide range of technologies, including microfluidics.

A standard method is through limiting dilution: a cell suspension is serially diluted and then aliquoted into multiple wells such that each dispensed volume is likely to contain < 1 cell [48] (**Figure 3A**). This is a statistical method and offers no guarantee that an aliquot contains exactly one cell, motivating more controlled isolation strategies [49]. Micromanipulation – using micropipettes mounted on mechanical stages – enables manual selection of single cells [50], or cloning rings can be used to provide a physical barrier to isolate a cell from a surrounding population. While both methods are effective for generating clonal cultures, they are low throughput and require skilled operators [51]. For applications requiring higher throughput and single-cell resolution – for example, when separating single cells into distinct subgroups – automated methods are commonly used. One of the most established methods is fluorescence-activated cell sorting (FACS), whereby cells are confined within droplets and an electric field used to deflect droplets based on fluorescent markers (**Figure 3B** [52]), achieving processing rates up to 70,000 events per second [53] though the high flow rate and shear stresses can compromise viability of isolated cells. Furthermore, downstream processing and verification is typically required to establish monoclonal cultures.

Microfluidic approaches offer alternative strategies for single-cell isolation, generally falling into two broad categories: droplet microfluidics and microfluidic cell trapping. In droplet-based approaches, individual cells are encapsulated within immiscible droplets that act as independent microreactors (**Figure 3C** [54]). Cell-trapping devices use hydrodynamic forces and micro-barriers to capture single cells for downstream analysis [55] [56]. Although current techniques improve throughput and control, many still rely on complex instrumentation and high operating costs. As a result, ongoing research focuses on simpler and more accessible single-cell isolation platforms.

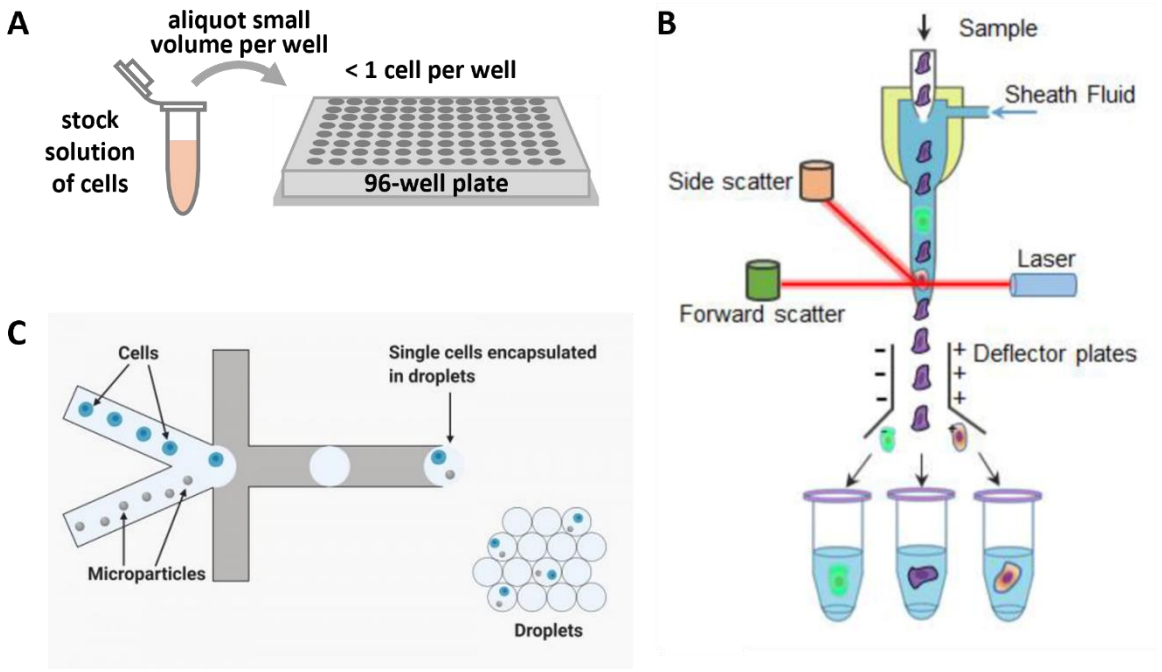

Figure 3. Methods of obtaining an isolated single cell. (A) Limiting dilution is commonly used to obtain a single cell. A stock solution is aliquoted across a microtiter plate such that each well is likely to contain less than one cell. **(B)** Fluorescence activated cell sorting (FACS) achieves high throughput sorting of single cells based on the presence of a fluorescent marker [52]. **(C)** Droplet-based microfluidic systems confine single cells to discrete drops [54].

Open microfluidics

A frequently cited limitation of traditional microfluidic systems is that they are typically sealed within polymeric chips, restricting access to cells or reagents during experiments. This has motivated the development of open-microfluidics (OM), in which at least one boundary of a channel or chamber is exposed or comprises a fluid interface [57] (**Figure 4A** [58]**, B** [59]). Such open interfaces enable direct manipulation of contents, facilitate exchange of liquids and gases, and reduce the effects of bubble entrapment [60]. As a result, OM platforms have been adopted in a wide range of biological applications, including cell migration assays [61], [62] and the fabrication of 3D tissue models (**Figure 4C** [63]), offering enhanced access to microenvironments over conventional sealed microfluidic devices. Furthermore, the exposed interface enables flow within OM systems to be driven by surface tension, often referred to as ‘passive pumping’, eliminating the need for external pumps [64], [65]. However, many OM systems are still PDMS-based, or require complex surface patterning steps and fabrication

methods [8], [66], [67]. Although PDMS remains one of the most widely used materials in the fabrication of microfluidic systems, adsorption of small molecules and leaching of uncured oligomers can interfere with sensitive biological assays. Regehr et al. [4] investigated potential artefacts in PDMS-based microfluidic systems and demonstrated than uncured oligomers can leach into culture media and may accumulate in cell membranes. Furthermore, small molecules such as estrogen were rapidly depleted from culture media due to adsorption into PDMS, suppressing hormone-dependent signalling. While PDMS remains a valuable and widely used material for microfluidic devices, the chemical interactions between PDMS, cell culture media, and cells must be carefully considered when using or designing such systems and have been suggested as a contributing factor to the limited adoption of microfluidics by biologists [5].

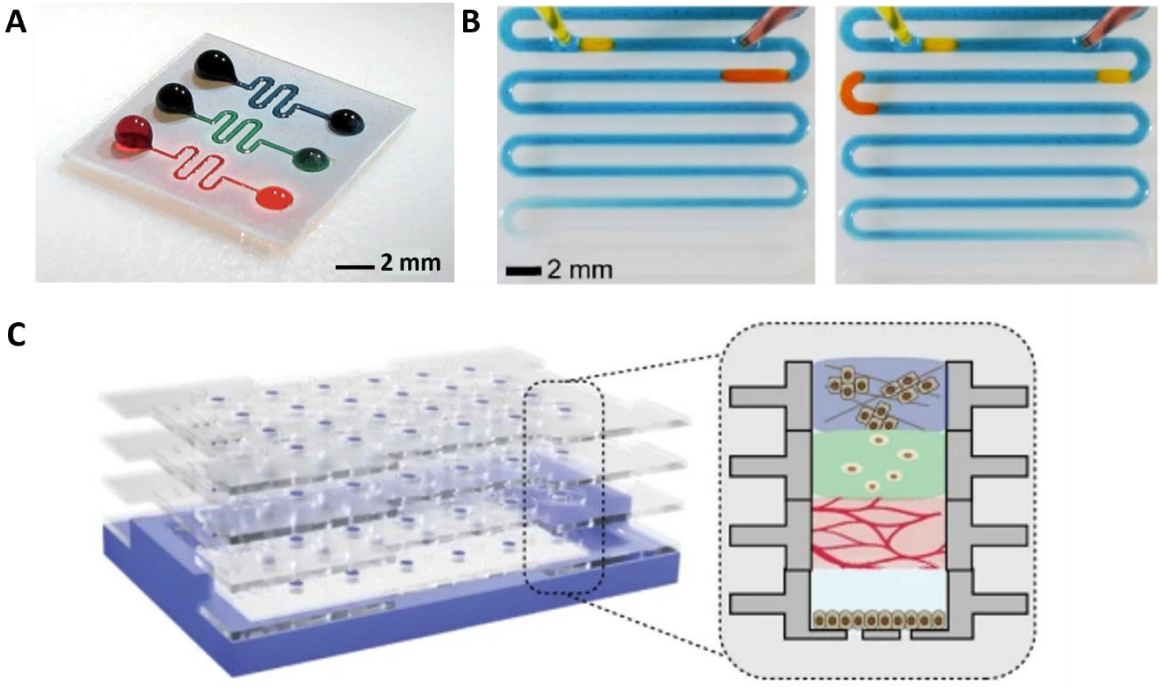

Figure 4. Examples of open microfluidic platforms. (A) A semi-open microfluidic platform where flow through a microchannel is driven by gradients in Laplace pressure [58]. **(B)** Exposed microchannels enable direct access via pipette [59]. **(C)** An example of a 3D open-microfluidic system. Suspended drops containing different cell types can be stacked to form 3D tissue models [63].

Microfluidics with fluid walls

Fluid-walled microfluidics has recently emerged as a distinct subset of OM in which aqueous media is confined by immiscible fluid interfaces, rather than solid walls [10]. In these systems, a thin layer of protein-containing medium (for example, serum or albumin – required to stabilise pinning lines [10], [68]) is overlaid with the immiscible fluorocarbon, FC40, and a micro-jet of FC40 is then used to displace the underlying medium, creating FC40 fluid walls held tightly in place by interfacial forces [69] (**Figure 5A**). Fluorinert FC40 ($C_{21}F_{48}N_2$) is gas-permeable, optically transparent, chemically stable, and bioinert as demonstrated by its compatibility with the culture of a wide range of cell types [12], [70]. Using this method, medium can be shaped into any 2D pattern within standard tissue-cultureware, creating custom microenvironments for biological studies from just standard culture medium and immiscible oil (**Figure 5B**). These fluid walls yield excellent optics [12], [47] and microenvironments are fully accessible through fluid-fluid interfaces. Furthermore, jet-printing enables rapid prototyping of microfluidic arrangements [69]. While commercially available microfluidic chips are widely used and play an important role in biological research [71], the design and fabrication of custom devices using conventional lithography-based methods can require upwards of several hours [72]. In contrast, although fabrication of fluid walls also requires technical expertise, microfluidic arrangements can be generated within seconds rather than hours.

The unique properties of fluid walls have been leveraged across an expanding range of biological applications. For example, fluid walls can be reconfigured mid-assay, enabling the isolation and retrieval of specific cell populations. This approach has been used to isolate and study migrated populations of macrophages [11] and bacteria [73] in microchannels with fluid walls. Accessibility through fluid-fluid interfaces has also been harnessed to create wound-healing assays in cell monolayers [74]. In addition, such systems have enabled directed axotomy, where iPSC-derived neurons were cultured within fluid walls and a submerged microjet used to sever axons and monitor their subsequent repair [14].

A key feature of fluid walls is the ability to generate internal pressure gradients and thereby drive flow passively. While fluid walls are pinned to 2D geometries, they are free to morph in 3D in response to volume changes and internal Laplace pressures [75], [76]. This makes flow prediction inherently complex, although significant progress has been made in recent years characterising flow within fluid walls [16], [75], [76]. The ability to generate gradients in Laplace pressure through selective addition/withdrawal of volume has been used to generate passive-pumping systems, eliminating the need for external syringe pumps (**Figure 5C**). This has been applied to enable spatial confinement of cells and chemoattractant in chemotaxis assays, and design cellular perfusion systems [13], [14], [69]. Fluid-walled microfluidics is a promising technology that enables the creation of fully accessible and reconfigurable microfluidic systems, unconstrained by solid plastic walls and formed within standard tissue-cultureware, thereby offering biologists a compelling alternative to conventional microfluidic systems.

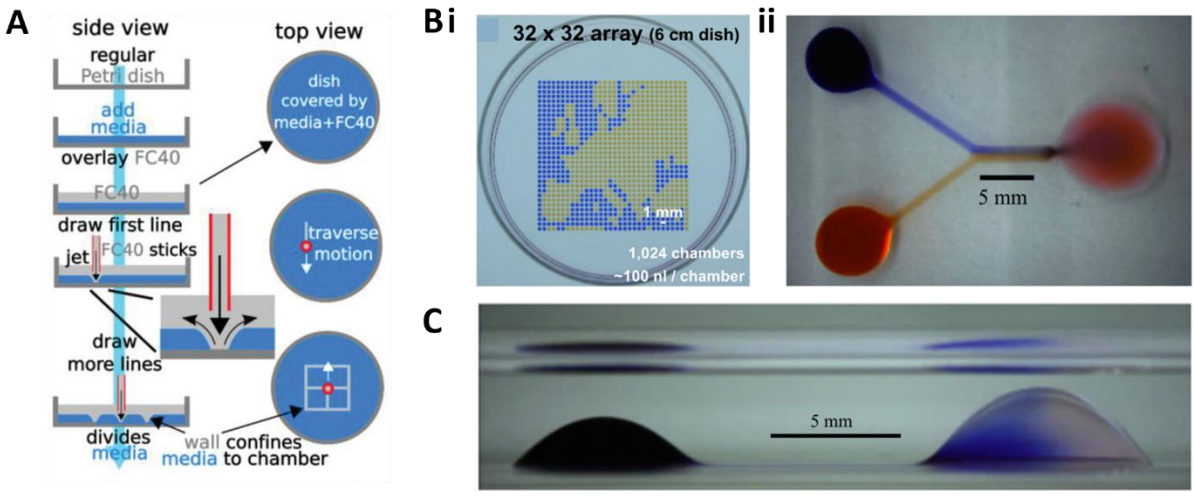

Figure 5. Microfluidics with fluid walls. (A) Fluid walls are fabricated using cell-culture medium overlaid with FC40. A submerged microjet of FC40 displaces the underlying medium, creating confined regions bounded by fluid walls [69]. **(B)** Arbitrary two-dimensional designs can be produced. Examples include **(i)** a grid of square microchambers and **(ii)** a system to generate a diffusion gradient between red and blue dyes [10]. **(C)** Fluid walls enable passively driven flow through gradients in Laplace pressure [75].

Chapter 3: Generation of clonal cultures of adherent or suspension cells using flat sessile drops for assurance of monoclonality

Authors: Joseph A.E. Morgan, Peter R. Cook, Alfonso A. Castrejón-Pita, and Edmond J. Walsh

Published: Biotechnology and Bioengineering, 122: 2739-2750 (July 19, 2025)

Abstract

Single-cell isolation is an essential step in many biomedical workflows, including genetic analyses and drug-based assays. It is commonly attempted through limiting dilution into microtiter wells. However, dark optical edge effects at the well periphery make it difficult to confirm which wells contain just one cell. Consequently, statistical methods are used to obtain the probability that a well contains a single cell. Sessile microdrops can be deposited in the centre of wells away from obscuring walls. If these drops have low contact angles, optical edge effects are minimal. A dilute cell suspension can be infused into such drops, which are then imaged to confirm the presence of a single cell with certainty. Subsequently, wells are flooded with media and incubated to allow clonal growth. The fraction of single cells yielding colonies then provides an accurate and non-probabilistic measure of cloning efficiency. We demonstrate average cloning efficiencies between 62% - 78% with human embryonic kidney, cancer, and induced pluripotent stem cells, as well as Chinese-hamster suspension cells. We verify that stem cells continue to express pluripotency markers after cloning and incorporate the method into a gene-editing workflow for cell-line development. This demonstrates the seamless integration of sessile microdrops into established protocols, providing assurance of mono-clonality with high cloning efficiency.

Introduction

Single-cell isolation and cloning are critical steps in many biomedical workflows such as drug development, cell-line engineering, and gene-editing [1]. Isolation of a single cell can provide valuable information on gene regulation and biological mechanisms not identifiable from populations of cells [2]. The processes of single-cell isolation and cloning present significant challenges. A common method involves limiting dilution into polystyrene microtiter plates: a stock solution is aliquoted into multiple wells such that each dispensed volume is likely to contain less than one cell [3]. This method relies on Poisson statistics and therefore users cannot be certain which aliquot contains just one cell. Consequently, multiple cloning rounds may be needed to provide confidence in monoclonality, adding significant time and cost [4]. In principle, monoclonality can be confirmed by imaging wells to verify the presence of a single cell post-deposition. However, this is challenging due to optical edge effects at the junction between the well base and vertical wall that result in dark regions at the well periphery, where cells cannot be observed by conventional microscopy.

This problem has driven development of many sophisticated techniques. However, the utility, delicacy, and accessibility of these methods is often limited. For example, manual ones (such as micromanipulation) are typically low throughput and require skilled operators [5], while automated ones like fluorescence activated cell sorting (FACS) use high flow rates that can reduce cell viability [5]. Furthermore, tagging with fluorescent markers to improve cell visibility can also reduce viability and/or may be inappropriate [6]. Microfluidic approaches have emerged as promising alternatives (e.g., confining cells to individual droplets [7], hydrodynamic cell trapping [8], imaging cells pre-deposition), but their complexity, poor integration into existing workflows, and known reluctance of biologists to adopt microfluidics indicates there is still significant scope for innovation [4], [9].

We present a simple and elegant approach: cells are imaged in sessile microdrops, that previous studies using an oil overlay have shown allow normal cell growth [10 - 14]. As sessile drops with high contact angles ($> \sim 20°$) yield dark edge effects that are maximal at the drop

periphery, we develop a workflow that involves imaging drops with reduced contact angles (< 15°). We create such drops directly within microtiter wells, image them, and within 2 minutes fill the well; this allows in-well verification of monoclonality so that users can be certain which drops/wells contain only one cell (without requiring an oil overlay). Using this workflow, we show that various adherent and non-adherent mammalian cells – including gene-edited stem cells – clone efficiently, and that the method can be incorporated seamlessly into current cloning protocols involving microtiter plates.

Results

The problem and a solution

The most widely-used method for cell cloning involves aliquoting a stock solution (where the dispensed volume typically contains < 1 cell) into wells in a microtiter plate [3]. **Figure 1A** is an image of a well filled with medium (200 µL) using this approach. When viewed from below, refraction of light at the plastic junction between the well base and wall yields a peripheral dark zone that obscures any cells, if present. Consequently, users can never be certain a well contains only one cell. Our approach involves depositing a microdrop (typically ~1 µL) in the centre of a well (away from the dark peripheral zone), and we will see that refraction of light across the curved surface of such a drop yields a different kind of edge effect – this time at the drop periphery (**Figure 1B, C**). This second effect can also obscure cells; however, this edge effect can be minimized by reducing the angle of incidence at the drop periphery, which can be easily achieved by exploiting the phenomenon known as contact-line pinning. Many cell-culture media display strong pinning: volume can be removed from a drop without a reduction in footprint diameter [4]. This reduction in angle of incidence allows a clearer view throughout the drop (**Figure 1C**). We describe drops before and after removing volume as ‘full’ and ‘flat.’ A full drop yields strong edge effects of both types (**Figure 1D**, left), but the flat drop (90% volume removed) now has essentially no obscuring region at the drop periphery (**Figure 1D**, right).

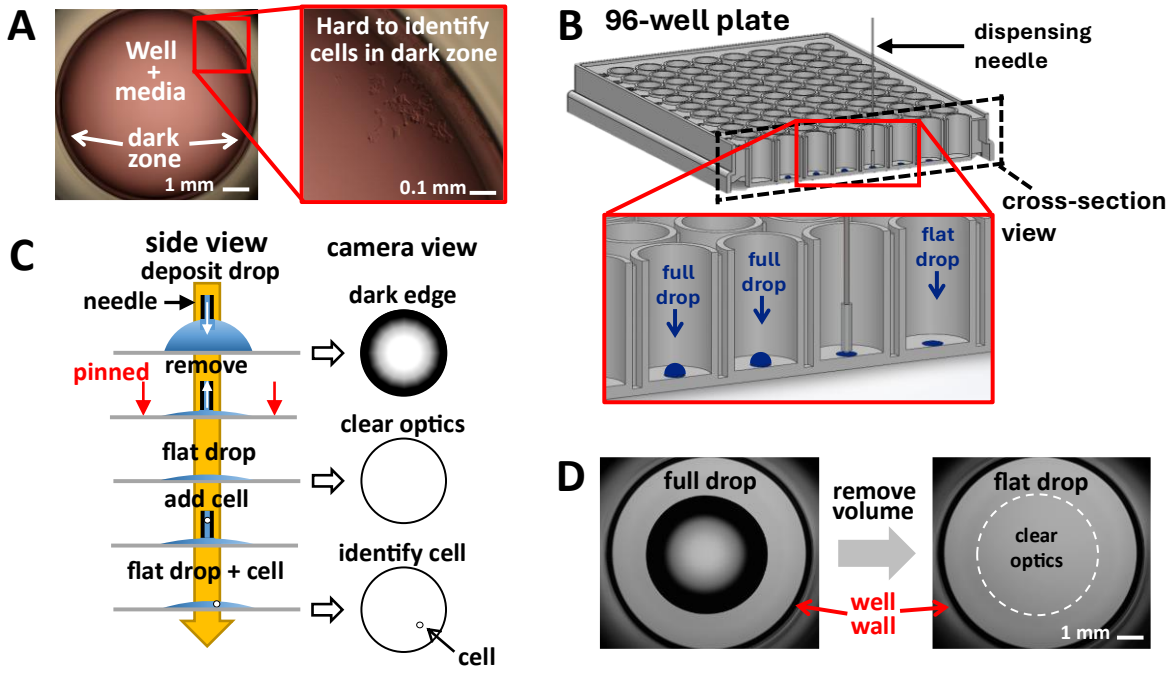

Figure 1. Identifying single cells in microtiter wells. (A) A microtiter well containing media viewed from beneath. Refraction of light at the junction between the well base and well results a dark zone at the periphery where it can be difficult to identify cells. **(B)** A solution is to deposit a drop centrally within the well, away from the dark zone. Withdrawing volume from the drop leaves a flat drop. **(C)** Refraction of light across the curved surface of the original full drop results in dark edges at the drop periphery, where it can be difficult to see drop contents. We exploit contact line pinning, whereby volume can be removed without a reduction in footprint diameter. This reduces the angle of incidence and eliminates dark regions within the sessile drop, giving a clear view of drop contents. Adding a small volume (we tested 50 nL and 0.5 µL) of fluid containing a single cell to the drop allows users to confirm the presence of a single cell microscopically. **(D)** Removing volume provides clear optics within the drop, where users can clearly identify cells. Depositing the drop centrally ensures the dark well periphery no longer compromises the image.

Theory: contact-line pinning and optics in sessile drops

A drop deposited on a surface spreads to its equilibrium contact angle (θ_E) which depends on multiple factors including interfacial tension, surface roughness, and temperature [15]. Adding volume to a drop increases the contact angle, until the advancing contact angle (θ_A) is reached and the drop footprint spreads. Conversely, removing volume reduces the contact angle, until the receding contact angle (θ_R) is reached and the footprint retracts. The difference $\theta_A - \theta_R$ is described as contact-angle hysteresis and can be used to quantify contact-line pinning – the degree to which the contact line is fixed (**Figure 2A**). Certain fluids

are tightly pinned, such that >95% volume can be removed without an observable reduction in footprint area ($\theta_R \ll \theta_E$).

Maintaining low contact angles improves internal drop optics, since it minimizes the effects of the refraction of light across the curved interface. If a drop is sufficiently small (i.e., drop radius is below the capillary length, λ_c; which in water is ≈ 2.7 mm):

$$\lambda_c = \sqrt{\frac{\gamma}{\Delta\rho g}} \tag{1}$$

(where γ is surface tension, g gravitational acceleration, and $\Delta\rho$ the density difference between liquid and air), interfacial forces will outweigh gravitational ones, and the drop adopts a geometry that can be modelled using that of a spherical cap (**Figure 2Bi**). Drop volume, V, is therefore:

$$V = \frac{a^3}{\sin^3\theta} \cdot \frac{\pi(2 - 3\cos\theta + \cos^3\theta)}{3} \tag{2}$$

where θ is the contact angle and a the footprint radius. Maximum drop height, h, can be obtained easily:

$$h = \frac{a}{\sin\theta}(1 - \cos\theta) \tag{3}$$

Knowing h and a, drop radius of curvature R is:

$$R = \frac{a^2 + h^2}{2h} \tag{4}$$

Drop curvature can then be used to predict how light is refracted across the curved liquid-air interface. The critical angle φ_{max} beyond which light is refracted outside of the microscope objective is dependent on both numerical aperture NA and refractive index of the medium the light passes through, n:

$$\varphi_{max} = \sin^{-1}\left(\frac{NA}{n}\right) \tag{5}$$

If light is refracted beyond φ_{max} it will not be collected by the objective and appears as a dark region in the resulting image (**Figure 2Bii, iii**). The radius of the visible area within a drop (R_m)

can be calculated using the radius of curvature and tangent between the drop surface and horizonal α using:

$$R_m = R\sin(\alpha_m) \tag{6}$$

The summation of refractions through each medium gives the total refraction, this includes through the drop ($n_{water} \approx 1.33$), the polystyrene dish ($n_{dish} \approx 1.5$), and air between dish and objective ($n_{air} = 1$), determined using Snell's law:

$$n_1 \sin\theta_i = n_2 \sin\theta_r \tag{7}$$

where θ_i and θ_r are angles of incidence and refraction, and $n_{1,2}$ the refractive indices of the different materials [4] (**Figure S1** [p. 48] shows experimental validation of theory).

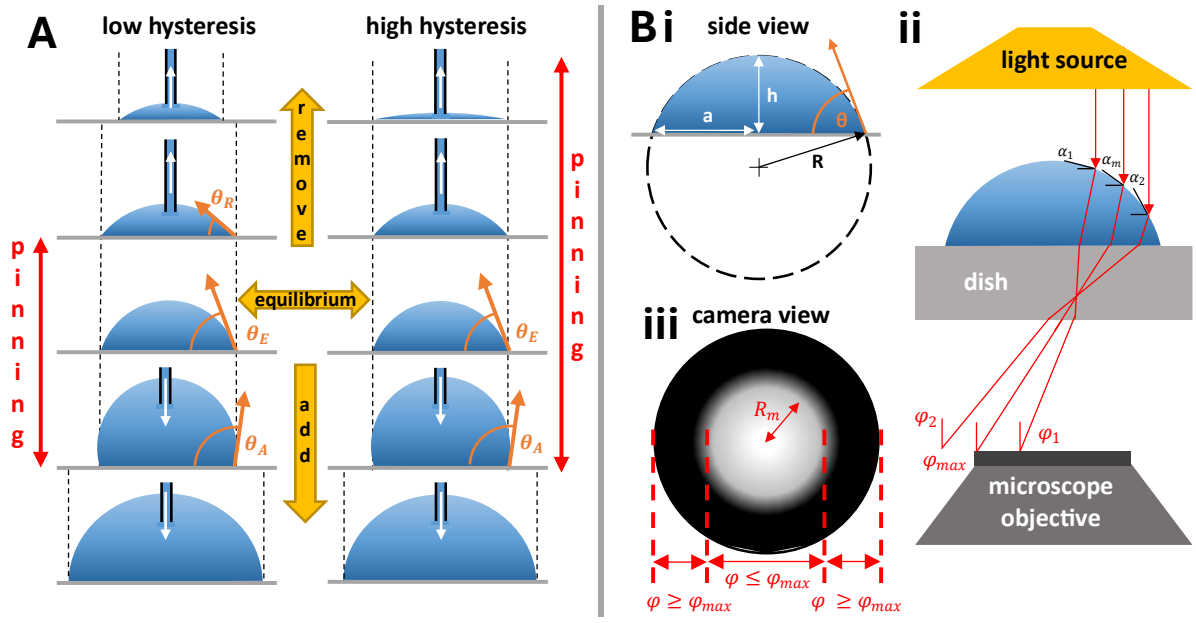

Figure 2. Contact-line pinning and sessile-drop optics. (A) Drops with low and high contact-angle hysteresis. Middle row: drops deposited on a surface spread until the equilibrium contact angle, θ_E, is reached. Two bottom rows: adding volume does not increase the footprint until the advancing contact angle, θ_A, is reached. Two top rows: removing volume does not decrease the footprint until the receding contact angle, θ_R, is reached. Drops are pinned between θ_R and θ_A. Almost all fluid can be removed from a drop with high hysteresis without reducing the footprint diameter. **(B)** Optical properties of sessile drops. **(i)** Geometry of spherical cap. **(ii)** Light from the microscope light source is refracted across the curved air-drop interface, and light rays (red lines) beyond φ_{max} are not collected by the objective. **(iii)** In the camera view, lost light yields a dark zone (in which any cell present cannot be seen). Figure adapted from Soitu *et al.*[4]

The workflow

Figure 3 outlines our workflow. A microdrop (typically 1 µL) is deposited in the middle of a conventional 96-well microplate using a programmable 3-axis traverse (detail regarding automated traverse and syringe pump provided in methods, images shown in **Figure S2** [p.48]). Next, ~90% of the volume is removed to reduce the contact angle and produce a flat drop, a small aliquot of cell suspension added (typically 50 nL containing ~1.4 cells so that wells receive 0, 1 or 2 cells, calculated using Poisson statistics), the drop is imaged from below to confirm which wells contain just one cell, the well manually flooded with growth medium (typically 200 µL), and the microplate incubated to allow clonal growth. Finally, cloning efficiencies are determined. Conventional limiting dilution is used as a control; however, results from this control are subject to substantial uncertainties associated with counting and diluting cell numbers accurately. Our workflow depends on two critical steps: ensuring pinning lines do not retract when fluid is withdrawn to create flat drops, and that these drops are sufficiently flat to lack obscuring dark zones at their periphery. If there is no hysteresis, the pinning line will retract as fluid is removed to maintain a constant equilibrium contact angle and hence retain dark zones.

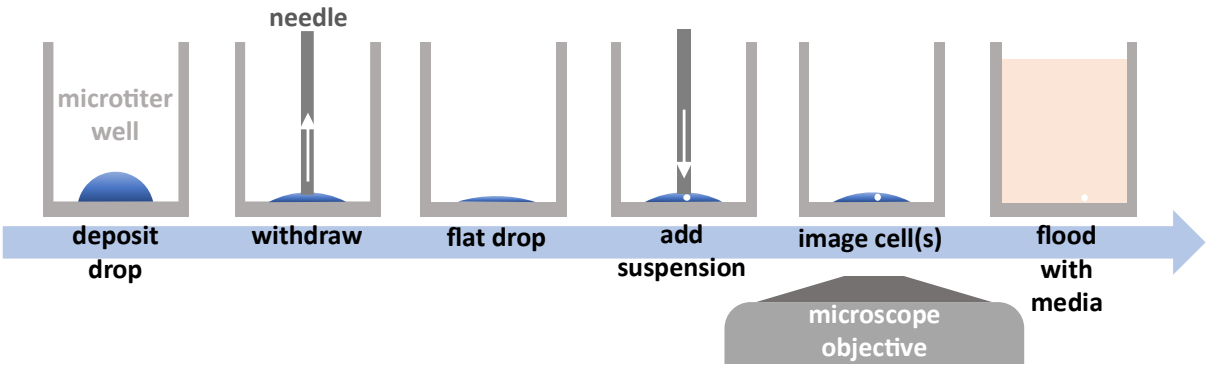

Figure 3. Using sessile microdrops in a cloning workflow. A drop is deposited into a microtiter well (typically 1 µL), volume withdrawn (90%) to leave a flat drop, and a small volume of cell suspension added (typically 50 nL). The now-flat drop is imaged to confirm the presence of a single cell and flooded with media to allow normal cell growth.

Pinning line stability

Fetal bovine serum (FBS) is present in most media used to culture mammalian cells; it also stabilizes pinning lines [4]. Unfortunately, it is a complex, undefined, and variable bioproduct that contains many different proteins – and this is driving development of chemically-defined alternatives [16]. As we wished to develop an alternative that provides excellent pinning on the different polystyrene surfaces found in the microplates used to culture adherent and non-adherent cells, we screened various fluids (**Figure S3** [p. 49]). Phosphate-buffered saline (PBS) is perhaps the simplest and most widely-used salt solution in cell culture, and when supplemented with 0.5 mg/mL bovine serum albumin (BSA) – but not a non-protein alternative like poly-ethylene glycol, PEG – it pinned micro-drops on both types of surface (**Figure S3** [p. 49]). Therefore, generally we use it when creating flat drops.

Optical properties of flat drops

Figure 4A shows a 1 µL drop of PBS + 0.5 mg/mL BSA deposited on a polystyrene surface treated for tissue culture (see Materials and Methods for detail). The drop has a high contact angle (θ_E ≈ 60°, calculated using drop footprint and spherical cap geometry), and a dark zone at the drop periphery is clearly seen in the microscope when viewed from below. Removing 0.9 µL does not reduce footprint diameter; the drop is pinned (θ ≈ 7.3°) and now optics across the entire drop footprint have become much clearer. After adding 0.05 µL containing ~1.4 cells users can now count precisely the number of cells delivered (here, one) despite the (slight) increase in contact angle (θ ≈ 11°) because the total refraction is still below the critical angle (14.5° for the 10X objective).

Drops with different numbers of cells can be imaged clearly (**Figure 4B**) using a standard microscope. **Figure 4C** shows that a variety of cell types are clearly identifiable using 4X and 10X objectives. Here we show a single (adherent) iPSC in a flat drop (5µL PBS + 8 µg/mL laminin initially deposited, 90% volume removed), a single non-adherent CHO-S cell in a flat drop (1 µL PBS + 0.5 mg/mL BSA initially deposited, 90% removed), and a whole-well view of a single adherent LNCaP cell in a flat drop (same as for CHO-S). In all cases, images of single

cells are no longer compromised by edge effects where the well base meets the wall, or by curvature at the drop periphery.

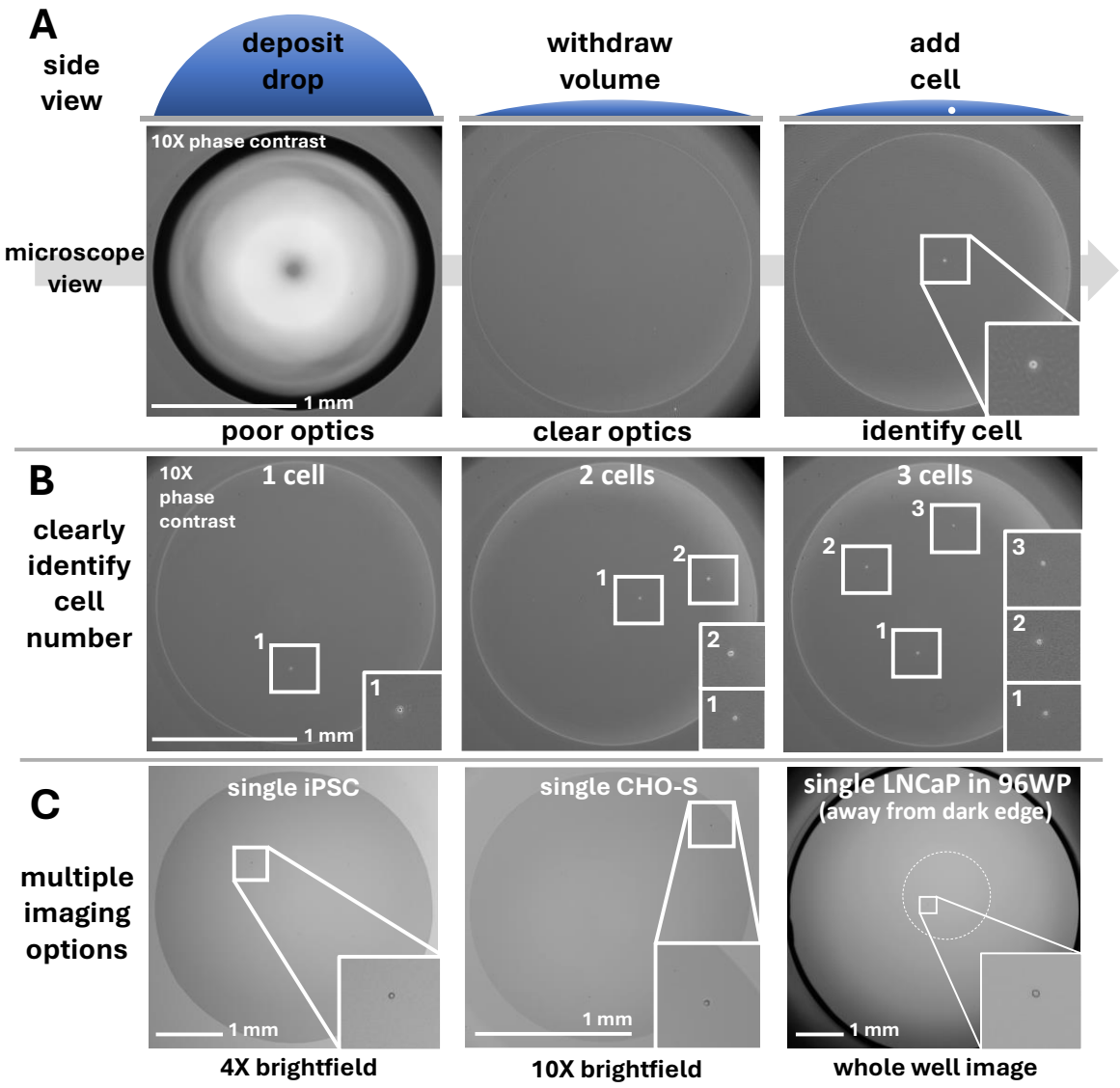

Figure 4. Identify cells in microdrops. (A) Method for identifying a single cell. A drop initially has poor optics, withdrawing volume improves optics and – after adding a single cell – the cell can be seen clearly. **(B)** Users can count numbers of cells (here, from human embryonic kidney) per well accurately. **(C)** Cells can be seen clearly using 4X and 10X objectives, in brightfield or phase contrast. The dotted circular white line marks the drop periphery in the whole well images (where edge effects at the well periphery are clearly visible).

Cloning efficiencies

Figure 5A shows example clonal colonies of LNCaPs after 21 days of incubation, and CHO-S after 14, both of which proliferated from a single cell. As expected using this method, adherent colonies usually grow in the middle of the well (**Figure 5Bi**) in which case the entire colony can be seen clearly, away from the dark well edges. However, some grow in the dark zone at the well periphery (**Figure 5Bii**); this highlights the need for confidence that a well initially contained only one cell.

A range of matrix coatings were tested to assess which cell-culture fluids are tightly pinned to polystyrene surfaces (**Figure S3** [p. 49]). For example, laminin is commonly used in the culture of iPSCs. After 7 days, colonies growing from a single iPSC can be clearly identified growing on the matrix (**Figure 5C**). Such colonies grow to fill the original footprint of the drop, without extending into the non-coated region of the well that is now covered with medium only. In other words, iPSCs do not grow beyond the edge of the laminin coating, giving a clear image of the whole colony in the center of the well. Here, larger 5 µL drops were used, providing a larger footprint area permitting larger colony growth prior to passaging.

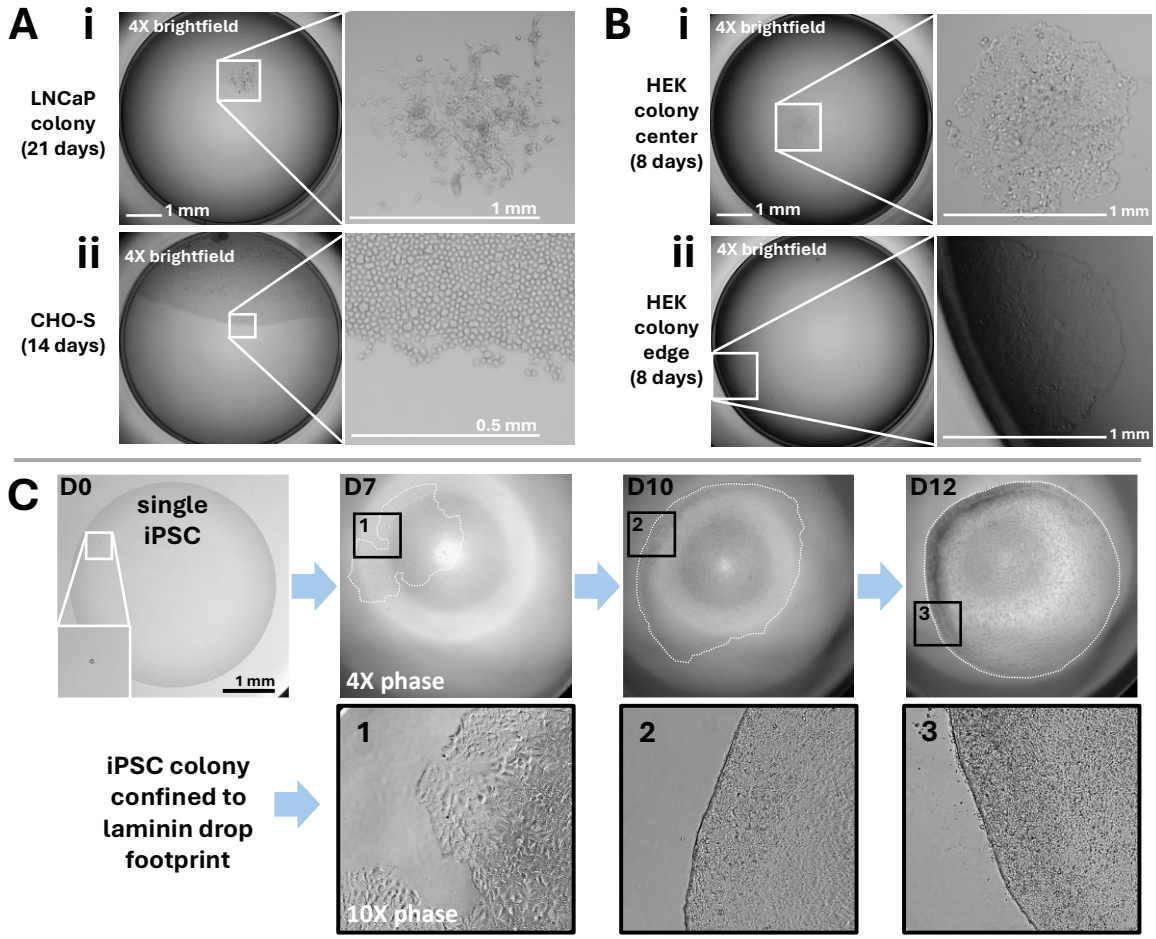

Figure 5. Single cells grow to colonies. (A) Whole-well images of colonies of **(i)** LNCaP cancer cells (d 21), and **(ii)** CHO-S (d 14). **(B)** Whole-well images of colonies growing in **(i)** the center of a well or **(ii)** at the well periphery, where they are partly obscured from view. **(C)** Part-well images of an iPSC (d 0) growing to a colony (d 7, d 10, d 12; dashed white lines outline colony, magnifications of boxed regions 1-3 shown below, image contrast enhanced and sharpened). Colony is confined to the footprint of initial laminin coating drop, providing a clear whole-colony image

Figure 6A shows some cloning efficiencies achieved using various cells, growth media, and coatings: all are in the expected range (based on reported efficiencies between ~50% - 70% for optimised human PSC and iPSC cloning workflows [17],[18]) and validate the gentle handling of single cells throughout the workflow. Each triplicate represents average cloning efficiencies across 3 x 96-well plates (3 biological reps). iPSC cloning efficiencies on various matrix coatings represent a single biological rep averaged over 3 x 96-well plates (apart from laminin). We also noticed that (adherent) HEK colonies often grew closer to the center of the well compared to those formed using the conventional method (~87% in the center, vs ~31% respectively, **Figure 6B**). This is likely attributed to the initial central deposition in the well – a

cell falls to the bottom and then is not displaced when the well is flooded with medium. Conversely, during conventional cloning, cells are prone to settle at the well periphery. As cell stress and changes in microenvironment can impact differentiation of iPSCs [19], we performed quality-control tests which showed that various pluripotency markers (i.e., SSEA-4, OCT-4, SOX-2 and TRA1-60) continued to be expressed normally after cloning (**Figure 6C**, see **Figure S5** [p. 51] for conservation using coatings other than laminin, plus staining for SSEA-1, which we use as a negative control – not expressed if cells are in a pluripotent state [20]).

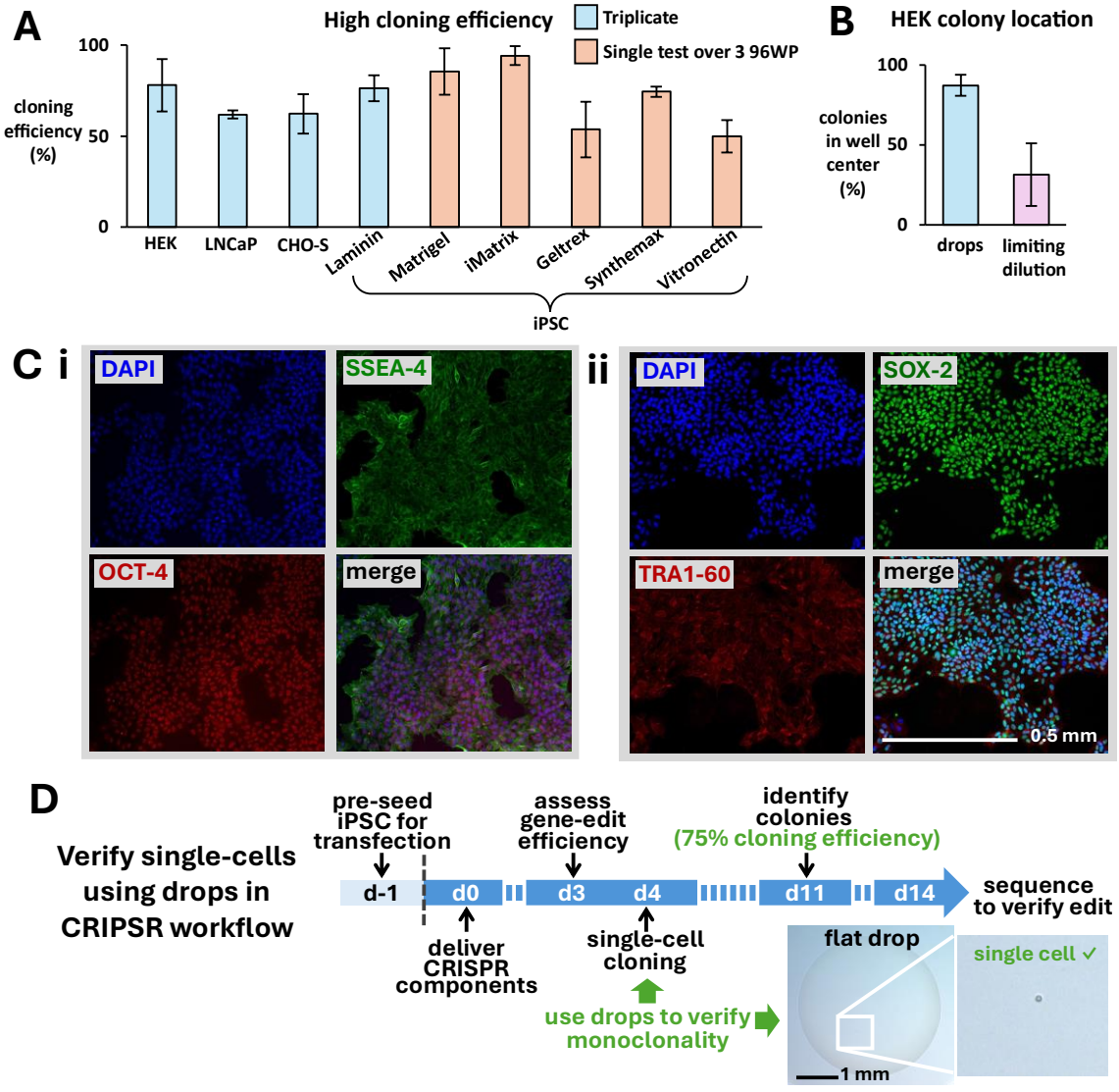

Figure 6. Cloning efficiencies, colony characteristics, and a CRISPR workflow.

(A) Excellent cloning efficiencies are obtained after imaging in drops (error bars ± standard deviation). **(B)** HEK colonies are more likely to grow in the centre of the well after imaging in microdrops. **(C)** iPSC pluripotency is retained post-imaging, demonstrated by **(i)** markers for SSEA-4/OCT-4 and **(ii)** SOX-2/TRA1-60. **(D)** Timeline demonstrating how single-cell verification using flat sessile drops is incorporated into a CRISPR gene-edit workflow.

Incorporation into a gene-editing workflow

Finally, we integrated our method into a CRISPR gene-editing workflow (**Figure 6D**; **Figure S6** [p. 52] provides detail). Clonal selection is an essential step in such workflows as not all cells are edited. The MYBPC3 gene (which encodes cardiac myosin building protein) is important in cardiac pathophysiology [21], and we knocked it out (through frameshift mutations [22]) in human iPSCs using a standard protocol [23]. Three days after editing, samples were sequenced and showed 75% knockout efficiency – a measure of how many of the contributing indels are likely to result in a functional knockout [24]. On day four (d4), a dilute solution of edited cells was dispensed into flat drops of PBS plus 8 µg/mL laminin in microtiter wells; 61 drops contained single cells, and – after flooding with medium, 46 of these single cells grew to give colonies by d14 (75% cloning efficiency). Twelve of these colonies were now randomly selected, the targeted segment amplified, and sequences determined. Eleven of the twelve clones had been edited. This provides a proof-of-concept that our method can be incorporated seamlessly into standard editing protocols for cell-line development.

Discussion

Poor optics at the edge of microtiter wells make single-cell verification challenging. Depositing cells within a sessile drop in the center of a well and so away from the edge mitigates against this. However, it introduces another problem: drops with high contact angles exhibit poor optics at their periphery due to refraction across the air-liquid interface. We leverage contact-line pinning to reduce the contact angle; this improves optics and enables visual confirmation of monoclonality within microtiter wells (**Figure 1**).

We screened various fluids to see which are pinned to polystyrene surfaces (**Figure 2**) and found that some protein-rich solutions – including FBS – are successfully pinned (**Figure S3A, B, C,** [p. 49]). This aligns with previous studies [4], [25] and is likely due to protein adsorption at the pinning line [26]. However, FBS is an ill-defined and variable bioproduct [16], and it's critical constituent – albumin (from bovine or human serum [27], **Figure S4** [p. 50]) – pinned just as well at concentrations one-tenth that found in human serum (~50 mg/mL) [28]. Using a 3-axis traverse to automate the workflow (**Figure 3**), microdrops were deposited, 90% drop volume withdrawn, a small volume of cell suspension added (typically 50 nL, 0.5 µL when imaging iPSCs) to yield drops free of edge effects and drops imaged (using 4X and 10X plus brightfield or phase contrast). Wells containing single cells were identified (**Figure 4**) and filled with medium within ~2 minutes (peripheral sacrificial wells were filled with PBS to minimize the effects of evaporation on cell survival in the inner ones). Automated seeding of cells into drops took ~1 second per well. Our total workflow took ~20 minutes to process all 60 inner wells (~5 minutes per 15 wells) of a 96-well plate. Single cells were in drops for no more than ~2 minutes (imaging time) before flooding with media. We calculated that an integrated liquid handling and imaging system would take ~5 minutes to process an entire 96-well plate from seeding of single-cells to flooding wells with media. For iPSCs, larger drops (5 µL; ~3.8 mm diameter) were deposited to create a larger footprint and permit greater cell proliferation on the matrix-covered area. Here, withdrawing 90% volume and adding 0.5 µL cell suspension gives an imaging contact angle of ~ 10.6^{o} (laminin drop).

Colonies are clearly identified using a conventional microscope on d7 for rapidly-growing iPSCs, d8 for HEKs, d14 for CHO-S, and d21 for slow-growing LNCaP (**Figure 5**). Average cloning efficiencies across all cell types were between 62% - 78%, including those for iPSCs grown on a wide range of matrices without loss of pluripotency markers (**Figure 6A, C; Figure S5** [p. 51]). Additionally, our approach is easily incorporated into an established gene-editing protocol (**Figure 6D**).

Our workflow has various advantages, with the most important being the certainty that a colony is derived from a single cell. Furthermore, coating just the area of microdrop footprint compared to the whole well provides savings in expensive coating reagents (e.g., coating a drop footprint area of 8 mm^2 gives a 75% reduction in coating consumption compared to traditional methods in 96-well plates; **Figure S3D** [p. 49]). Adding cells to microdrops centrally in wells also provides some control over where a cell first adheres to the surface, and hence ultimate colony location (e.g., adherent HEKs are usually not dislodged during well flooding, and this allows a clear whole-colony view in the center of the well, **Figure 5B**). This could facilitate earlier colony identification, earlier passaging, and could enable reduced experiment time compared to the conventional approach where peripheral colonies must grow to sufficient size to be seen in the visible well center.

Our method has limitations. First, infusion of cells into drop footprints is governed by Poisson statistics – users cannot guarantee they will get a single cell per drop. Some wells will receive no cells (others more than one), and visual confirmation is required to determine which contain just one cell. However, the number of wells receiving one cell could be improved by re-infusing empty drops with an additional aliquot. Second, of the fluids tested, only those containing proteins (serum or albumin) remained pinned on both treated and untreated polystyrene, thereby limiting the range of fluids suitable for forming flat drops. Third, counting errors commonly lead to infusion of too many (or too few) cells in a drop; however, as users can count exact cell numbers in each drop, they can work backwards to determine the true concentration dispensed. For example, we use a simple maximum likelihood estimation to fit Poisson distributions to iPSC cell counts per well (18 x 96-well plates in total) and find that on

average, 1.87 cells were deposited per well (standard deviation of ±0.44); this indicates that the true cell concentration was higher than counted manually (target of 1.4 cells per well, **Figure S7** [p. 53]**).** Note that limiting dilution experiments are subject to the same uncertainty, with some experiments yielding (apparent) cloning efficiencies of >100%, or misleadingly poor ones. Fourth, drop footprint diameter is limited by well diameter (6 mm; then, for example, using a 0.5 mm tolerance, the maximum possible footprint diameter is 5 mm – that of a ~20 µL drop on treated polystyrene. Finally, drops must be positioned away from the well walls to avoid well edge effects.

In summary, flat sessile drops provide excellent optics for imaging single cells in standard microwells, and cells clone efficiently after imaging. This provides certainty in monoclonality, and the method can be incorporated seamlessly into existing workflows.

Materials and methods

Cells

Cells were grown routinely at 37ºC and 5% CO_2, counted manually using a haemocytometer unless stated otherwise, and diluted to the required concentration.

Human embryonic kidney (HEK) 293 cells [29] were cultured in 5 mL DMEM (Sigma-Aldrich) + 10% FBS (Gibco) + 1% Penicillin-Streptomycin (Gibco) in 25 cm^2 polystyrene canted neck flasks (Corning). They were prepared for experiments by removing medium, rinsing with 1 mL PBS (Sigma-Aldrich), detached from the polystyrene surface (1 mL trypsin; TrypLE Express, Gibco), incubated (37ºC, 2 mins), trypsin was neutralised by adding 4 mL media, cells transferred to a 15 mL centrifuge tube (Falcon), (centrifuged 47 x g relative centrifugal force, RCF; 3 mins), the supernatant removed, cells resuspended in PBS and counted.

Lymph node carcinoma of the prostate (LNCaP) cells [30] were cultured in 20 mL RPMI-1640 medium (Sigma-Aldrich) + 10% FBS + 1% MEM non-essential amino acids (Gibco) + 1% Penicillin-Streptomycin + 1% L-Glutamine (Gibco) + 1% sodium pyruvate (Gibco) + 1% MEM vitamin solution (Gibco) in 75 cm^2 U-shaped canted neck cell culture flasks with vent

cap (Corning). Cells were prepared for experiments as above with the following variations: rinse with 2.5 mL PBS, detach with 3 mL trypsin, 4 mins incubation, neutralise with 4 mL complete medium, and spin for 5 mins (31 x g RCF).

Chinese hamster ovary suspension (CHO-S) cells [31] were cultured in CD CHO medium (Gibco) + 40 mL/L L-Glutamine in 25 cm^2 polystyrene canted neck flasks stood vertically to inhibit cell attachment. When cloning, non-treated (suspension) microtiter wells were flooded with a 1:1 ratio of CD CHO + 40 mL/L L-glutamine and DMEM/F12 (1:1) (Gibco) since this combination is known to support clonal growth of CHO-S [32].

KOLF2-C1 iPSCs [33] were cultured in StemFlex + supplement (Gibco) + 1X CloneR2 (Stemcell Technologies) in 6-well clear tissue-culture-treated plates (CytoOne, Starlab) coated with Biolaminin 521 (BioLamina) as per manufacturer's instructions. Cells were prepared for experiments by rinsing with 1 mL PBS, detach with 1 mL trypsin, 5 mins incubation, neutralise with 2 mL StemFlex + supplement + CloneR2 per well. Cells were spun (300g; 5 mins), supernatant discarded, resuspended in 1 mL complete media, and stained using Trypan Blue (Gibco) for counting. iPSCs were obtained and used in accordance with applicable ethical guidelines. Documentation supporting ethical compliance is available from the authors upon reasonable request.

Cell suspensions were aspirated manually via pipette before collection by the dispensing system, mitigating sedimentation within the reservoir.

Drop optics theory validation

To validate the critical-angle theory for drops, we dispensed a 1 µL drop of PBS + 0.5 mg/mL BSA onto a 60 mm treated polystyrene dish (Corning) using a syringe pump (Harvard Apparatus) and 50 µL syringe (Hamilton). Sacrificial drops (~10 µL) were manually deposited around the central drop to mitigate evaporation. The drop was subsequently imaged from below, and footprint measured using ImageJ [34].

Volume was incrementally removed from the drop in 100 nL steps (10% of the initial volume) using the syringe pump, imaging after each withdrawal. The radius of the visible area

was determined by vertical lines through the drop center and plotting corresponding grey values; the boundary for determination of critical angle was defined when there was a 15% decrease in pixel intensity observed compared to the center of the drop. Measurements were averaged along the vertical line and compared with the analytical results presented in **Figure S1** [p. 48]**.**

Screening fluids used to create drops for cell imaging

To assess the ability of a fluid to retain a low contact angle, 5 μl drops were deposited manually onto a 60 mm polystyrene tissue-culture-treated dish (Corning) and the footprint imaged. Approximately 4.75 μl (95% drop volume) was then manually removed from the drop via pipette and footprints re-imaged. If there was no visible change in drop footprint diameter, the fluid can be considered sufficiently pinned to facilitate imaging. For each fluid this process was repeated on non-treated 60 mm polystyrene dishes (Corning). Fluids tested include deionized water, PBS, DMEM, a range of polyethylene glycol solutions (PEG, Sigma-Aldrich), and solutions containing 0.05%, 0.5%, and 5% BSA. All solutions were prepared in PBS unless stated otherwise.

Matrix coatings for iPSCs (5 μL) were deposited into each well of a 96-well tissue-culture-treated microtiter plate (Corning). Drops were incubated for the manufacturer's recommended duration (typically 1-2 h), imaged using an inverted microscope (Olympus IX53), 4.5 μL removed, and drop footprints re-imaged. Drops were then measured using FIJI (imageJ [34]) and footprint diameter compared before and after removing volume to determine whether the fluid is pinned. Various matrix coatings were tested including human recombinant laminin 521 (LN521, BioLamina), Matrigel hESC-Qualified Matrix (Corning), iMatrix-511 (TakaraBio), Geltrex LDEV-Free, hESC-Qualified reduced growth factor basement membrane matrix (Gibco), Vitronectin recombinant human protein (Gibco), and Synthemax II-SC substrate (Corning). Concentrations used in creating drop footprints can be found in **Figure S3D** [p. 49].

Automated drop deposition

The deposition, addition, and withdrawal of fluid from drops was automated using a programmable motorized 3-axis traverse and incorporated syringe pump (iotaSciences). The syringe pump was driven by a stepper motor (NEMA11, model 11HS12-0674S) with 1 mm lead screw. This was used to give precise spatial control of a 25-gauge dispensing needle connected to a 500 µL glass syringe (Hamilton) via 28-gauge PTFE tubing (Adtech). All fluids used in drop deposition were aliquoted into 1.5 mL microtubes (Eppendorf) for handling by the printer. Printer commands were written in GCMC and compiled to G-code. The tubing, needle, and syringe were kept filled with 70% ethanol solution when not in use. Drops for imaging iPSCs (matrix coatings) were deposited using a similar 3-axis traverse with incorporated syringe pump (isoPick, iotaSciences) in which fluid was handled via a 23-gauge dispensing needle (standard needle for isoPick fluid printer, Tomlinson Tube) connected to a 500 µL glass syringe (Hamilton) via 24-gauge PTFE tubing (Adtech).

Drops for imaging HEK, LNCaP and CHO-S

Drops (1 µL PBS + 0.5 mg/mL BSA) were deposited into the central 60 wells of a 96-well microtiter plate (peripheral wells were pre-filled with 200 µL PBS to reduce evaporation in central wells). For HEK and LNCaP, drops were deposited in a flat bottom tissue-culture-treated 96-well plate, and for CHO-S in a flat bottom non-treated 96-well plate (both Corning, treated plate product code 3596, non-treated 3370). Fluid to create drops was collected by the printer and separated from ethanol within the tubing by a PBS slug (10 µL) flanked by two air gaps (3 µL). Drops were deposited with the tip of the dispensing needle 0.5 mm above the well base. This process was done 15 wells at a time to reduce the time a drop was left exposed to air. Next, 0.9 µL was withdrawn from each drop, by inserting the dispensing needle into the drop at a height of 0.1 mm from the well base. Next, 0.05 µL cell suspension (~28,000 cells/mL) was infused into the now-flat drop from a height of 0.1 mm from the well base. The plate was then transferred from the printer to the microscope for imaging. Finally, wells were

flooded manually with 200 µL media before starting the process again for the next block of 15 wells.

Drops for imaging iPSCs

Matrix coatings (5 µL) was deposited (from a height of 1 mm from the well base) into the central 60 wells of a 96-well microtiter plate. Drops were then incubated (37°C, 5% CO_2) for the time recommended by the manufacturer (1 h for Matrigel, Geltrex, Synthemax, and vitronectin. 2 h for laminin; no incubation required for iMatrix). After incubation, 4.5 µL was withdrawn from drops to reduce the contact angle. This was done 15 drops at a time to reduce the time drops were exposed to air. Next, 0.5 µL cell suspension was added to drop footprints (2,800 cells/mL, at a height of 0.15 mm from the well base). The plate was then transferred from the printer to the microscope for imaging. Finally, wells were flooded manually with 100 µL media (reduced volume to save comparatively expensive culture media for iPSCs). Wells containing a single cell were manually topped up with an additional 100 µL media after 5 d to maintain healthy colony growth.

Limiting-dilution control experiments

In each case, control experiments were performed using limiting dilution into 96-well microtiter plates. Stock concentrations were diluted to 2.5 cell/mL in 14 mL media in a 15 mL centrifuge tube (Greiner). From this suspension, 200 µL was manually deposited into each of the inner 60 wells of a 96-well microtiter plate. In the case of iPSCs, the same concentration was achieved in 7 mL media, and 100 µL was manually deposited into each inner well to reduce consumption of expensive media.

Cloning efficiency in microtiter plates

Cloning efficiency is typically calculated using:

$$\text{Cloning efficiency}(\%) = \left(\frac{\text{colonies from single cell}}{\text{single cells}}\right) \times 100$$

However, for the reasons previously discussed, the true number of single cells actually present in a microtiter plate is often unknown. This means that users rely on Poisson statistics to give the probability $P(x)$ that a well contains a single cell:

$$P(x) = \frac{e^{-\lambda}\lambda^{x}}{x!}$$

where x is the number of cells (1 for a single cell), and λ the average number of cells per well (typically $\ll 1$). Using this method, users can estimate the number of wells expected to contain a single cell for a given stock concentration. This measure of cloning efficiency is a probability-based estimate and depends on an accurate estimate of cell concentration. Errors in cell counting, which are common with manual counting, can lead to cloning efficiencies even greater than 100%. Similarly, low cloning efficiencies might misleadingly indicate poor cell viability when they could be a consequence of counting error.

Markers for iPSC pluripotency

Single cells were deposited into flat drops of laminin, Matrigel, and iMatrix coatings within microtiter wells (96-well plate) on d0. On d3, media was changed (StemFlex + CloneR2) and on d5, colonies from single cells identified and media changed to StemFlex only. On d7, colonies were transferred from respective coatings and split across three wells of a LN521-coated 6-well plate. On d14, cells were frozen in Knock-out serum replacement (Gibco) + 5% DMSO (Sigma) at 1 x 10^6 cells/mL in 1.5 mL vials (Nalgene, ThermoFisher). Vials were then sent to Cellected (Cellected Ltd, Salisbury, UK) for testing and analysis of pluripotency; 5 vials contained cells grown on laminin, 5 grown in iMatrix, 4 grown on Matrigel, and one parental (not cloned) grown on laminin which we use as a control.

After recovery of frozen cells in StemFlex media on laminin matrix, cells underwent morphological assessment and immunocytochemistry/immunofluorescence (ICC/IF) tests for Oct4, SSEA4, Sox2, Tra-1-60 (positive control) and SSEA1 (negative control) following ISCCR

guidelines [35]; all gave results as expected. The commercial service also included analysis using a single nucleotide polymorphism (SNP) array (Infinium GSA v3), plus tests for mycoplasma and sterility; results were as expected and not shown.

CRISPR gene-edit workflow

Flat drops were incorporated into a CRISPR gene-editing workflow in collaboration with iotaSciences following the protocol in Ludwik *et al.* [23] On d-1, KOLF2-C1 were suspended in StemFlex + 1X CloneR2 and plated (20,000 cells/well) into two wells of a tissue-culture-treated 6-well plate that had been precoated with Biolaminin 521, and incubated overnight. On d0, transfection was carried out using the Neon™ Nucleofector and Neon™ Transfection system 10 µL kit (Invitrogen). RNP comprised 2 µL MYBPC3 G>GG gRNA that targets exon 24 (target sequence AGGACTCCTGCACAGTACAG), 0.5 µL Cas9 (both Integrated DNA Technologies) and 12.5 µL Buffer R (ThermoFisher). Cells were harvested from one well of a 6-well plate, transferred to a microcentrifuge tube and resuspended in 10 µL Buffer R. Cells were then electroporated (tip size 10 µL, pulse voltage 1200V, pulse width 30 ms, 1 pulse), and plated in a 6-well plate coated with Biolaminin 521 in StemFlex + 0.5X CloneR2. Sub-cultured wild-type (control) cells were plated in an additional well and media replaced daily.

To assess the edit efficiency in the pool of transfected cells, a whole-cell lysate was prepared on d3. Media was removed and 25 µL lysis buffer (made by adding 2.5 µL DNARelease to 100 µL dilution buffer – both from ThermoFisher) added per well, then incubated (2 min) at room temperature. Cell lysate was collected and transferred to a PCR tube, incubated (98ºC, 2 min), spun down, and the supernatant stored at -20ºC. PCR was then carried out using Phire Tissue Direct PCR MasterMix kit (ThermoFisher) and a MiniAmp™ Thermal Cycler (Applied Biosystems) using MYBPC3 G>GG forward (sequence CAGCCTGTGGCGGTTAGTT) and reverse (sequence CGCTTCATGACTCAGCTCCT) primers, following the manufacturer's protocol [35]. Purified human genomic DNA (Promega) and water were used as positive and negative controls. PCR products were purified using the GeneJET PCR Purification Kit (ThermoFisher) following the manufacturer's protocol [37].

Finally, 5 µL of the purified PCR product + 5 µL forward primer MYBPC3 G>GG (10 µM) were sent to Source Biosciences (Source Bioscience Limited, Nottingham, UK) for Sanger sequencing and determination of knockout efficiency in the pool using the ICE (inference of CRISPR edits) tool [38].

On d4, 5 µL drops (Biolaminin 521) were deposited into the inner wells of a tissue-culture-treated 96-well plate, incubated (2 h), and volume withdraw as done in previous cloning tests. A suspension of the edited cell pool (2 cells/µL) was prepared in StemFlex + 1X CloneR2, and 0.5 µL suspension added to flat drops, which were then imaged and wells flooded with media. Wells containing a single cell were identified, and media changed daily thereafter. On d11, colonies were identified and cloning efficiency calculated. On d14, 12 of the clones were selected and target regions in each amplified using the sequencing primer (as on d3) and sequenced (Source Biosciences). Sequences obtained are shown in **Figure S6** [p. 52]**.**

Imaging

Drops containing HEK, LNCaP and CHO-S and subsequent colonies were imaged using a standard inverted microscope (Olympus IX53) and coupled DSLR camera (Nikon D610). Drops containing iPSCs and subsequent colonies were imaged using an inverted microscope (isoHub, iotaSciences) and attached camera (MC203CG-SY-UN, xiC, ximea). Image processing and analysis was done in FIJI (imageJ) [34].

Calculations and statistical analysis

All calculations (e.g., drop geometry, effect on adding/removing drop volume on contact angle) and statistical analysis (e.g., maximum likelihood estimation for fitting Poisson distribution to data) were performed in either Excel (Version 2404, Microsoft) or MATLAB (2023a, Mathworks).

Acknowledgements

The authors thank iotaSciences (iota Sciences Ltd, Begbroke Science Park, Oxfordshire, OX5 1PF) and in particular, Ann Na Tan for the culture and preparation of iPSCs used in experiments, and performing the CRISPR gene-edit. iotaSciences also provided a Scholarship for J.A.E.M.

References

[1] S. Chen *et al.*, 'Single-cell analysis technologies for cancer research: from tumor-specific single cell discovery to cancer therapy', *Front. Genet.*, vol. 14, Oct. 2023,

[2] L. Heumos *et al.*, 'Best practices for single-cell analysis across modalities', *Nat Rev Genet*, vol. 24, no. 8, pp. 550–572, Aug. 2023

[3] S. A. Fuller, M. Takahashi, and J. G. R. Hurrell, 'Cloning of Hybridoma Cell Lines by Limiting Dilution', *Current Protocols in Molecular Biology*, vol. 1, no. 1, p. 11.8.1-11.8.2, 1988

[4] C. Soitu, C. Deroy, A. A. Castrejón-Pita, P. R. Cook, and E. J. Walsh, 'Using Fluid Walls for Single-Cell Cloning Provides Assurance in Monoclonality', *SLAS TECHNOLOGY: Translating Life Sciences Innovation*, vol. 25, no. 3, pp. 267–275, June 2020

[5] P. Hu, W. Zhang, H. Xin, and G. Deng, 'Single Cell Isolation and Analysis', *Frontiers in Cell and Developmental Biology*, vol. 4, 2016, Accessed: July 21, 2022. [Online]. Available: https://www.frontiersin.org/articles/10.3389/fcell.2016.00116

[6] J. Ge *et al.*, 'Standard fluorescent imaging of live cells is highly genotoxic', *Cytometry Part A*, vol. 83A, no. 6, pp. 552–560, 2013

[7] D.-K. Kang, M. Monsur Ali, K. Zhang, E. J. Pone, and W. Zhao, 'Droplet microfluidics for single-molecule and single-cell analysis in cancer research, diagnosis and therapy', *TrAC Trends in Analytical Chemistry*, vol. 58, pp. 145–153, June 2014

[8] W. Zhou *et al.*, 'Microfluidics applications for high-throughput single cell sequencing', *Journal of Nanobiotechnology*, vol. 19, no. 1, Art. no. 1, Oct. 2021

[9] G. M. Whitesides, ‘The origins and the future of microfluidics’, *Nature*, vol. 442, no. 7101, pp. 368–373, July 2006

[10] J. L. Garcia-Cordero and Z. H. Fan, ‘Sessile droplets for chemical and biological assays’, *Lab Chip*, vol. 17, no. 13, Art. no. 13, June 2017

[11] A. Prastowo, P. R. Cook, and E. J. Walsh, ‘Biocompatibility of Sessile Drops as Chambers for Cell Culture’, in *2019 2nd International Conference on Bioinformatics, Biotechnology and Biomedical Engineering (BioMIC) - Bioinformatics and Biomedical Engineering*, Sept. 2019, pp. 1–5

[12] A. R. Liberski, J. T. Jr. Delaney, and U. S. Schubert, ‘“One Cell−One Well”: A New Approach to Inkjet Printing Single Cell Microarrays’, *ACS Comb. Sci.*, vol. 13, no. 2, pp. 190–195, Mar. 2011

[13] C. Soitu *et al.*, ‘Microfluidic chambers using fluid walls for cell biology’, *PNAS*, vol. 115, no. 26, Art. no. 26, June 2018

[14] E. J. Walsh *et al.*, ‘Microfluidics with fluid walls’, *Nat Commun*, vol. 8, no. 1, p. 816, Oct. 2017

[15] J.-W. Song and L.-W. Fan, ‘Temperature dependence of the contact angle of water: A review of research progress, theoretical understanding, and implications for boiling heat transfer’, *Advances in Colloid and Interface Science*, vol. 288, p. 102339, Feb. 2021

[16] G. Gstraunthaler, T. Lindl, and J. van der Valk, ‘A plea to reduce or replace fetal bovine serum in cell culture media’, *Cytotechnology*, vol. 65, no. 5, pp. 791–793, Oct. 2013

[17] N. Bhargava, P. Thakur, T.P. Muruganandam, *et al.* ‘Development of an efficient single-cell cloning and expansion strategy for genome edited induced pluripotent stem cells.’ *Mol Biol Rep* vol. 49, pp. 7887–7898, May 2022.

[18] Y. Chen, S.M. Pruett-Miller. ‘Improving single-cell cloning workflow for gene editing in human pluripotent stem cells.’ Stem Cell Research, vol.31, pp. 186-192, Aug. 2018

[19] X. Zhang, S. Zhang, and T. Wang, ‘How the mechanical microenvironment of stem cell growth affects their differentiation: a review’, *Stem Cell Research & Therapy*, vol. 13, no. 1, p. 415, Aug. 2022

[20] J.S. Draper, C. Pigott, J.A. Thomson, and P.W. Andrews. ‘Surface antigens of human embryonic stem cells: changes upon differentiation in culture’, *Journal of Anatomy*, vol. 200, pp.249-258, April 2002

[21] L. Carrier, G. Mearini, K. Stathopoulou, and F. Cuello, ‘Cardiac myosin-binding protein C (MYBPC3) in cardiac pathophysiology’, *Gene*, vol. 573, no. 2, pp. 188–197, Dec. 2015

[22] S. Lalonde *et al.*, ‘Frameshift indels introduced by genome editing can lead to in-frame exon skipping’, *PLoS One*, vol. 12, no. 6, p. e0178700, June 2017

[23] K. A. Ludwik, N. Telugu, S. Schommer, H. Stachelscheid, and S. Diecke, ‘ASSURED-optimized CRISPR protocol for knockout/SNP knockin in hiPSCs’, *STAR Protoc*, vol. 4, no. 3, p. 102406, July 2023

[24] K. Bryant, ‘Guide to Understanding CRISPR Data Analysis Scores’, Synthego. Accessed: Jan. 22, 2025. [Online]. Available: https://www.synthego.com/blog/crispr-knockout-score

[25] A. Prastowo, ‘Cell-based assays in flowing and sessile drops’, http://purl.org/dc/dcmitype/Text, University of Oxford, 2019. Accessed: Aug. 16, 2022. [Online]. Available: https://ora.ox.ac.uk/objects/uuid:9013838b-d97e-4dd1-833b-0b464fe96b38

[26] V. V. Berejnov, ‘Self-pinning protein-laden drops’, *Journal of Colloid and Interface Science*, vol. 322, no. 1, Art. no. 1, June 2008.

[27] D. W. Jayme and S. R. Smith, ‘Media formulation options and manufacturing process controls to safeguard against introduction of animal origin contaminants in animal cell culture’, *Cytotechnology*, vol. 33, no. 1–3, pp. 27–36, July 2000

[28] M. Taverna, A.-L. Marie, J.-P. Mira, and B. Guidet, ‘Specific antioxidant properties of human serum albumin’, *Annals of Intensive Care*, vol. 3, no. 1, p. 4, Feb. 2013

[29] F. L. Graham, J. Smiley, W. C. Russell, and R. Nairn, ‘Characteristics of a human cell line transformed by DNA from human adenovirus type 5’, *J Gen Virol*, vol. 36, no. 1, pp. 59–74, July 1977

[30] J. S. Horoszewicz *et al.*, ‘LNCaP model of human prostatic carcinoma’, *Cancer Res*, vol. 43, no. 4, pp. 1809–1818, Apr. 1983.

[31] M. Kito, S. Itami, Y. Fukano, K. Yamana, and T. Shibui, ‘Construction of engineered CHO strains for high-level production of recombinant proteins’, *Appl Microbiol Biotechnol*, vol. 60, no. 4, pp. 442–448, Dec. 2002

[32] J. Zhu, J. W. Wooh, J. J. C. Hou, B. S. Hughes, P. P. Gray, and T. P. Munro, ‘Recombinant human albumin supports single cell cloning of CHO cells in chemically defined media’, *Biotechnology Progress*, vol. 28, no. 3, pp. 887–891, 2012

[33] C. B. Pantazis *et al.*, ‘A reference human induced pluripotent stem cell line for large-scale collaborative studies’, *Cell Stem Cell*, vol. 29, no. 12, pp. 1685-1702.e22, Dec. 2022

[34] C. A. Schneider, W. S. Rasband, and K. W. Eliceiri, ‘NIH Image to ImageJ: 25 years of image analysis’, *Nat Methods*, vol. 9, no. 7, pp. 671–675, July 2012

[35] ‘Basic Research Standards’, International Society for Stem Cell Research. Accessed: Jan. 21, 2025. [Online]. Available: https://www.isscr.org/basic-research-standards

[36] ‘Thermo Scientific Phire Tissue Direct PCR Master Mix Product Information’. Thermo Fisher Scientific, 2015. Accessed: Jan. 29, 2025. [Online]. Available: https://assets.thermofisher.com/TFS-Assets/LSG/manuals/F-170_QR_TS_5.pdf

[37] ‘Thermo Scientific GeneJET PCR Purification Kit User Guide’. Thermo Fisher Scientific, 2015. Accessed: Jan. 29, 2025. [Online]. Available: https://assets.thermofisher.com/TFS-Assets/LSG/manuals/MAN0012662_GeneJET_PCR_Purification_UG.pdf

[38] D. Conant *et al.*, ‘Inference of CRISPR Edits from Sanger Trace Data’, *The CRISPR Journal*, vol. 5, no. 1, pp. 123–130, Feb. 2022

Supplementary information

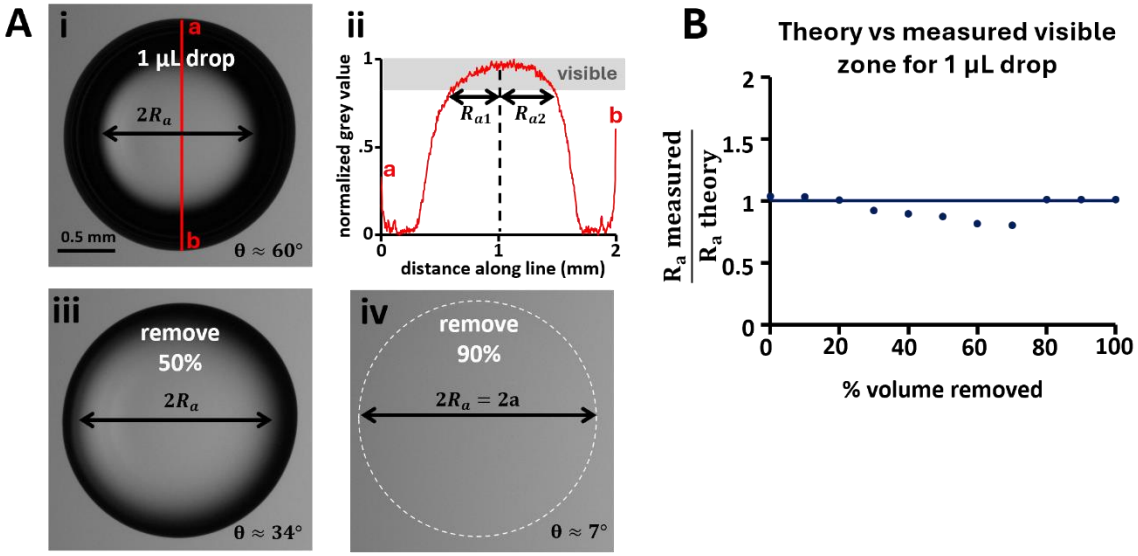

Fig. S1. Drop optics theory validation.

(A) A 1 µL drop of PBS + 0.5 mg/mL BSA is deposited on a dish (**i**); it has dark (optically inaccessible regions at the drop periphery). The radius of the visible area (Ra) is determined by plotting the grey values along a vertical line through the drop center (**ii**); the visible boundary was defined as a 15% decrease in pixel intensity compared to the center of the drop. Removing 50% of the volume (**iii**) reduces the angle of incidence and therefore total refraction, shrinking the dark zone. Removing 90% of the volume (**iv**) gives clear optics across the entire footprint (pinning line highlighted, images taken in brightfield using 4X objective).

(B) Comparison between the predicted radius of visible area and experimental measurement supports the theory with reasonable accuracy.

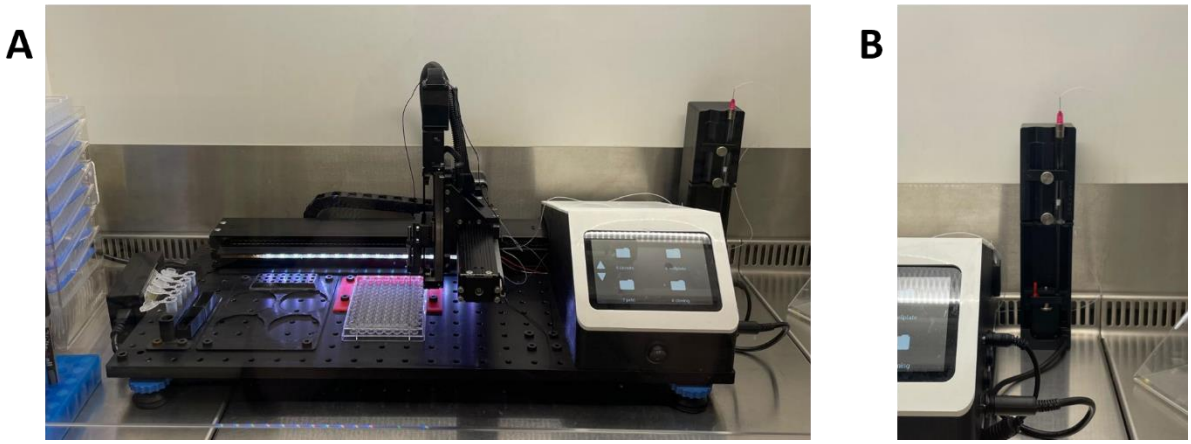

Fig S2. Automated 3-axis traverse and syringe pump.

(A) Fluid handling was controlled via a programmable 3-axis traverse and syringe pump. Image shows system in laminar flow hood. Microtubes are loaded on the left, a microtiter plate in the middle and commands selected using the touchscreen interface on the right. System provided by iotaSciences.

(B) Zoomed image of the programmable syringe pump.

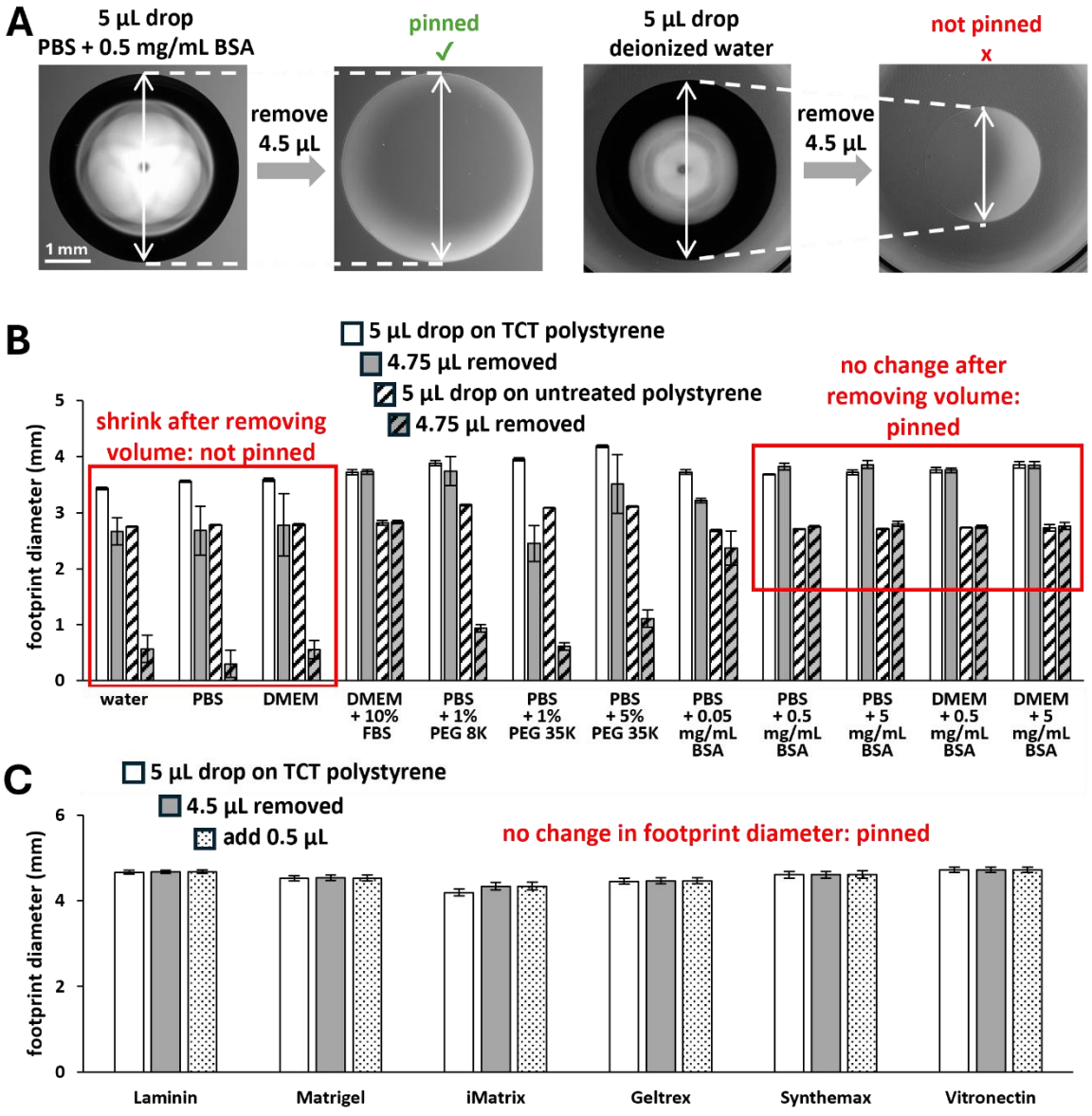

D

Coating	Normal conc. for 96W	Normal volume per well (µL)	Drop conc.	Drop volume (µL)	Saving
Laminin	2.29 µg/mL	70	8 µg/mL	5	75%
Matrigel	228 µL/mL	70	800 µL/mL	5	75%
iMatrix	0.32 µL/mL	100	0.32 µL/mL	5	0%
Geltrex	5.925 µL/mL	100	14.9 µL/mL	5	75%
Synthemax	25 µg/mL	100	125 µg/mL	5	75%
Vitronectin	1.6 µg/mL	100	8 µg/mL	5	75%

Fig. S3. Drop footprint analysis.

(A) A drop on tissue-culture-treated polystyrene imaged from below. Removing volume from a drop of laminin does not cause a reduction in footprint diameter; the footprint remains pinned at the original position. Removing volume from a drop of deionized water causes a clear reduction in footprint diameter (as the pinning line retracts).

(B) Fluids were evaluated to determine whether they are pinned on both treated and untreated polystyrene.

(C) Matrix coatings were assessed for any change in footprint diameter after removing and adding volume.

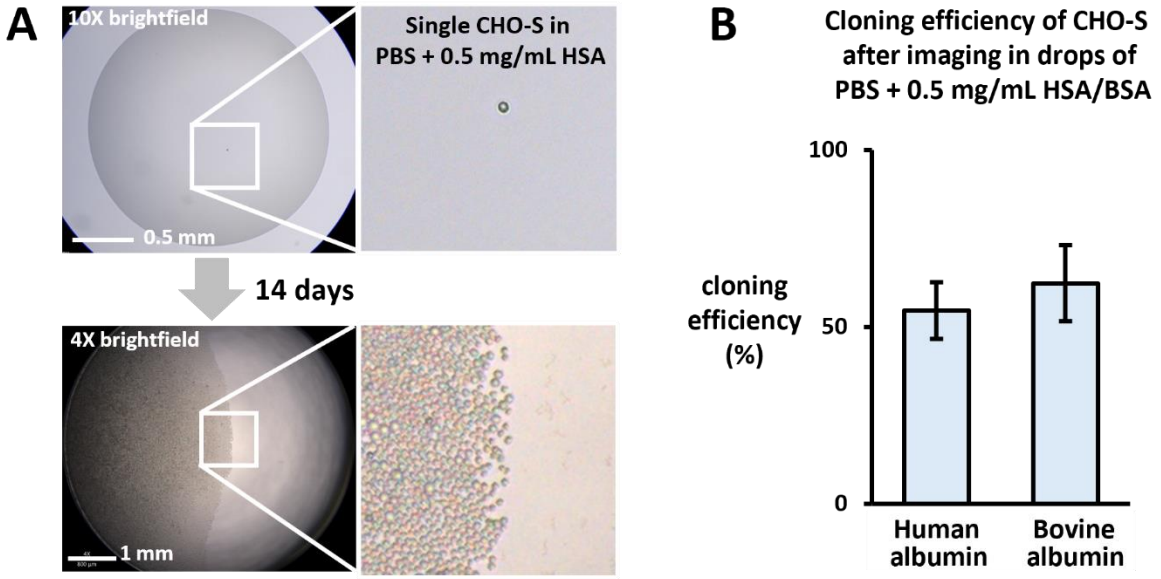

Fig. S4. Imaging CHO-S in drops containing bovine vs human serum albumin (HSA)

(A) Drops of PBS + 0.5 mg/mL HSA are pinned on polystyrene surfaces, allowing creation of drops with low contact angles and excellent optics required for single-cell imaging. A single CHO-S is clearly identified and grows into a colony in a non-treated (suspension) microtiter well.

(B) There is no significant difference in cloning efficiency after imaging CHO-S in drops containing HSA vs BSA ($p = 0.37$, Welch's two-sample t-test).

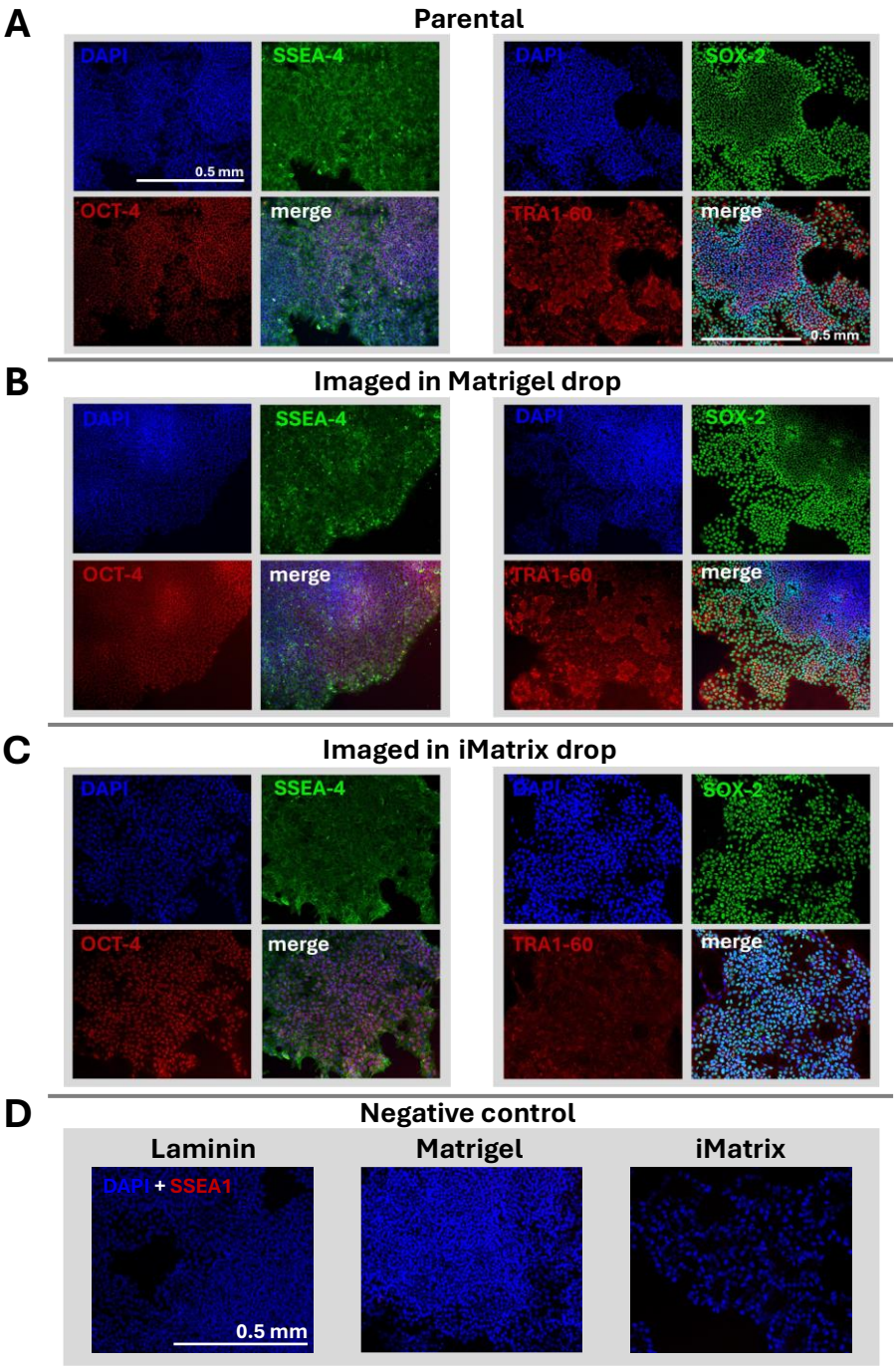

Fig. S5. Immunofluorescence detection of pluripotency markers (SSEA-4/OCT-4 and SOX-2/TRA1-60) in two derived clones grown from single cells imaged in flat drops, and the parental (KOLF2-C1) stem-cell line.

(A) Parental cells.

(B, C) Colonies from a single iPSC grown after imaging in a drop of Matrigel or iMatrix. Pluripotency markers continue to be expressed.

(D) For each matrix coating, staining for SSEA-1 was used as a negative control.

A

CRISPR gene-edit	
Knock-out efficiency	**75%**
Cloning	
Single cells identified in drops	61
Colonies from single cell	46
Cloning efficiency	**75%**
Clones sequenced	12
Edited clones	11

B

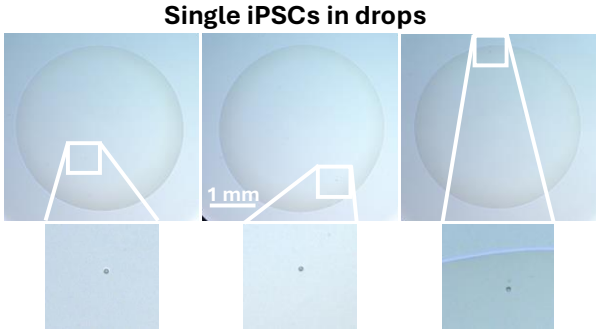

C

MYBPC3 sgRNA

	Parental	A	G	G	A	C	T	C	C	T	G	C	A	C	A	G	T	A	C	A	G
Clone	1	A	G	G	A	C	T	C	C	T	-	-	-	-	-	-	-	-	-	-	-
	2	A	G	G	A	C	T	C	C	T	G	C	A	C	-	-	-	-	-	A	G
	3	A	G	G	A	C	T	C	C	T	G	C	A	C	A	G	A	c	T	c	c
	4	A	G	G	A	C	T	C	C	T	G	C	A	C	A	G	T	A	C	A	G
	5	A	G	G	A	C	T	C	C	T	G	C	A	C	-	-	-	-	-	A	G
	6	A	G	G	A	C	T	C	C	T	G	C	A	C	A	-	-	-	-	-	G
	7	A	G	G	A	C	T	C	C	T	G	C	A	C	-	-	-	-	-	A	G
	8	A	G	G	A	C	T	C	C	T	G	C	A	C	A	G	T	-	-	-	A
	9	A	G	G	A	C	T	C	C	T	G	C	A	C	-	-	-	-	-	A	G
	10	A	G	G	A	C	T	C	C	T	G	C	a	t	a	c	g	a	t	g	a
	11	A	G	G	A	C	T	C	C	T	G	c	a	c	a	c	t	A	t	g	G
	12	A	G	G	A	C	T	C	C	T	G	C	A	C	A	-	-	-	-	-	G

Fig. S6. Integration into a CRISPR gene-edit workflow.

Single stem cells were grown on Biolaminin, and cloning efficiency determined on d7.

(A) Key figures from our workflow.

(B) Example images of single cells in flat drops. Clear drop optics provide an excellent view of a single cell, right up to the drop edge.

(C) Target MYBPC3 sequence of the guide RNA (blue background). Twelve clones were selected, and their target DNA amplified and sequenced. Eleven of the 12 contained edits (highlighted in brown).

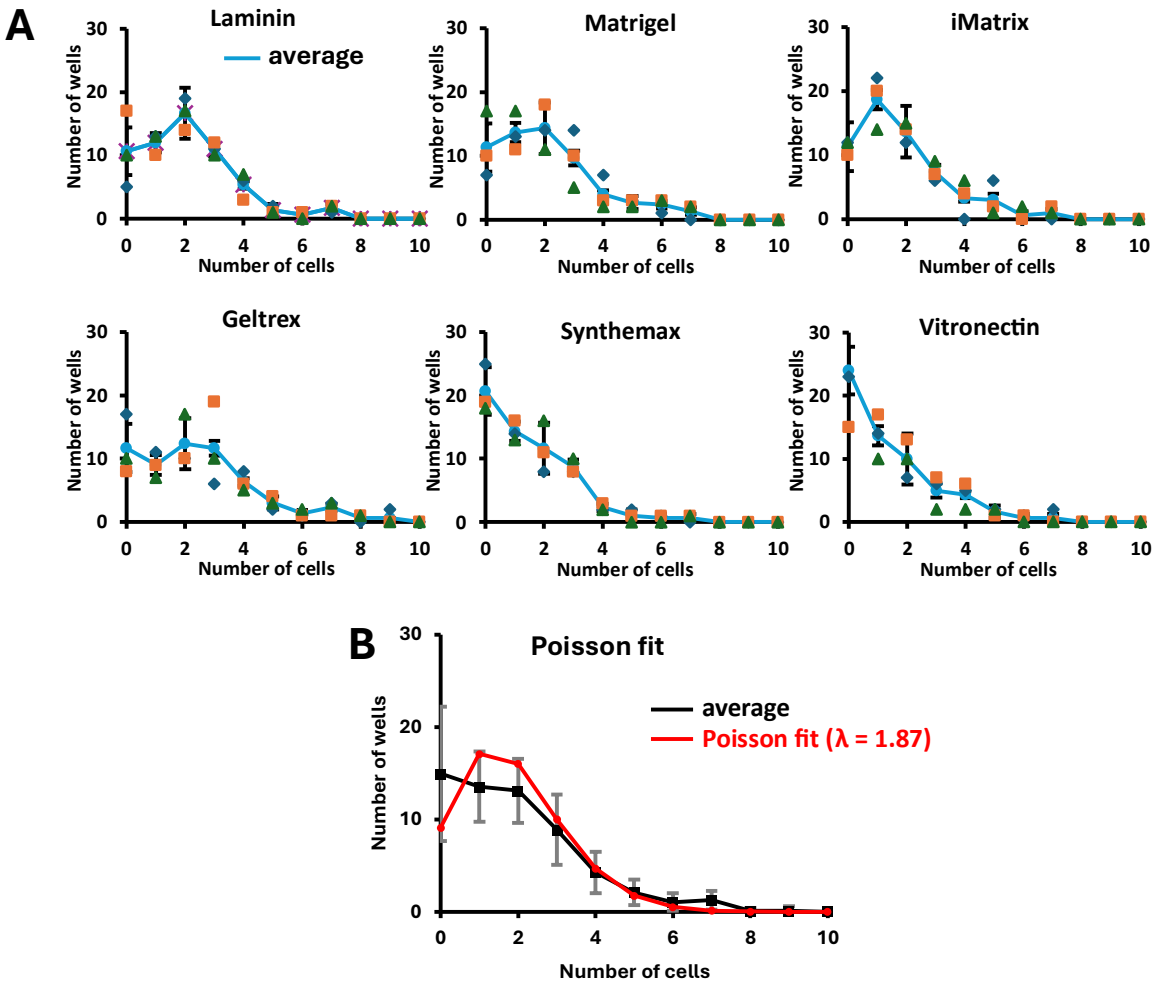

Fig. S7. Cells deposited per well.

(A) Numbers of wells with 0-10 cells for each matrix coating tested. Each graph contains results from three 96-well plates (excluding peripheral wells; different colors show results for different plates).

(B) All six plots merged and average plotted (± SD). A maximum likelihood estimation was used to fit the Poisson distribution to the data, giving an estimate of the average number of cells infused into each well.

Statement of Authorship for joint/multi-authored papers for PGR thesis

To appear at the end of each thesis chapter submitted as an article/paper

The statement shall describe the candidate's and co-authors' independent research contributions in the thesis publications. For each publication there should exist a complete statement that is to be filled out and signed by the candidate and supervisor **(only required where there isn't already a statement of contribution within the paper itself).**

Title of Paper	Generation of Clonal Cultures of Adherent or Suspension Cells Using Flat Sessile Drops for Assurance of Monoclonality
Publication Status	Published
Publication Details	Joseph A.E. Morgan, Peter R. Cook, Alfonso A. Castrejón-Pita, Edmond J. Walsh Biotechnology and Bioengineering 122 (10), 2739-2750 (July 19, 2025)

Student Confirmation

Student Name	Joseph Morgan		
Contribution to the Paper	Lead Author Designed experiments in discussion with co-authors, performed experiments, collected and analysed data, prepared figures and manuscript, responded to reviewers and implemented changes.		
Signature 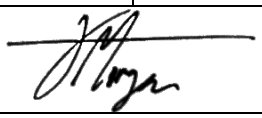		Date	07/01/2026

Supervisor Confirmation

By signing the Statement of Authorship, you are certifying that the candidate made a substantial contribution to the publication, and that the description described above is accurate.

Supervisor name and title: Prof. Edmond J. Walsh		
Supervisor comments		
Signature Ed Walsh	Date	7th Jan 2026

This completed form should be included in the thesis, at the end of the relevant chapter.

Chapter 4: Identification and isolation of migratory subpopulations of cancer cells using microfluidics with fluid walls

Authors: Joseph A.E. Morgan, Daniele T. Cotton, Srinivasa R. Rao, Peter R. Cook, James R. Edwards, Alfonso A. Castrejón-Pita, Claire M. Edwards and Edmond J. Walsh

Abstract

Metastasis of prostate cancer cells to the bone is a major clinical challenge, and various microfluidic assays have been developed to investigate it. However, adoption by biologists is limited due to complex fabrication and operation methods combined with difficulty to retrieve cells of interest. We jet-print dumbbell-shaped microfluidic arrangements with fluid walls in standard Petri dishes in seconds using normal growth media and immiscible oil. Prostate cancer cells and chemoattractant (serum) are introduced into each end using local transient differences in Laplace pressure to enable spatial confinement. Chemotaxis towards serum is monitored using standard microscopes, as the confining fluid walls are optically transparent. Distinct sub-populations of migratory cells possess different morphologies and motilities, assessed using a custom machine-learning segmentation model. Then, we leverage the reconfigurability of fluid walls to isolate and retrieve rapidly-migrating cells. This demonstrates that fluid-walled microfluidics is a versatile and accessible approach for studying cancer cell migration at single-cell resolution, presenting new opportunities for studying metastatic heterogeneity.

Introduction

Cell migration is a critical step during metastasis. In prostate cancer, cells shed from the primary tumour can invade surrounding tissue, enter blood vessels, and disseminate throughout the body (**Figure 1A**) [1]. A frequently-cited study reports that 90% of men who die from prostate cancer also exhibit bone metastases [2]. Consequently, many *in vitro* migration assays have been developed, e.g., involving transwells, Dunn chambers, wound-healing, and complex matrices; [3 - 7]. However, such methods are often limited: for example, transwell assays provide little information on cell morphology, and wound-healing assays are generally unsuitable for studying chemotaxis [8].

Microfluidic approaches have emerged as promising alternatives especially for high-throughput assays, providing greater flexibility in assay design and enabling real-time monitoring of directed migration through microchannels [9] [10]. These platforms allow for precise control over cellular microenvironments and have deomonstrated the presence of distinct migratory cancer cell subpopulations alongside non-migratory cells [11] [12] [13]. In some cases, microfluidic systems facilitate isolation and retrieval of migratory cells, enabling downstream comparisons that have demonstrated increased metastatic potential in vivo compared to non-migratory cells [13]. However, such approaches are typically limited to low-resolution classification (for example, migratory or non-migratory) as cells are often pooled during retrieval, restricting analysis of heterogeneity within migratory subpopulations. Furthermore, custom microfluidic devices are commonly fabricated using polydimethylsiloxane (PDMS) and lithography-based methods which are time- and labour-intensive and produce enclosed systems with limited access to cells. Open-microfluidic systems partially address these limitations by improving accessibility [14] [15] but often rely on similarly complex fabrication techniques that may present a barrier to many biologists [16].

Fluid-walled microfluidics offers an effective solution – cells are contained by immiscible fluids that form liquid interfaces rather than solid walls [17]. Spatially distinct culture systems can be formed using standard cell-culture media and confined by the immiscible and bio-inert

fluorocarbon oil, FC40 – their geometry is maintained by interfacial forces. FC40 is chemically stable, optically transparent, gas-permeable, and been shown to support the long-term culture of a wide variety of cell types when overlaid [18] [19] [20]. Such culture systems can be made in seconds on standard tissue-cultureware, and – as confining walls are liquid and transparent – they are easily pierced with pipettes so that all regions are fully accessible. Moreover, culture systems can be reconfigured during assay to allow isolation and retrieval of cells of interest [21]. The advantages of using fluid-walled microfluidics in cell migration studies have been demonstrated in assays of macrophage and bacterial chemotaxis [22] [23].

We present a fluid-walled assay to study the migration of PC3 prostate-cancer cells, derived from a cancer that metastasised to bone [24]. PC3 have high metastatic potential and have been used previously in various migration assays [25] [26] [27]. We jet-print arrays of fluid-walled microfluidic arrangements shaped like dumbbells, each comprising two chambers connected by a narrow fluid conduit. Modulating local volumes directly alters height, but not footprint, and hence local pressures. In our system, geometries are sufficiently small that interfacial forces outweigh gravitational ones (Bond number < 1), and dumbbell dynamic behaviour is governed by gradients in Laplace pressure; adding or withdrawing volume enables control over flow direction [18] [28]. We exploit pressure gradients to confine cells and chemo-attractant (foetal bovine serum, FBS [29]) to respective chambers [18].

Over 3 days, cells migrate through the conduit towards FBS. We then identify sub-populations of highly-migratory cells, which likely represent cells with a higher metastatic potential compared to non-migrating ones [12] [13]. We then reconfigure the fluid walls – a process unique to this method, to isolate the highly migratory cells from the majority and retrieve them.

The accessibility of machine-learning tools for cell segmentation is advancing rapidly [30]. We trained a custom model using Cellpose-SAM [31], a framework that combines the strong generalization of Cellpose with the Segment Anything Model [32] to automate tracking of individual cells and elucidate cell characteristics. This uncovered striking morphological

heterogeneity in migrating sub-populations. In summary, we demonstrate the versatility of fluid-walled microfluidics for studying single-cell migration and subsequently apply this platform to identify and characterize heterogenous sub-population of migratory cancer cells.

Experimental setup

Jet-printing dumbbells with fluid walls

Dumbbells were fabricated on standard 60 mm polystyrene culture dishes using a modified fluid printer (isoCell, iotaSciences, images included in supplementary **Figure S1** [p. 90]). First, the dish was coated with a thin layer of medium (1 mL, withdrawn manually to leave a thin film) and overlaid with 3 mL of the immiscible fluorocarbon, FC40. A submerged microjet of FC40 was then used to sweep a path through the underlying medium, leaving behind stable FC40 fluid walls held in place by interfacial forces (**Figure 1B**). This process is referred to as jet-printing [33]. FC40 is bio-inert, permeable to gasses, and has refractive index close to water, making it well-suited to live-cell culture and imaging [34]. The jet path was controlled by a three-axis traverse, enabling rapid generation of any two-dimensional (2D) pattern. Using this approach, we produced an array of 80 dumbbells (5 columns, 20 rows) in ~ 30 s (**Figure 1C, D**). Each dumbbell consisted of two chambers (1.8 mm x 1.8 mm) connected by a narrow conduit (1 mm length, 0.2 mm width). Since dumbbells are confined by a fluid-fluid interface, all regions are fully accessible. After lowering a dispensing needle (connected to a syringe pump, controlled via the fluid printer) through the interface, media can be infused/withdrawn locally into/from each chamber independently (**Figure 1Ei**, see red and blue dye). This approach can be used to seed cells in one chamber and deliver chemo-attractant to the other (**Figure 1Eii**). Dumbbells were fabricated using medium + 0.5% FBS, which we found to be the minimum concentration required to ensure stable fluid walls (supplementary **Figure S2** [p. 91]).

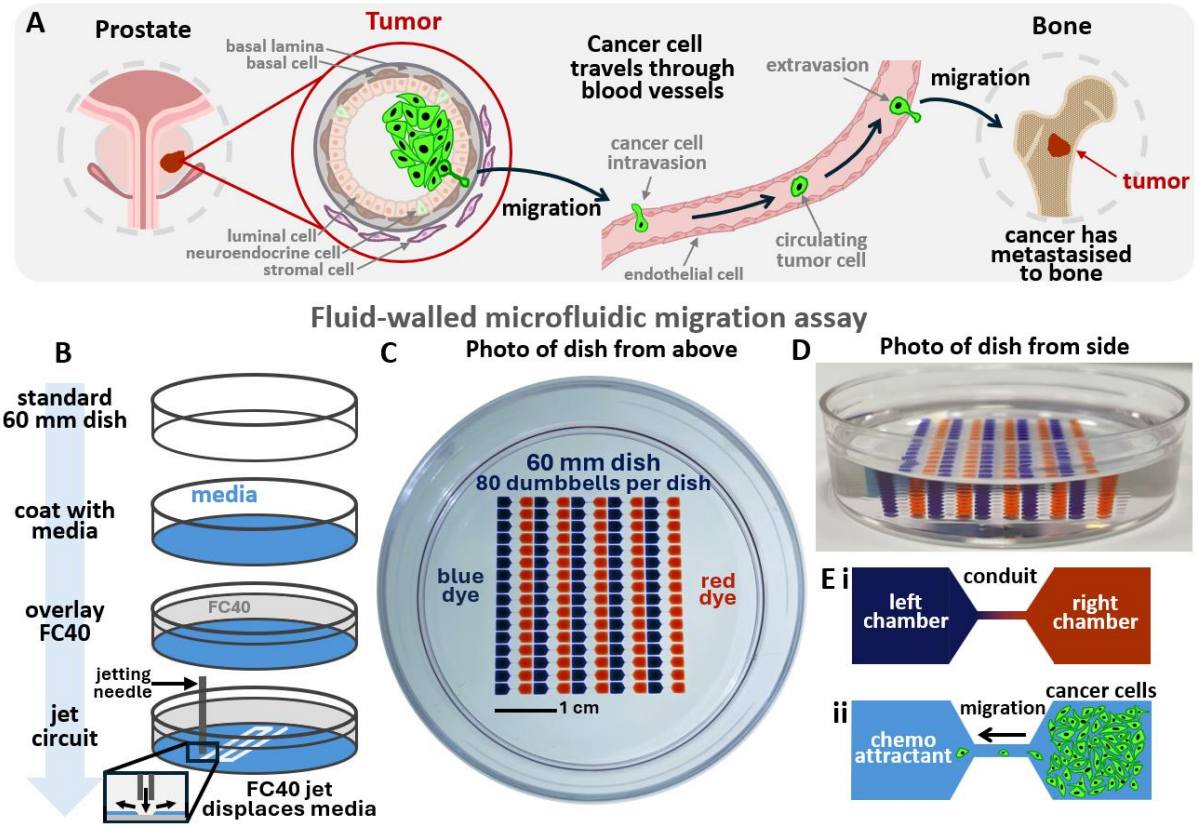

Figure 1. A fluid-walled microfluidic assay for cell migration. (A) Primary prostate tumors can metastasise to the bone via cell migration and intra-/extra-vasion through the bloodstream. **(B)** To study this process, we engineered fluid-walled microfluidic dumbbells. A thin film of culture medium covered a standard 60 mm dish, FC40 fluorocarbon was overlaid, and FC40 jetted through the medium to create fluid walls. **(C)** 80 dumbbells were fabricated on a single 60 mm dish. Image shows red and blue dyes in opposing chambers (top-down image acquired with an iPhone camera). **(D)** Side-on photo of dish. Dumbbells are pinned to the polystyrene surface under FC40. **(E)** Chambers can be addressed independently. For example, **(i)** dyes for visualisation, or **(ii)** seeding cells in one chamber and introducing a chemo-attractant in the other.

Controlling flow in microfluidics with fluid walls

Unlike conventional microfluidic systems bounded by solid walls, fluid walls – while tightly pinned to the underlying substrate – are free to morph when media is added or withdrawn. Consequently, regions within a dumbbell may have different radii of curvature depending on local volumes, and hence different pressure rises across the fluid interface - Laplace pressures – which are given by:

$$P_L = \gamma\left(\frac{1}{R_1} + \frac{1}{R_2}\right) \quad (1)$$

In the case of a small drop deposited on a surface, $P_L = 2\gamma/R$, with R the radius of curvature of the drop and γ the interfacial tension (for DMEM + 10% FBS and FC40, $\gamma = 22.8$ mN/m [35]). By approximating chamber 3D geometry as that of a spherical cap, this can be expressed in terms of chamber heights h and footprint radius a:

$$P_L = \frac{4\gamma h}{a^2 + h^2} \quad (2)$$

and height estimated from the volume V in the chamber [35]:

$$V = \frac{\pi}{6}h(3a^2 + h^2) \quad (3)$$

Consider a dumbbell at equilibrium where both chambers have the same footprint geometry and equal volume with contact angles, θ less than 90º (**Figure 2**). Adding volume to the left chamber will increase chamber height (and reduce the radius of curvature) causing an increase in Laplace pressure. Consequently, this induces flow from the left chamber to the right until pressures in each chamber equilibrate. These principles underpin our ability to exploit circuit dynamics to achieve spatial control within the circuit and create functional migration assays. For further detail regarding circuit pressure dynamics and 3D geometry, see supplementary **Figure S3** [p. 93].

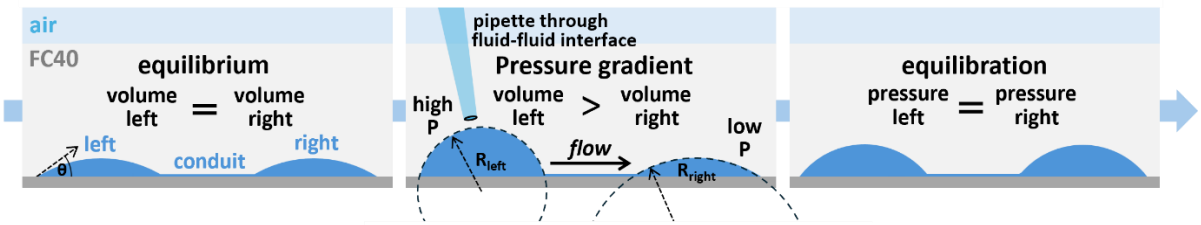

Figure 2. Controlling flow in fluid-walled microfluidics. Two chambers with the same footprint geometry and volume connected by a fluid conduit are at equilibrium. Adding volume to the left chamber causes a local increase in Laplace pressure. This pressure imbalance drives flow from the left to the right chamber until pressures equilibrate.

Results

Enabling spatial confinement of cells and chemoattractant

Following jet printing, displaced medium accumulated within chambers such that each chamber contained ~ 150 nL (estimated by comparing the weight of an empty dish against a dish after adding 1 mL of medium and manually withdrawing to leave a thin film, then calculating μL/mm^2 of medium displaced by the FC40 fluid walls and swept into each dumbbell). To standardize chamber volumes and remove residual serum, dumbbell chambers were washed with 600 nL phosphate buffer saline (PBS). During washing, the estimated peak contact angle was ~ 33^o. Withdrawing more than the chamber volume ensured near-complete removal of medium, while also extracting a small volume of FC40 overlay, thereby minimizing any variability in the volume of media in chambers. The efficacy of the PBS wash in removing residual serum is shown in supplementary **Figure S4** [p. 94]**,** where fluorescent bovine serum albumin, BSA, is used as a surrogate for serum. Following the wash, dumbbells were coated with 100 nL fibronectin solution to promote cell attachment. Next 400 nL serum-free medium was added to the left chamber to generate a pressure gradient driving flow toward the right chamber. A smaller volume of cell suspension (100 nL, ~ 500 PC3 cells, transduced to express enhanced green fluorescent protein, eGFP) was then seeded into the right-hand chamber. The pressure difference between the two chambers ensured flow was from left to right, and this confined inputted cells to their chamber (**Figure 3A).** Individual cells are clearly visible in this chamber. Cells adhered within 3 h. As flow between chambers persisted well beyond this, cells remained in the right-hand chamber (see supplementary **Figure S5** [p. 95] for flow estimations and supplementary **Figure S6** [p. 95] for optimisation of cell seeding number).

Once cells had adhered, the same principles were applied to introduce and confine a chemo-attractant into the left-hand chamber (**Figure 3B**). Here, 200 nL serum-free medium was added to the right-hand chamber containing cells, and 100 nL medium + 20% FBS was added to the left, thus generating flow from right to left (ensuring chemo-attractant was

confined to the left-hand chamber). After ~ 2 hours (approximate chamber equilibration time), serum then diffused into/through the conduit, estimated to establish a stable diffusion gradient after an additional ~ 3.5 hours (which was estimated to remain stable for the duration of the assay) and some cells began to migrate along the concentration gradient from right to left. See supplementary **Figure S7** [p. 97] for estimation of diffusion rates and equilibration times, and **Figure S8** [p. 98] for effect of serum concentration and chamber volume on migration.

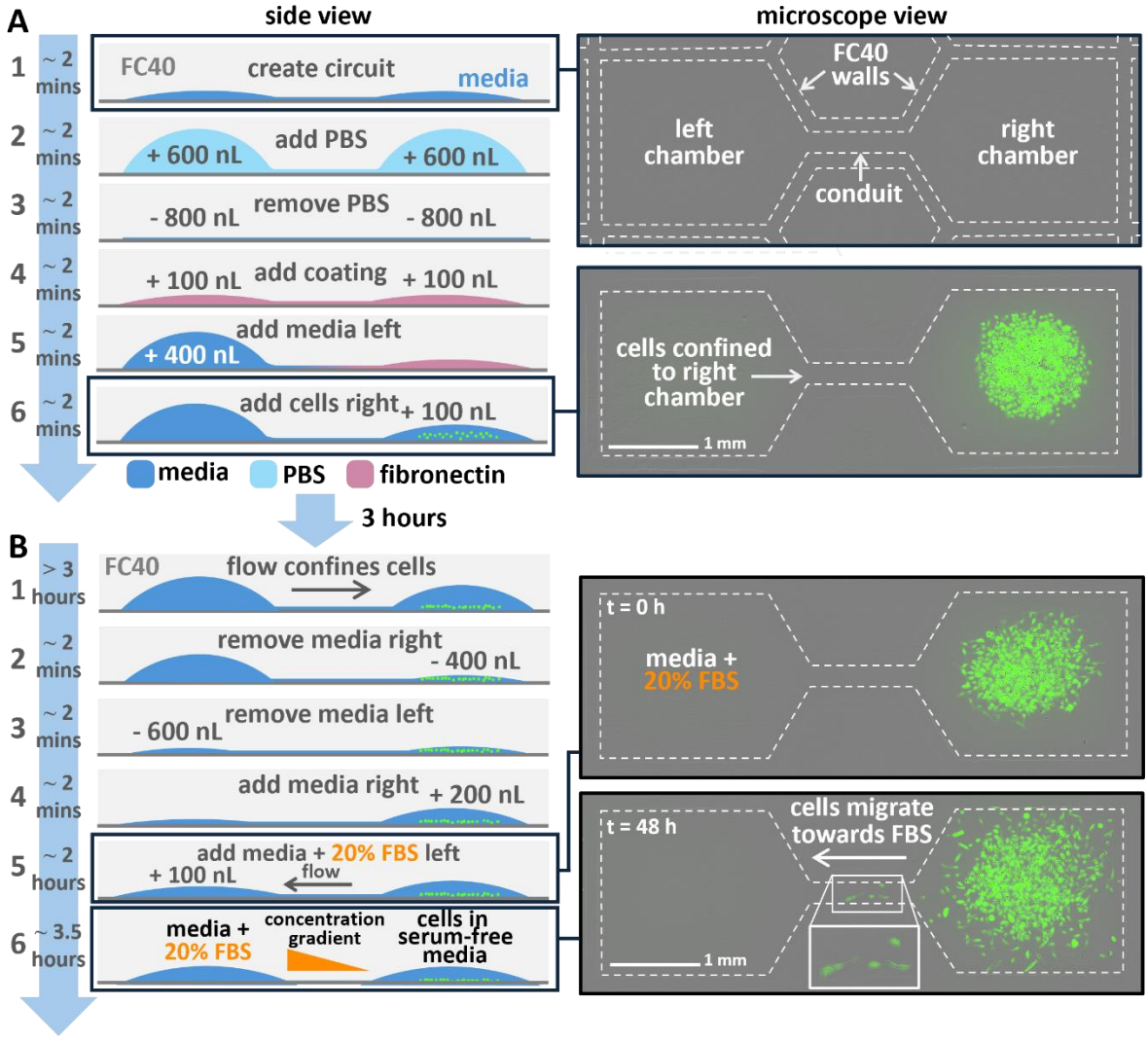

Figure 3. Workflow for introducing cells and chemo-attractant into dumbbells. Low-power fluorescence microscope views of the circuit at the stages indicated are shown on the right. **(A)** (1) Dumbbells were fabricated by jetting FC40 through a thin film of culture media to create fluid walls (image on right), (2,3) washed with PBS, and (4) coated with fibronectin. To confine cells, (5) 400 nL of medium was added to the left chamber to generate a gradient in Laplace pressure, driving flow from left to right. (6) PC3-eGFP cells were now added to the right-hand chamber (fluorescence image on right). Each step took ~ 2 mins to complete, cells were then placed in the incubator for 3 hours to attach.

(B) (1) Differences in Laplace pressure ensure flow is to the right (sustained for > 3 hours), so cells are confined to the right. (2) After 3 h, medium is removed on the right, and (4) medium added to drive flow from right to left and hence initially confine chemo-attractant. (5) Chemo-attractant (media + 20% FBS) was introduced into the left. Differences in chamber volume were used to control flow and confine serum to the left chamber. Flow persisted for ~ 2 hours, after which (6) serum diffused through the conduit, establishing a stable diffusion gradient after ~ 3.5 hours, promoting cell migration to the left. Images on the right show cells migrating towards 20% FBS.

Cell migration through the conduit

Following addition of chemo-attractant, dumbbells were placed in a standard CO_2 incubator and imaged hourly thereafter using an Incucyte live-cell imaging system (phase contrast and fluorescence). The excellent optical properties of dumbbells enabled clear visualization of cell migration through the conduit into the distal chamber [34] (**Figure 4A,** supplementary **Movie S1**). Migrating cells were morphologically heterogeneous compared to non-migrating ones (**Figure 4Bi, ii;** supplementary **Movies S2, S3**).

Analysis of time-lapse image stacks of migrating cells revealed some key migration parameters. Data are presented across 7 biological replicates, with each experiment comprising 120 test dumbbells and 24 control dumbbells (no FBS), distributed equally across four dishes (36 dumbbells per dush, the maximum number visible within the field of view of the imaging system).

In the test condition, cells required at least 24 h to traverse the conduit, with the proportion of dumbbells containing migrated cells increasing steadily over 3 days (**Figure 4Ci**). Migration was significantly greater in the test condition than in the control ($p < 0.01$, Welch's two-sided t-test comparing area under the curve for each independent experiment) indicating that diffusion of FBS through the conduit effectively promotes cell migration. The average time required for a cell to traverse the conduit was typically 2-3 days (**Figure 4Cii**). Comparing the total number of cells in all 36 dumbbells on any dish at the final timepoint **(Figure 4Ciii**) with the number of migrated cells per dish (**Figure 4Civ**) reveals that migrated cells represents 0.03% of the total cell population, averaged across all 7 replicates. It is likely that the yield of

migratory cells could be increased by extending the experimental timescale; however, experiments were terminated after 3 days due to the onset of cell death among non-migratory cells in the serum-free chamber.

There was substantial variability in the time required for the first cell to enter the conduit, with differences of days observed between dumbbells on the same dish (**Figure 4Cv**). In some cases, cells entered the conduit in <5 h – shorter than the time required to establish a stable FBS gradient (~ 6 h) – suggesting that early entry may reflect exploratory behaviour rather than chemotaxis. Approximately 30% of dumbbells contained cells that followed the first through the conduit, followers were deliberately excluded from analysis to focus on the most rapidly-migrating ones.

Migrated cells were morphologically heterogeneous (**Figure 4Cvi**) with areas ranging from 0.00043 mm^2 (smallest) to 0.0139 mm^2 (largest). Of the 119 cells measured, 48 had an area below 0.004 mm^2 and a circularity above 0.8, indicating a substantial fraction of small, round cells at the final timepoint relative to a mid-range value of 0.0067 mm^2. The remaining cells displayed diverse morphologies, including larger, elongated, and irregularly-shaped phenotypes.

It was possible that the proportion of small cells (for example, middle right in **Figure 4Bii**) may be fluorescent vesicles and not cells. To verify that fluorescent bodies were cells, 12 dishes containing a total of 360 test and 72 control dumbbells were fixed post-migration and stained with DAPI to confirm the presence of nuclear material (**Figure 4D**). In all cases, a positive DAPI signal indicated that the entity in the distal chamber was a cell.

Conduit height is dependent on internal Laplace pressure, which is assumed to be equal to the left and right chambers at equilibrium. Under low-volume conditions, this enabled the formation of very shallow conduits (see supplementary **Figure S3** for theory detail [p. 93]). Assuming equilibrated chamber volumes of ~150 nL, equating pressures yielded an estimated conduit height of ~1.3 μm, smaller than the height of adherent PC3 cells (~ 3 – 5 μm [36]).

Comparable channel heights have been reported in systems employing silicone oil-medium interfaces, where deformation of the interface during cell transit was observed [14]. A similar interaction is likely to occur here; interfacial deformation may impose mechanical constraints on migrating cells.

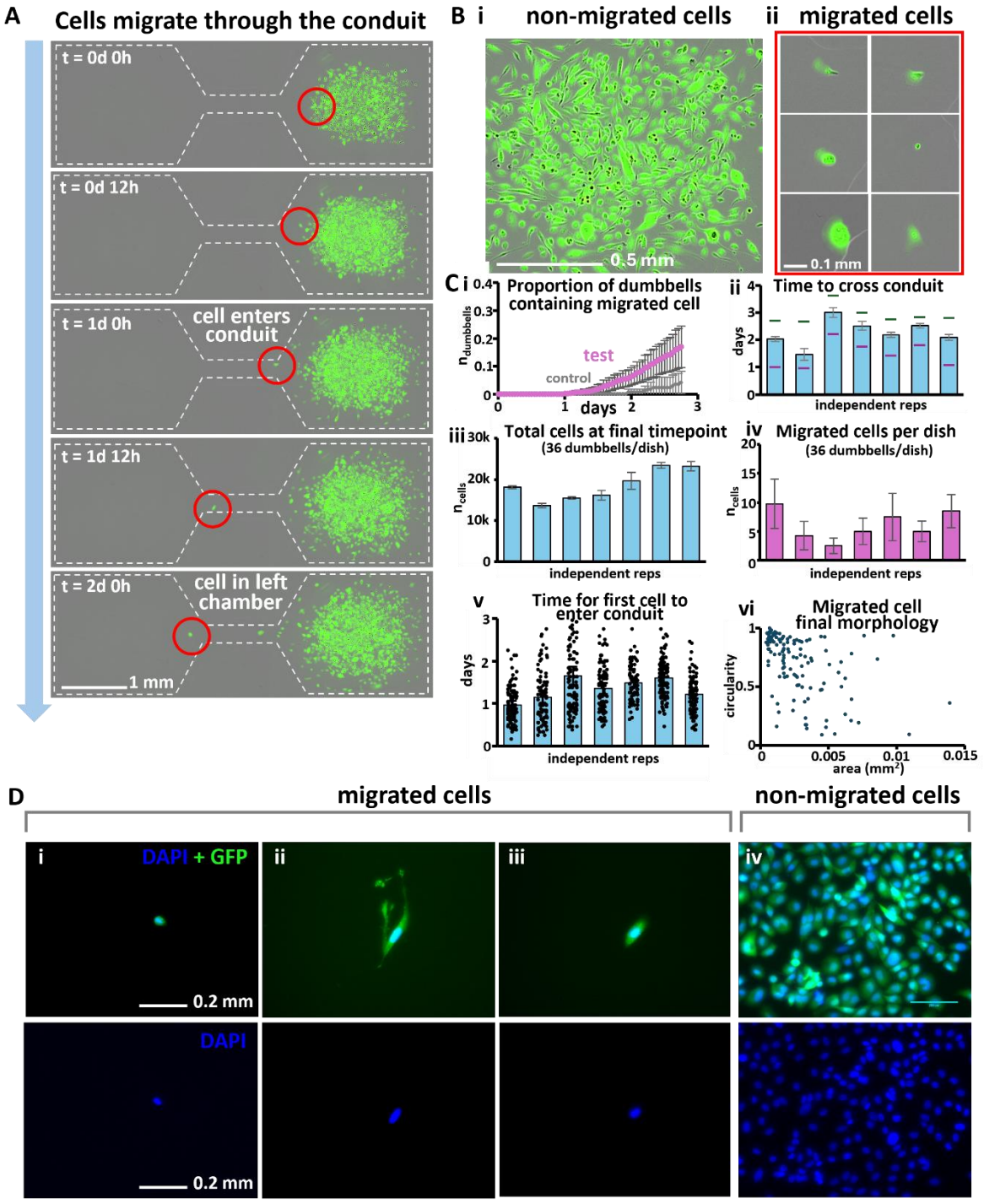

Figure 4. Single-cell migration through dumbbells. (A) PC3-eGFP cells are initially confined to the right chamber. Excellent circuit optics allows migration of single cells to be followed. **(B)** Representative

fluorescence images showing cell morphology in **(i)** the non-migrated cell population and **(ii)** migrated cells at the final timepoint. **(C)** Some key migration parameters across 7 replicates. **(i)** Proportion of dumbbells on a dish containing a migrated cell over time. There was enhanced migration in the test condition (serum) than the control (serum-free, $p < 0.01$ Welch's two-sided t-test comparing area under the curve). **(ii)** Times taken for a cell to traverse the conduit, with max/min time taken shown as green and purple lines respectively. **(iii)** Total number of cells across all 36 active dumbbells on a dish at the final timepoint. **(iv)** The average number of migrated cells on a dish for each replicate. **(v)** Average time taken for the first cell to enter the conduit. **(vi)** Morphologies of migrated cells at the final timepoint. Error bars in each sub-panel indicate standard errors of means (SEMs). **(D)** Nuclear staining. **(i-iii)** Representative migrated cells and **(iv)** non-migrated cells fixed and stained with DAPI. Merged GFP/DAPI images are shown with the corresponding DAPI-only images displayed below.

Reconfiguring dumbbells to isolate and pick cells of interest

A key advantage of fluid-walled microfluidics is the ability to dynamically reconfigure arrangements during an experiment [18] [21]. We applied this capability to demonstrate how the most migratory cells can be isolated from non-migrated ones. When a single migrated cell was identified in the left chamber, the same FC40 jet used for dumbbell fabrication was redeployed to construct new fluid walls across the conduit entrance and exit, thereby isolating each chamber. This required a higher velocity FC40 jet than used to initial form the dumbbell, to 'cut' through the conduit which has (at equilibrium) a cross-sectional area of ~ 170 μm^2. Consequently, the jet flow rate was increased from 480 µL/min to 900 µL/min to ensure sufficient FC40 could be jetted vertically through medium in the conduit onto the bottom of the dish to form the fluid wall. Following isolation of the specific cell from all the others, trypsin was used to detach the cell from the polystyrene surface, and, by withdrawing volume, the cell was picked and transferred to a microtiter well (**Figure 5A**). An additional step was required to obtain single non-migrated cells. Non-migrated cells were isolated, detached, and pooled, and the resulting cell suspension distributed across a GRID of fluid-walled micro-chambers [20] (**Figure 5B**). If a single cell was identified within a chamber, it was picked using an optimized method (supplementary **Figure S9** [p. 99]).

Proliferation of picked single migrated cells was assessed under three conditions: medium + 10% FBS, co-culture with LNCaP cells, and medium + 30% FBS. Co-culture with

LNCaP was included based on previous reports indicating enhanced viability under these conditions [37]. Cells grew to yield clones (**Figure 5C**), with an average cloning efficiency of 12% in the high-serum condition – lower than that achieved by other single-cell handling systems [38] and likely due to the relative difficulty in lifting cells from the fibronectin-coated polystyrene substrate, requiring trypsinisation for > 15 mins and often two consecutive rounds of picking. Quantification of fold-change in cell number at days 1, 7 and 14 revealed that proliferation was enhanced using 30% FBS (**Figure 5D**). The large error bars reflect both the relatively low cloning efficiency and the successful expansion of clonal colonies, with examples growing up to ~200 cells over 14 days. Picking efficiency was also evaluated (**Figure 5E**). Approximately half of migrated cells (3 replicates) were picked on the first attempt, and re-picking missed cells raised recoveries comparable to those found in our optimized GRID-based workflow (**Figure S9** [p. 99]).

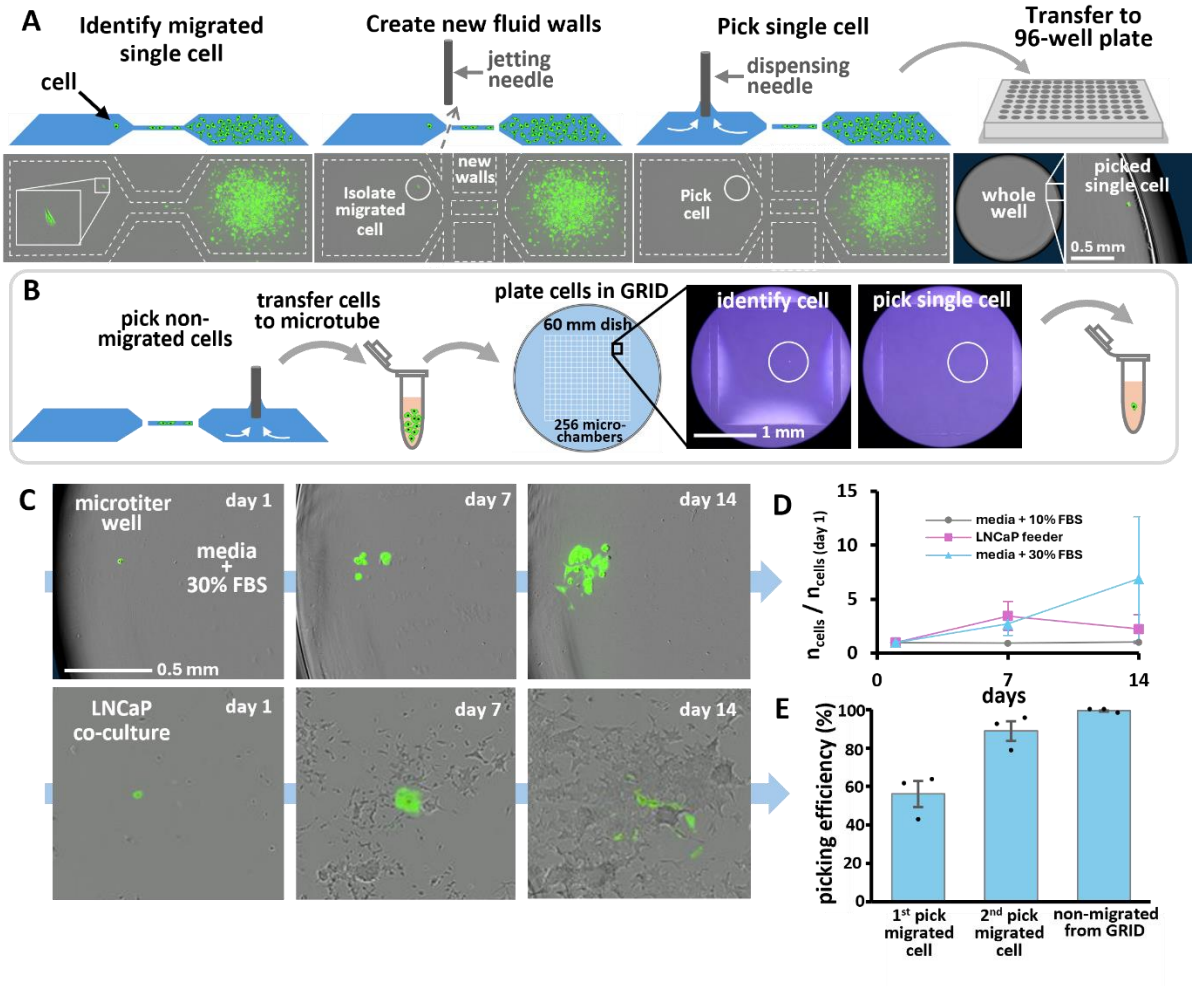

Figure 5. Reconfigure dumbbell to isolate and pick single cell of interest. (A) Workflow for isolation and picking of migrated cell (PC3-eGFP) from dumbbells. Fluorescence images of dumbbells shown below. First, a single migrated cell is identified. Then, a jet of FC40 is used to create new fluid walls across the conduit, isolating the cell from the non-migrated population. The cell is then picked from the chamber and transferred to a microtiter well. **(B)** Workflow for picking many non-migrated cells, followed by clonal isolation. Non-migrated cells are picked and collected in a microtube, then the suspension is plated across a GRID of fluid-walled chambers, single cells identified and picked for downstream analysis. **(C)** Single migrated cells are picked and transferred to microwells containing medium + 30% FBS, or LNCaP co-cultures. **(D)** Cell proliferation in different environments, quantified as fold increase in cell number at d 7 and d 14 relative to counts one day after picking (± SEM). **(E)** Comparison of single-cell picking efficiency. Cells picked by two sequential rounds of picking showed high efficiency, comparable to the optimized GRID-based method (± SEM).

AI segmentation and tracking of single cells

We exploit the excellent optics provided by the transparent fluid walls to train a custom model for automated segmentation and tracking of individual cells using Cellpose-SAM. Training on 100 manually-segmented images was sufficient to reach ~97% accuracy (**Figure**

S10 [p. 100]). Hourly live-cell imaging enabled high-resolution single-cell tracking and extraction of dynamic morphological features during migration (**Figure 6A, B**). Using this trained model in combination with ImageJ, cells were tracked across 58 representative dumbbells, each containing a single migratory cell (supplementary **Movie S4, S5**). If multiple cells migrated through the conduit, analysis was restricted to the trajectory of the first cell to complete transit. Analysis of cell trajectories using polar histograms (rose plots) revealed a clear directional bias of migrated cells towards and through the conduit (**Figure 6Ci**), whereas non-migrating ones showed no such bias (**Figure 6Cii**).

We next compared the total displacement of each tracked cell in 5 representative examples. In most cases, the cell that successfully migrated through the conduit also exhibited the greatest overall displacement within the circuit. However, we also observed instances where a cell displayed high motility within the chamber but did not traverse the conduit (**Figure 6D**).

Combining segmentation with tracking enabled assessment of morphological dynamics during migration. For example, analysis of cell area revealed that both migrated and non-migrated populations began with similar sizes (average initial migrated cell area of 0.0017 mm^2 and 0.0013 mm^2 for non-migrated), but migratory cells exhibited a greater increase in area over time compared with the average non-migrated cell (average migrated cell area of 0.0028 mm^2 and 0.0015 mm^2 for non-migrated at the final timepoint, with maximum average values of 0.0035 mm^2 and 0.0018 mm^2 for each group respectively, **Figure 6E**).

To relate morphology to migratory behaviour of 58 migratory cells, we compared average cell area, circularity, and velocity (**Figure 6Fi**). Visualisation of area against circularity revealed that migrated cells segregated into distinct morphological subpopulations. K-means clustering identified two groups: a population of smaller, more circular cells and a population of larger, less-circular ones (**Figure 6Fii**). The first group had an average cell area of 0.0023 mm^2 and circularity of 0.52, whereas the second had an average area of 0.0049 mm^2 and circularity of 0.44. Analysis of motility revealed that the smaller, circular cells migrated at higher

average velocities (0.053 mm/h) compared with the larger, less-circular counterparts (0.046 mm/h, **Figure 6Fiii**, supplementary **Movie S6**). [See supplementary **Figure S10** [p. 100] for further information on implementing Cellpose and ImageJ for automated segmentation and tracking of single cells].

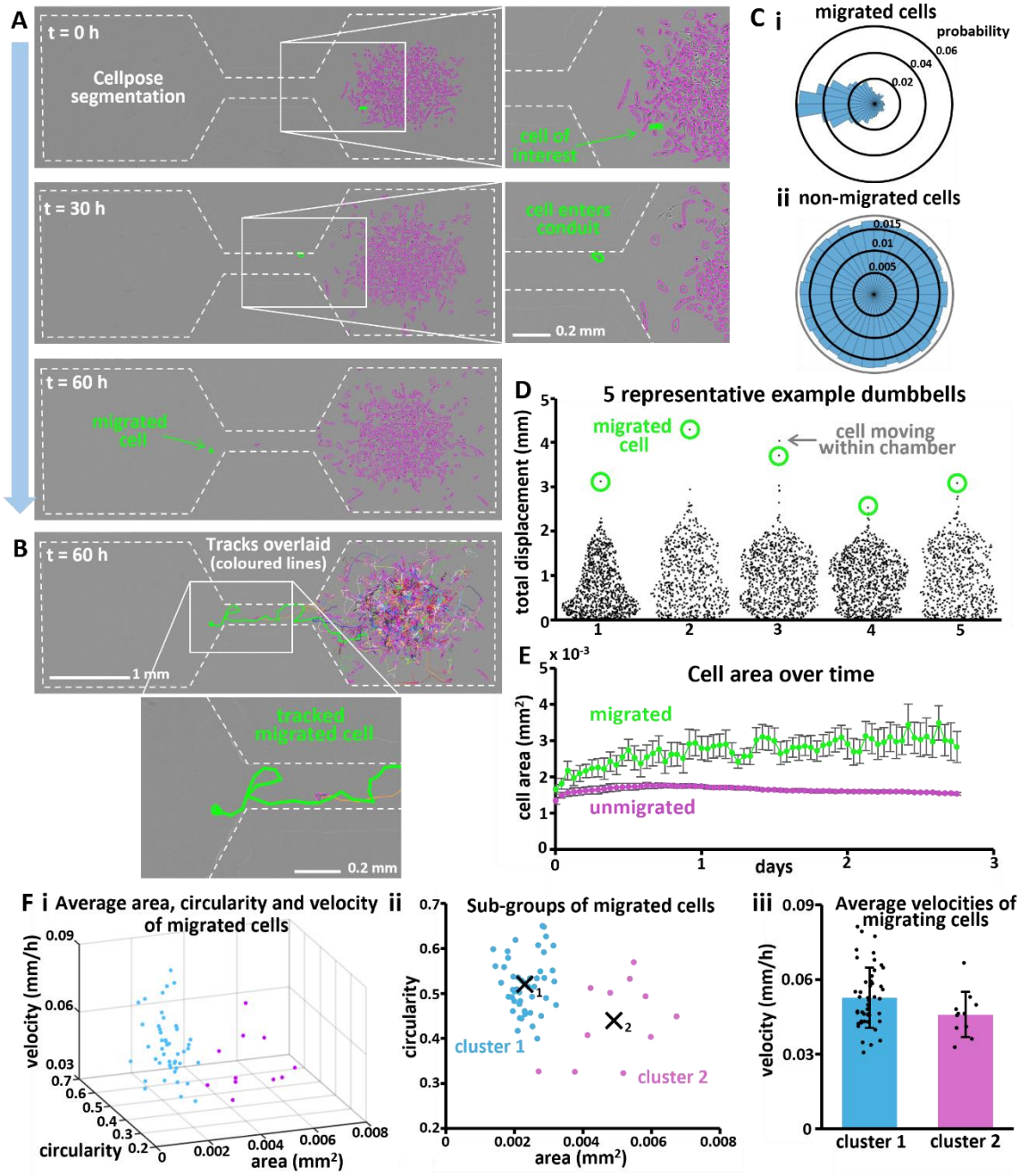

Figure 6. Segmentation and tracking of single cells. (A) A custom Cellpose-SAM model, trained on representative images of dumbbells, was used to segment individual cells within time-lapse stacks. Hourly imaging enabled high-resolution cell tracking. A green line is drawn around the cell of interest, and purple around all others. **(B)** Final frame from A with tracks overlaid. The migrated cell is highlighted

in green, with multicoloured lines showing tracks of non-migrated cells. **(C)** Migrated cells showed a strong bias towards the left, through the conduit **(i)**, whereas non-migrated cells had no directional preference **(ii). (D)** Comparison of track lengths revealed that migrated cells typically had the greatest total displacement; however, in some cases, highly-motile cells failed to traverse the conduit. Data from 5 representative dumbbells are shown. **(E)** Integration of segmentation with tracking allowed quantification of changes in cell area in migrated versus non-migrated populations over time (± SEM). **(F)** Comparison of **(i)** average area, circularity, and velocity (± SEM) among migrated cells. Cluster analysis based on **(ii)** cell morphology reveals distinct subpopulations, which results suggest may have **(iii)** different motility characteristics ($p = 0.054$, Welch's two-sample t-test).

Discussion

Prostate cancer metastasis remains a major clinical challenge. We present an accessible fluid-walled microfluidic platform for biologists to create high throughput migration assays on-demand.

Conventional microfluidic systems typically rely on lithography-based fabrication methods, which can require several hours to produce a single chip and often restricts access to cells confined within enclosed microchannels [39]. In contrast, jet-printing fluid walls enabled rapid and reproducible fabrication of microfluidic arrangements within seconds, with all regions remaining fully accessible (**Figure 1**), overcoming some of the fabrication barriers associated with conventional microfluidics [16].

Dumbbell stability requires protein adsorption to the media-FC40-polystyrene pinning line [33], and 0.5% FBS concentration allowed reliable fabrication (**Figure S1** [p. 82]). Modulating chamber volumes enabled control of flow direction (**Figure 2**) and spatial confinement of cells and chemo-attractant to distinct dumbbell chambers (**Figure 3; Figure S5** [p. 95]). Over 3 days, some cells migrated through the conduit towards serum (**Figure 4**). This is consistent with findings from conventional microfluidic migration assays, which have shown that within heterogenous cancer cell populations, only a subset of cells exhibit migratory behaviour through microchannels, while others remain non-migratory [11] [12]. Migratory cells were morphologically heterogeneous, ranging from small and round to larger cells with a less circular, more mesenchymal shape, with evidence of protrusions indicative of

lamellipodia forming in the direction of movement (**Figure 4B**). The presence of the latter is consistent with previous microfluidic migration studies, which have reported that highly chemotactic cells often display more elongated, mesenchymal morphologies compared to non-migratory cells [27] and may be indicative of an epithelial-mesenchymal transition (EMT [40]). However, further characterisation would be required to confirm this.

Only a small minority of cells migrated, with a dish containing 36 dumbbells yielding on average only 3 migratory cells; this is consistent with the small fraction of cells within a tumour being metastatic [41]. Green-fluorescent BSA served as a surrogate for FBS to monitor diffusion through the conduit (**Figure S7** [p.97]). Fluorescence was first detected at the conduit opening after ~2 hours, indicated the onset of diffusion. A stable gradient was estimated to form after a further ~3.5 hours and persist beyond the experiment duration (~9 days). However, signal intensity increased until ~12 hours post-infusion. This may indicate incomplete equilibration of dumbbell chambers, with residual flow partially opposing diffusion, or could reflect adsorption and accumulation of fluorescent albumin to the polystyrene surface [42].

Media + 20% FBS promoted migration (**Figure S7** [p. 97]), and smaller volumes limited proliferation, ensuring that cells in the conduit were migrating rather than expanding (**Figure S8** [p. 98]). Although serum was used as the chemoattractant in this work (as in previous studies [29] [43]), future work could explore alternative chemoattractants, such as epidermal growth factor [44] or bone-associated cytokines (e.g. TGF-β, BMP-2) [45] [46] to enhance the physiological relevance of the assay. Cells often explored the chamber before entering the conduit, however in some cases cells could be observed immediately moving towards and through the conduit (**Movie S1**). As some cells migrated in serum-free controls, serum enhances, rather than initiates, migration in an inherently exploratory subpopulation (**Figure 4Ci**).

Conduit height is dependent on chamber volume, with low volumes enabling very shallow conduits (e.g. ~1.3 μm at 150 nL, **Figure S3** [p. 93]), smaller than the height of adherent PC3 cells (~3 – 5 μm [36]). Comparable length scales are employed in many PDMS-based microfluidic migration assays, where channel heights ~3 – 5 μm are used to prevent cells in suspension from entering microchannels, or mimic aspects of the metastatic process where cells navigate through restricted microenvironments [11] [12] [13] [47] [48]. Even shallower conduits (< 1 μm) were reported in a previous study where conduits were confined by similar fluid interfaces (silicone oil-medium) and used to study neutrophil migration [14]. In these systems, interfacial deformation during cell transit imposed compressive forces that elicited bleb-based migratory behaviour, and more closely recapitulated migration through confined tissue environments than solid-walled systems. A similar interaction is likely in the present system, where interfacial deformation may impose mechanical constraints on migrating cells. Such confinement is likely to also influence processes associated with EMT and hence cell mobility [49]. Accordingly, future work could include analysis of EMT markers (e.g. upregulation of vimentin or downregulation of E-cadherin [50]) in migratory versus non-migratory cells to further elucidate these effects.

Cells were fixed within dumbbells and stained with DAPI to confirm the presence of nuclei (**Figure 4D**). Migrated and non-migrated cells were also evaluated for senescence-associated markers using β-galactosidase, however staining yielded insufficient signal for robust analysis, possibly due to insufficient volume of staining solution added to each dumbbell chamber (supplementary **Figure S11** [p. 101]).

Single migratory cells were isolated, picked, and yielded clones (**Figure 5**), however cloning efficiency was low compared to other automated single-cell handling systems – further optimisation is required to improve clonal recovery. The ability to isolate and retrieve individual cells represents a key advantage of fluid walls over conventional microfluidic platforms, where migratory or non-migratory cells are typically pooled for downstream analysis [11] [12] [13].

While such approaches enable comparisons between broad groups, they may overlook heterogeneity within migratory subpopulations. We also show a method for obtaining single non-migrated cells, demonstrating a comparative framework (**Figure 5B**). Beyond comparison between migratory subpopulations and/or non-migratory cells, future work would be to also evaluate non-transduced PC3 to determine whether transduction has influenced migratory behaviour.

The transparency of fluid walls allowed collection of images throughout the workflow, and use of automated segmentation and tracking routines allowed comparison of both the morphologies and motilities of migratory and non-migratory cells (**Figure 6**). While the Cellpose/ImageJ tracking worked well, it was computationally expensive, taking ~5 minutes per dumbbell on GPUs and ~40% of tracked migratory cells required manual correction. The migrating cells grew over time more rapidly than non-migrating ones (**Figure 6E**) likely due to entering a serum-rich environment. K-means clustering was used to identify two distinct migratory groups: smaller, rounder cells and larger, less circular cells (**Figure 6F**). Smaller cells on average migrated faster than the larger ones, likely due to differences in traction energy associated with attachment area [51]. The mechanical resistance imposed by the interface may also influence migration velocity since greater interfacial deformation may be required to accommodate larger cells. Similar trends have been reported in conventional microfluidic studies where the relative size of the cell to the microchannel influences migration dynamics: narrower channels require more pronounced deformation resulting in reduced migration velocities [52] [53]. It has also been shown that under confinement, cells can transition from slower mesenchymal modes to faster amoeboid migration phenotypes, leading to increased migration speeds in narrower channels [54] [55]. Further characterisation is required to determine whether a similar transition occurs in this system.

While smaller cells on average migrater faster than larger ones, the difference in mean velocities between the two groups was not statistically significant ($p = 0.054$, Welch's two-sample t-test), likely due to the limited sample size (47 cells in the first group and 11 in the

second). Increasing the number of tracked cells would improve statistical power and may enable more robust characterisation of subpopulations. Furthermore, we cannot directly infer that faster-moving cells possess greater metastatic potential as cells may adopt different migratory behaviours in more complex/3D environments. Nevertheless, prior studies have reported correlations between increased motility and metastatic fitness [12] [13] [56].

While our platform has many advantages, some limitation should be noted. Dumbbell conditions were optimised for PC3 cells, different cell types would require re-optimisation to ensure sufficient yields. Furthermore, diffusion gradients exist only within the conduit, making it challenging to infer precise chemotactic responses, although alternative fluid-walled designs exist for such applications [22] [57]. In summary, this work establishes fluid-walled microfluidics as an accessible platform for studying single migratory cancer cells, opening new avenues for dissecting the functional heterogeneity underlying metastasis.

Materials and methods

Cell culture

Cells were grown routinely at 37°C and 5% CO_2 and counted using a Bio-Rad TC10 automated cell counter unless stated otherwise.

Human prostate cancer (PC3, transduced with a lentiviral vector encoding for enhanced green fluorescent protein, eGFP, transduced cells provided by Dr. Yollanda Calle, King's College London) cells [24] and lymph node carcinoma of the prostate (LNCaP) cells [58] were cultured in 20 mL RPMI-1640 medium (Sigma-Aldrich) + 10% FBS (Gibco) + 1% MEM nonessential amino acids (Gibco) + 1% penicillin-streptomycin (Gibco) + 1% L-Glutamine (Gibco) + 1% sodium pyruvate (Gibco) + 1% MEM vitamin solution (Gibco) in 75 cm^2 U-shaped canted neck flasks (Corning). We refer to this media composition as 'complete' media (without FBS). Cells were passaged or prepared for experiments by first pre-warming media, PBS (Sigma-Aldrich) and trypsin (TrypLE Express, Gibco) in a 37°C water bath. Media was removed, cells rinsed (PBS, 3 mL) and detached (trypsin, 3 mL). Cells were incubated (3

mins), 4 mL media added, suspension transferred to 15 mL centrifuge tube (300g; 5 min) and supernatant removed. Cells were resuspended in 5 mL media, counted and diluted to the required concentration.

Human embryonic kidney (HEK 293) cells [59] were cultured in 5 mL DMEM (Sigma-Aldrich) + 10% FBS + 1% penicillin-streptomycin in 25 cm^2 polystyrene canted neck flasks (Corning). Cells were passaged or prepared for experiments as above with the following modifications: rinsed with 1 mL PBS, detached (trypsin, 1 mL), 4 mL media added then spun down (47 x g RCF; 3 min). Cells resuspended in PBS and using a haemocytometer.

Fluid printer

The fluid printer (iotaSciences Ltd) comprised a three-axis traverse and two integrated syringe pumps used to automate fluid deposition via two needles (one per syringe). The first syringe contained FC40 and connected to a needle (70 μm internal diameter) spatially controlled via the traverse to jet-print the microfluidic circuit; the 'jetting needle'. The second was filled with 70% ethanol solution (to maintain sterility) and connected to the 'dispensing needle' (255 μm internal diameter) used in the handling of media, cells and reagents. Needles were connected to respective syringe pumps via Teflon tubing. The central platform within the printer held a single 60 mm petri dish and up to eight 1.5 mL Eppendorf tubes. A custom platform was attached to the front of the printer to accommodate microtiter well plates, allowing automated transfer of cells from petri dishes.

Fabricating and preparing dumbbells with fluid walls

Dumbbells with fluid walls were jet-printed following the workflow outlined in the experimental section of this paper, creating arrays of 80 dumbbells (16 rows, 5 columns, for detailed geometry, see **Figure S3** [p. 93]). The jetting process swept aside the underlying media such that each dumbbell contained approximately 150 nL (estimated by comparing weights of empty dishes and those covered by a thin film of media). Then, 600 nL PBS was added to the left and right chambers of the inner 36 dumbbells (the field of view of the live-cell

imaging system) and 800 nL subsequently removed – thereby also withdrawing a small volume of FC40. This minimized variability in dumbbell volume post-jetting and washed away residual serum (effectiveness of wash shown in **Figure S4** [p. 94]). Dumbbell chambers were then filled with 100 nL human FNC coating mix (AthenaES) to encourage initial cell attachment.

Enabling spatial confinement of cells and chemoattractant

First, 400 nL complete serum-free media was added to the left chamber (500 nL total volume). Then, 100 nL suspension (~ 500 cells in serum-free complete media) added to the right chamber (200 nL total volume). Differences in chamber volumes ensured flow from the left chamber to the right and hence cell confinement (**Figure S5** [p. 95]). Dishes were incubated for ~ 3 h to allow cells to attach. Before adding chemo-attractant, 400 nL was removed from the right (cell) chamber and 600 nL removed from the left, such that flow was always in the direction of the cell chamber. Then, 200 nL complete serum-free media was added to the cell chamber, and 100 nL complete media + 20% FBS was added to the left. Cell suspensions were aspirated manually before collection by the dispensing system, mitigating sedimentation within the storage tube.

Live cell imaging during migration

Following addition of chemo-attractant, cells were imaged every hour for ~ 3 days using the Incucyte S3 live-cell analysis system (Sartorius), taking phase-contrast and fluorescence (green) scans of the 36 inner dumbbells. Dishes were positioned using a custom holder (iotaSciences) and were typically loaded four at a time. Image data were organised using MATLAB (2023a, MathWorks) and time-lapse sequences of cell migration (phase-contrast and fluorescence) were created using ImageJ. To correct for positional drift, each cropped stack was stabilised using the template-matching plugin in ImageJ. Cell images in **Figures 3-5** are combined phase and fluorescent**, Figure 6** is phase only.

Fixing and staining cells post-migration

Cells were fixed by first adding 400 nL PBS to both dumbbell chambers. Next, 600 nL was removed followed by the addition of 600 nL fixative solution – PBS containing 4% paraformaldehyde (ThermoFisher). Dishes were incubated for 15 mins at room temperature, protected from light. Fixative was then removed and each side washed by withdrawing 800 nL and adding 600 nL PBS, repeated twice. Fixed dishes were sealed with parafilm, wrapped in foil and stored at 4°C.

For nuclear staining, FC40 was manually removed and dishes were rinsed twice with 1 mL PBS. Cells were then stained with DAPI by adding 1 mL staining solution (1:1000 dilution of 1 mg/mL stock in PBS; Sigma-Aldrich) per dish and incubating for 5 mins at room temperature. The staining solution was removed and dishes were rinsed with 5 mL PBS, followed by the addition of a further 5 mL PBS. Dishes were sealed, wrapped and stored as before until imaging. Imaging was performed using an EVOS FL Auto microscope (ThermoFisher) and images were processed using ImageJ.

To evaluate senescence-associated markers, cells were stained using a β-galactosidase staining kit (9860S, Cell Signalling Technology). Cells were fixed as described above, 600 nL staining solutions was then added to each chamber, dishes were sealed with parafilm and incubated for 7 days at 37° C in a dry non-CO_2 incubator. Prior to imaging, dishes were also stained with DAPI as described above (protocol provided by Daniele Cotton).

Optimization of cell number, chamber volume, and chemoattractant concentration

To optimize seeding concentrations used, dumbbells were fabricated as usual, and each dish divided into 3 columns of 12 dumbbells. Cell suspension (100 nL) was seeded into the right chamber at ~125, 250, or 500 cells. For each condition, cells were scored if they entered the conduit or progressed over halfway. The highest concentration (~500 cells per dumbbell) yielded the most cells progressing over halfway through the conduit (**Figure S6** [p. 95]).

To assess the effect of serum concentration and chamber volume on migration, dumbbells were fabricated and seeded with ~500 in the right chamber. After cell attachment, medium containing varying FBS concentrations (0% – 100%, 20% increments) was added to the left chamber. Dumbbells were arranged in 6 groups of 6 per dish, with experiments performed across 4 dishes: 2 with equilibrated chamber volumes ~150 nL, and 2 ~450 nL. Dishes were imaged hourly using the Incucyte, and cells scored if they entered the conduit or progressed over halfway. Total cell number within a circuit was counted using ImageJ (**Figure S8** [p. 98]).

Automated cell segmentation and tracking

Hourly phase-contrast images acquired using the IncuCyte were compiled into time-lapse stacks using MATLAB/ImageJ and stabilized. Stacks were cropped to single dumbbells containing cells migrated through the conduit. From each stack, the 20^{th}, 30^{th} and 40^{th} frames were extracted as representative samples for model training. Training images were sequentially loaded into the Cellpose graphical user interface (GUI), where the Cellpose segment anything model (SAM) provided initial segmentations. Segmentation errors were corrected manually for a human-in-the-loop workflow. In total, 150 images were annotated and custom models trained on an NVIDIA Quadro RTX 400 GPU. Subsequently, full time-lapse stacks were processed in ImageJ using the TrackMate plugin with the Cellpose detector module. Cell trajectories were generated using the Linear Assignment Problem (LAP) tracker. For the primary cell of interest in each stack, any tracking errors were manually corrected. The results datasets (including X-Y coordinates, cell area, perimeter, and circularity at each timepoint) were exported for further analysis.

Picking single cells post-migration

After 3 days, dishes were removed from the incubator and transferred to the fluid printer. To isolate the most migratory cells from the non-migrated population, new fluid walls were jet-printed intersecting both ends of the conduit (‘cutting’), physically separating the two

populations. To ensure consistent cutting, a higher jet rate of 900 µL/min was used. Then, dishes were imaged to confirm successful isolation and identify suitable candidates for retrieval. For each target chamber, 400 nL PBS was added and 600 nL subsequently removed to minimize chamber volume. Cells were detached using 400 nL trypsin per chamber, 20 mins incubation. The entire chamber volume was withdrawn, and the retrieved cell transferred to a 96-well microtiter plate with wells pre-filled with 100 µL media. Chambers were re-imaged after picking to confirm the removal of the target cell. If the cell remained, an additional 200 nL trypsin was added and the picking process repeated.

The same procedure was then applied to the non-migrated cell population, with the following modifications. Non-migrated cells (from dumbbells containing a migrated one) were picked into the first row a 96-well plate, each well pre-filled with 100 µL media. The suspension was then pooled into a 1.5 mL tube. In parallel, a microfluidic GRID comprising 256 microfluidic chambers was created [20]. A 60 mm dish was coated with a thin layer of PBS + 5 mg/mL BSA, overlaid with 2 mL FC40, and the fluid printer used to jet-print the GRID. Chambers were pre-filled with 100 nL PBS. The pooled cell suspension was then dispensed into the GRID, 100 nL per chamber. Visual inspection via microscope was used to confirm the presence of a single cell in a chamber. Chambers containing a single cell were subsequently aspirated and the cell transferred to a microtiter well (pre-filled with medium).

Optimization of single cell picking from GRID chambers

Arrays of 256 square chambers were jet-printed in 60 mm tissue culture-treated polystyrene dishes (Corning). To quantify picking efficiency, ~ 100 cells were seeded into each chamber. Cells were counted before and after picking, and efficiency defined as percentage of cells removed. The underlying medium used in GRID fabrication was varied, including 0.05%, 0.5%, and 5% BSA in PBS (to test whether BSA, known to inhibit cell adhesion, improved picking [60]), as well as standard culture medium supplemented with 10% FBS.

To ensure cells remained centrally located within chambers, we tested different ratios of chamber pre-fill volume to suspension added. Chambers were pre-filled with 50 or 100 nL PBS, after which cell suspension was added (200 nL total chamber volume). Cells were imaged (Olympus CKX53) and positions measured relative to chamber centre using ImageJ. Optimization experiments were first performed with HEK and LNCaP cells before PC3. Increasing BSA concentration and pre-filling chambers with PBS improved picking efficiency, the optimized method required chamber fabrication with PBS + 5 mg/mL BSA, pre-filling with 100 nL PBS, and adding 100 nL cell suspension (**Figure S9** [p. 99]).

Visualising confinement and diffusion of chemoattractant

Dishes and dumbbells were prepared as usual. After the final wash step, 200 nL PBS was added to the chamber that would normally contain cells. Subsequently, 100 nL complete media + 10 mg/mL BSA was added to the opposing chamber. The BSA solution comprised a mixture of fluorescently labelled and unlabelled protein at a 1:10 ratio (BSA AlexaFluor 488 conjugate, Invitrogen; BSA Fraction V, Sigma-Aldrich), corresponding to an effective FBS concentration of 20%.

Dishes were imaged every 2 h for 2 d using the Incucyte (phase and GFP fluorescence images), and time-lapse images stacks created as before. Time required for fluorescent albumin to enter the conduit was determined by drawing a line profile across the junction between the chamber and conduit and a second line 100 µm into the conduit in ImageJ, and monitoring pixel intensity to detect GFP signal. Estimated diffusion rates were calculated in Excel (version 2404, Microsoft).

Visualising effect of PBS wash in dumbbells

To assess the efficiency of washing in removing residual serum, 60 mm dishes were coated with 1 mL complete media + 0.25 mg/mL fluorescent BSA. The coating solution was withdrawn and overlaid with 2 mL FC40. Dumbbells were then jetted as normal and dishes imaged using the Incucyte. For the central 36 dumbbells, 600 nL PBS was added to the central

and right columns (24 dumbbells) followed by the withdrawal of 800 nL to complete the first wash. Dishes were re-imaged, after which the right column (12 dumbbells) underwent an additional wash before imaging a final time. Fluorescent intensity within each dumbbell was quantified using ImageJ.

Estimation of circuit local volumes and flow rates

Dumbbells matching the geometry used in experimental assays were fabricated in large uni-well dishes (Nunc™, ThermoFisher) with flat walls, improving side-on imaging quality compared to curved walls of Petri dishes. Dishes were coated with 4 mL DMEM + 0.5 % FBS; medium was withdrawn to leave a thin film, and ~ 20 mL FC40 overlaid. Since the normal fluid printer cannot accommodate larger dishes, a custom three-axis traverse system (iotaSciences) was used. The jetting needle was connected to a syringe pump (kd Scientific) driving a 2 mL syringe (Hamilton) filled with FC40. A separate syringe pump (PhD Ultra, Harvard Apparatus) controlled a 50 µL syringe (Hamilton) connected to a dispensing needle. After jetting, 100 nL serum-free media was dispensed into each chamber, and the dish imaged from side-on (FTA1000 B Class, First Ten Angstroms). Next, 400 nL of media was added to the left chamber and 100 nL to the right, with images acquired every 5 mins for 6 hours. Chamber heights were determined using FTA32 software, with the dispensing needle external diameter (0.51 mm) as a scale reference. Chamber volumes and corresponding pressures were estimated from measured heights. Flow rate was estimated from curve fit of average height of the taller drop over time, using the fit to estimate volume and smooth the data (curve fit to the average height was $h(t) = 0.0119e^{-1.1041t} + 0.2346e^{-0.016t}$ where h is drop height in mm and t time in hours).

Statistical analysis

All calculations, including estimation of local pressures within dumbbells, 3D geometry, and diffusion rates, as well as statistical analyses such as k-means clustering of migrated cell

morphological data, were carried out using Excel or MATLAB. Data were standardized by z-score for clustering.

Acknowledgements

The authors thank iotaSciences (iota Sciences Ltd, Begbroke Science Park, Oxfordshire, OX5 1PF) for providing equipment, reagents and financial support toward the project. This research was funded by Rosetrees, the John Black Charitable Foundation, the Oxford-MRC Doctoral Training Partnership and the National Institute for Health Research (NIHR) Oxford Biomedical Research Centre (BRC). The views expressed are those of the author(s) and not necessarily those of the NHS, the NIHR or the Department of Health.

References

[1] S. K. Wong, N.-V. Mohamad, T. R. Giaze, K.-Y. Chin, N. Mohamed, and S. Ima-Nirwana, 'Prostate Cancer and Bone Metastases: The Underlying Mechanisms', *Int J Mol Sci*, vol. 20, no. 10, p. 2587, May 2019.

[2] L. Bubendorf *et al.*, 'Metastatic patterns of prostate cancer: An autopsy study of 1,589 patients', *Human Pathology*, vol. 31, no. 5, pp. 578–583, May 2000.

[3] S. Boyden, 'The chemotactic effects of mixtures of antibody and antigen on polymorphonuclear leucocytes', *Journal of Experimental Medicine*, vol. 115, no. 3, pp. 453–466, Mar. 1962.

[4] X. Wang, C. C. Decker, L. Zechner, S. Krstin, and M. Wink, 'In vitro wound healing of tumor cells: inhibition of cell migration by selected cytotoxic alkaloids', *BMC Pharmacology and Toxicology*, vol. 20, no. 1, p. 4, Jan. 2019.

[5] D. Zicha, G. A. Dunn, and A. F. Brown, 'A new direct-viewing chemotaxis chamber', *Journal of Cell Science*, vol. 99, no. 4, pp. 769–775, Aug. 1991.

[6] M. Aslan, E.-C. Hsu, S. Liu, and T. Stoyanova, 'Quantifying the invasion and migration ability of cancer cells with a 3D Matrigel drop invasion assay', *Biology Methods and Protocols*, vol. 6, no. 1, p. bpab014, Jan. 2021.

[7] P. Bouchalova and P. Bouchal, ‘Current methods for studying metastatic potential of tumor cells’, *Cancer Cell International*, vol. 22, no. 1, p. 394, Dec. 2022.

[8] C. R. Justus, N. Leffler, M. Ruiz-Echevarria, and L. V. Yang, ‘In vitro Cell Migration and Invasion Assays’, *J Vis Exp*, no. 88, p. 51046, June 2014.

[9] Z. Yang *et al.*, ‘High Throughput Confined Migration Microfluidic Device for Drug Screening’, *Small*, vol. 19, no. 16, p. 2207194, 2023.

[10] F. Sala, C. Ficorella, R. Osellame, J. A. Käs, and R. Martínez Vázquez, ‘Microfluidic Lab-on-a-Chip for Studies of Cell Migration under Spatial Confinement’, *Biosensors (Basel)*, vol. 12, no. 8, p. 604, Aug. 2022.

[11] S. Ding *et al.*, ‘Sorting and characterization of cancer cells with different migration phenotypes using a microfluidic platform’, *Sensors and Actuators B: Chemical*, vol. 440, p. 137875, Oct. 2025.

[12] Y.-C. Chen *et al.*, ‘Functional Isolation of Tumor-Initiating Cells using Microfluidic-Based Migration Identifies Phosphatidylserine Decarboxylase as a Key Regulator’, *Sci Rep*, vol. 8, no. 1, p. 244, Jan. 2018.

[13] C. L. Yankaskas *et al.*, ‘A microfluidic assay for the quantification of the metastatic propensity of breast cancer specimens’, *Nat Biomed Eng*, vol. 3, no. 6, pp. 452–465, Jun. 2019.

[14] J. H. Schrope *et al.*, ‘Confinement by Liquid-Liquid Interface Replicates In Vivo Neutrophil Deformations and Elicits Bleb-Based Migration’, *Advanced Science*, vol. 12, no. 21, p. 2414024, 2025.

[15] C. Li *et al.*, ‘Combining Top-Down and Bottom-Up: An Open Microfluidic Microtumor Model for Investigating Tumor Cell-ECM Interaction and Anti-Metastasis’, *Small*, vol. 21, no. 9, p. 2402499, Mar. 2025.

[16] E. Berthier, E. W. K. Young, and D. Beebe, ‘Engineers are from PDMS-land, Biologists are from Polystyrenia’, *Lab Chip*, vol. 12, no. 7, Art. no. 7, Mar. 2012.

[17] E. J. Walsh *et al.*, ‘Microfluidics with fluid walls’, *Nat Commun*, vol. 8, no. 1, p. 816, Oct. 2017.

[18] F. Nebuloni, Q. B. Do, P. R. Cook, E. J. Walsh, and R. Wade-Martins, 'A fluid-walled microfluidic platform for human neuron microcircuits and directed axotomy', *Lab on a Chip*, vol. 24, no. 13, pp. 3252–3264, 2024.

[19] A. Prastowo, P. R. Cook, and E. J. Walsh, 'Biocompatibility of Sessile Drops as Chambers for Cell Culture', in *2019 2nd International Conference on Bioinformatics, Biotechnology and Biomedical Engineering (BioMIC) - Bioinformatics and Biomedical Engineering*, pp. 1–5. Sept. 2019.

[20] C. Soitu *et al.*, 'Microfluidic chambers using fluid walls for cell biology', *PNAS*, vol. 115, no. 26, Art. no. 26, June 2018.

[21] C. Deroy *et al.*, 'Reconfigurable Microfluidic Circuits for Isolating and Retrieving Cells of Interest', *ACS Appl. Mater. Interfaces*, vol. 14, no. 22, Art. no. 22, June 2022.

[22] C. Deroy *et al.*, 'Assaying Macrophage Chemotaxis Using Fluid-Walled Microfluidics', *Advanced Materials Technologies*, vol. 7, no. 9, p. 2200279 July 2022.

[23] N. M. Oliveira *et al.*, 'Suicidal chemotaxis in bacteria', *Nat Commun*, vol. 13, no. 1, p. 7608, Dec. 2022.

[24] M. E. Kaighn, K. S. Narayan, Y. Ohnuki, J. F. Lechner, and L. W. Jones, 'Establishment and characterization of a human prostatic carcinoma cell line (PC-3)', *Invest Urol*, vol. 17, no. 1, pp. 16–23, July 1979.

[25] K. Oono *et al.*, 'Inhibition of PC3 human prostate cancer cell proliferation, invasion and migration by eicosapentaenoic acid and docosahexaenoic acid', *Mol Clin Oncol*, vol. 7, no. 2, pp. 217–220, Aug. 2017.

[26] I. V. Maly and W. A. Hofmann, 'Effect of Palmitic Acid on Exosome-Mediated Secretion and Invasive Motility in Prostate Cancer Cells', *Molecules*, vol. 25, no. 12, p. 2722, June 2020.

[27] Y.-C. Chen, S. G. Allen, P. N. Ingram, R. Buckanovich, S. D. Merajver, and E. Yoon, 'Single-cell Migration Chip for Chemotaxis-based Microfluidic Selection of Heterogeneous Cell Populations', *Sci Rep*, vol. 5, no. 1, p. 9980, May 2015.

[28] F. Nebuloni, J. Morgan, E. J. Walsh, and P. R. Cook, ‘A platform for modular assembly and feeding of micro-organoids on standard Petri dishes’, *Biol Open*, vol. 12, no. 5, p. bio059825, May 2023.

[29] S. Garcia-Garcia *et al.*, ‘HGK promotes metastatic dissemination in prostate cancer’, *Sci Rep*, vol. 11, no. 1, p. 12287, June 2021.

[30] S. Winfree, ‘User-Accessible Machine Learning Approaches for Cell Segmentation and Analysis in Tissue’, *Front Physiol*, vol. 13, p. 833333, Mar. 2022.

[31] M. Pachitariu, M. Rariden, and C. Stringer, ‘Cellpose-SAM: superhuman generalization for cellular segmentation’, May 01, 2025, *bioRxiv*.

[32] A. Kirillov *et al.*, ‘Segment Anything’, Apr. 05, 2023, *arXiv*: arXiv:2304.02643.

[33] C. Soitu, N. Stovall-Kurtz, C. Deroy, A. A. Castrejón-Pita, P. R. Cook, and E. J. Walsh, ‘Jet-Printing Microfluidic Devices on Demand’, *Advanced Science*, vol. 7, no. 23, Art. no. 23, 2020.

[34] C. Soitu, C. Deroy, A. A. Castrejón-Pita, P. R. Cook, and E. J. Walsh, ‘Using Fluid Walls for Single-Cell Cloning Provides Assurance in Monoclonality’, *SLAS TECHNOLOGY: Translating Life Sciences Innovation*, vol. 25, no. 3, Art. no. 3, June 2020.

[35] F. Nebuloni, P. R. Cook, and E. J. Walsh, ‘Flows in fluid-walled conduits driven by Laplace pressure’, *Journal of Fluid Mechanics*, vol. 969, p. A28, Aug. 2023.

[36] X. Tang *et al.*, ‘Effects of substrate stiffness on the viscoelasticity and migration of prostate cancer cells examined by atomic force microscopy’, *Beilstein J Nanotechnol*, vol. 13, pp. 560–569, Jun. 2022.

[37] Y. Zhang *et al.*, ‘Exosomes Promote the Transition of Androgen-Dependent Prostate Cancer Cells into Androgen-Independent Manner Through Up-Regulating the Heme Oxygenase-1’, *International Journal of Nanomedicine*, vol. 16, pp. 315–327, Jan. 2021.

[38] J. A. E. Morgan, P. R. Cook, A. A. Castrejón-Pita, and E. J. Walsh, ‘Generation of Clonal Cultures of Adherent or Suspension Cells Using Flat Sessile Drops for Assurance of Monoclonality’, *Biotechnology and Bioengineering*, vol. 122, no. 10, pp. 2739–2750, Oct. 2025.

[39] F. Sala, C. Ficorella, R. Osellame, J. A. Käs, and R. Martínez Vázquez, 'Microfluidic Lab-on-a-Chip for Studies of Cell Migration under Spatial Confinement', *Biosensors (Basel)*, vol. 12, no. 8, p. 604, Aug. 2022.

[40] R. Kalluri and R. A. Weinberg, 'The basics of epithelial-mesenchymal transition', *J Clin Invest*, vol. 119, no. 6, pp. 1420–1428, Jun. 2009.

[41] N. Riggi, M. Aguet, and I. Stamenkovic, 'Cancer Metastasis: A Reappraisal of Its Underlying Mechanisms and Their Relevance to Treatment', *Annual Review of Pathology: Mechanisms of Disease*, vol. 13, no. Volume 13, 2018, pp. 117–140, Jan. 2018.

[42] M. M. Browne, G. V. Lubarsky, M. R. Davidson, and R. H. Bradley, 'Protein adsorption onto polystyrene surfaces studied by XPS and AFM', *Surface Science*, vol. 553, no. 1, pp. 155–167, Mar. 2004.

[43] Z. Wang *et al.*, 'RILP inhibits proliferation, migration, and invasion of PC3 prostate cancer cells', *Acta Histochemica*, vol. 124, no. 7, p. 151938, Oct. 2022.

[44] S. M. N. Rao, U. Tata, V. K. Lin, and J.-C. Chiao, 'The Migration of Cancer Cells in Gradually Varying Chemical Gradients and Mechanical Constraints', *Micromachines*, vol. 5, no. 1, pp. 13–26, Mar. 2014.

[45] L. Walker, A. C. Millena, N. Strong, and S. A. Khan, 'Expression of TGFβ3 and its effects on migratory and invasive behavior of prostate cancer cells: involvement of PI3-kinase/AKT signaling pathway', *Clin Exp Metastasis*, vol. 30, no. 1, pp. 13–23, Jan. 2013.

[46] H. Kwon *et al.*, 'Development of an in vitro model to study the impact of BMP-2 on metastasis to bone', *Journal of Tissue Engineering and Regenerative Medicine*, vol. 4, no. 8, pp. 590–599, 2010.

[47] C. D. Paul, P. Mistriotis, and K. Konstantopoulos, 'Cancer cell motility: lessons from migration in confined spaces', *Nat Rev Cancer*, vol. 17, no. 2, pp. 131–140, Feb. 2017.

[48] M. Mak, C. A. Reinhart-King, and D. Erickson, 'Elucidating mechanical transition effects of invading cancer cells with a subnucleus-scaled microfluidic serial dimensional modulation device', *Lab Chip*, vol. 13, no. 3, pp. 340–348, Feb. 2013.

[49] T. Zulueta-Coarasa, J. Fadul, M. Ahmed, and J. Rosenblatt, ‘Physical confinement promotes mesenchymal trans-differentiation of invading transformed cells in vivo’, *iScience*, vol. 25, no. 11, Nov. 2022.

[50] U.-G. Lo, C.-F. Lee, M.-S. Lee, and J.-T. Hsieh, ‘The Role and Mechanism of Epithelial-to-Mesenchymal Transition in Prostate Cancer Progression’, *Int J Mol Sci*, vol. 18, no. 10, p. 2079, Sep. 2017.

[51] A. Leal-Egaña *et al.*, ‘The size-speed-force relationship governs migratory cell response to tumorigenic factors’, *Mol Biol Cell*, vol. 28, no. 12, pp. 1612–1621, June 2017.

[52] Y. Belotti, D. McGloin, and C. J. Weijer, ‘Effects of spatial confinement on migratory properties of Dictyostelium discoideum cells’, *Commun Integr Biol*, vol. 14, no. 1, pp. 5–14. Jan. 2021.

[53] D. Irimia and M. Toner, ‘Spontaneous migration of cancer cells under conditions of mechanical confinement’, *Integr Biol (Camb)*, vol. 1, no. 0, pp. 506–512, Sep. 2009.

[54] A. W. Holle *et al.*, ‘Cancer Cells Invade Confined Microchannels via a Self-Directed Mesenchymal-to-Amoeboid Transition’, *Nano Lett.*, vol. 19, no. 4, pp. 2280–2290, Apr. 2019.

[55] Y.-J. Liu *et al.*, ‘Confinement and Low Adhesion Induce Fast Amoeboid Migration of Slow Mesenchymal Cells’, *Cell*, vol. 160, no. 4, pp. 659–672, Feb. 2015.

[56] N. Desjardins-Lecavalier *et al.*, ‘Migration speed of captured breast cancer subpopulations correlates with metastatic fitness’, *J Cell Sci*, vol. 136, no. 13, p. jcs260835, July 2023.

[57] F. Nebuloni, C. Deroy, P. R. Cook, and E. J. Walsh, ‘Stable diffusion gradients in microfluidic conduits bounded by fluid walls’, *Microsyst Nanoeng*, vol. 10, no. 1, p. 79, June 2024.

[58] J. S. Horoszewicz *et al.*, ‘LNCaP model of human prostatic carcinoma’, *Cancer Res*, vol. 43, no. 4, pp. 1809–1818, Apr. 1983.

[59] F. L. Graham, J. Smiley, W. C. Russell, and R. Nairn, ‘Characteristics of a human cell line transformed by DNA from human adenovirus type 5’, *J Gen Virol*, vol. 36, no. 1, pp. 59–74, July 1977.

[60] F. Grinnell and M. K. Feld, ‘Initial adhesion of human fibroblasts in serum-free medium: Possible role of secreted fibronectin’, *Cell*, vol. 17, no. 1, pp. 117–129, May 1979.

[61] G. L. Francis, 'Albumin and mammalian cell culture: implications for biotechnology applications', *Cytotechnology*, vol. 62, no. 1, pp. 1–16, Jan 2010.

[62] A. K. Gaigalas, J. B. Hubbard, M. McCurley, and S. Woo, 'Diffusion of bovine serum albumin in aqueous solutions', *J. Phys. Chem*., vol. 96, no.5, pp. 2355–2359, Mar. 1992.

Supplementary Information

Fluid printer

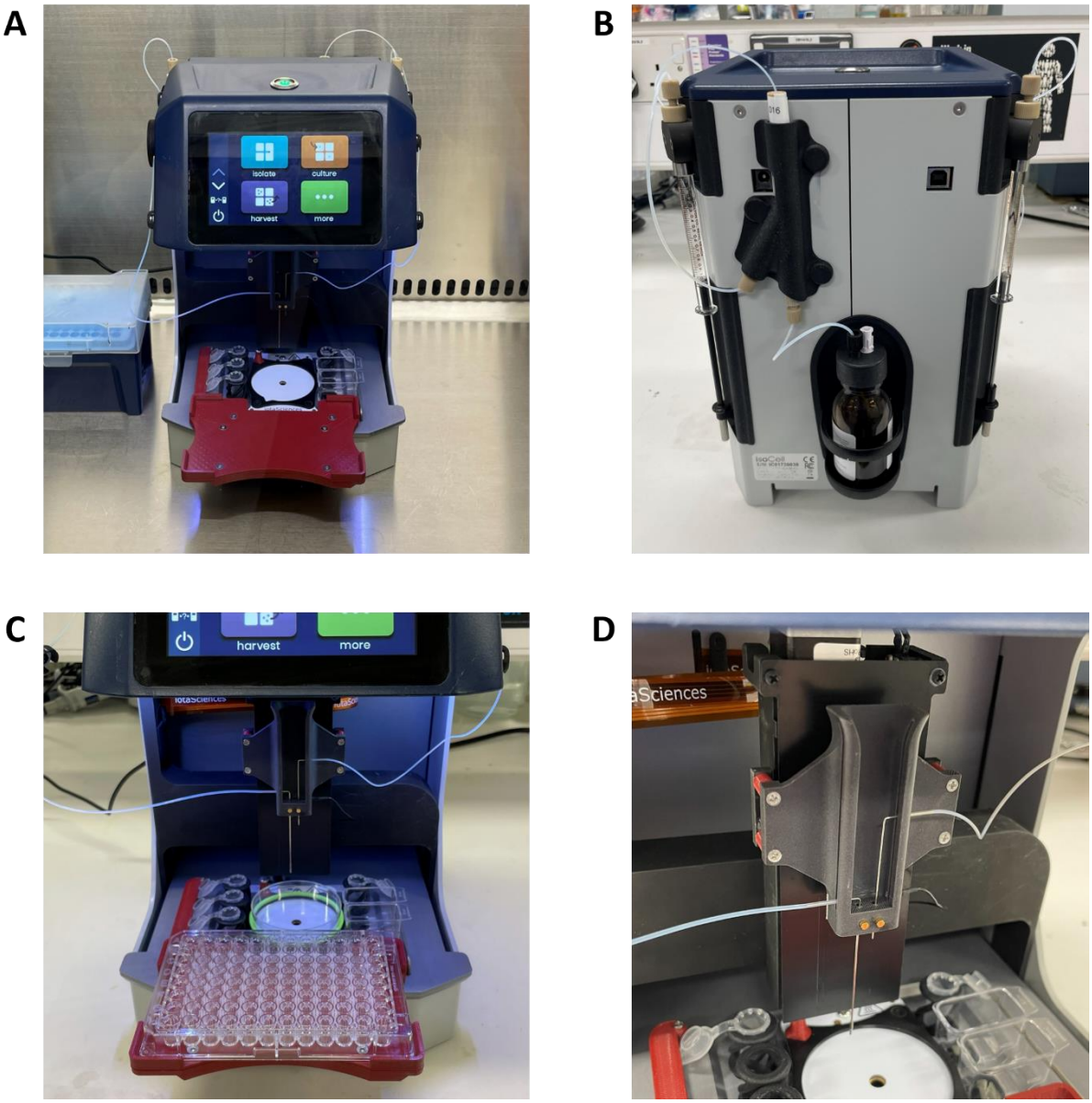

Figure S1. Fluid printer. Example images of the fluid printer used for fluid handling and fabrication of fluid walls. **(A)** Image of the printer in a laminar flow hood. The printer has been modified to accommodate well plates (red platform). **(B)** Image of printer rear. Bottle contains FC40 used to fabricate fluid walls. Left syringe contains FC40 for jetting, right syringe contains ethanol to maintain sterility within fluid handling system. **(C)** A 6 cm petri dish is loaded into the centre of the printer with microtube holders on each side (reservoirs for ethanol and waste on right). A 96-well plate is held in the custom attachment. **(D)** The jetting and dispensing needle are held within a housing unit and spatial control provided via the 3-axis traverse. Here the dispensing needle is in the lowered position. Images B-D were taken outside of the hood. All images were taken using a smartphone camera.

Serum content required for dumbbell fabrication

BSA is an excellent stabilizer of fluid walls, and RPMI medium plus FBS (which contains BSA) is used as a chemo-attractant. Consequently, FBS-free medium is applied as the control, and it is then important that this contains too little FBS to act as an attractant. Therefore, when jetting, we employed RPMI medium plus the lowest FBS concentration sufficient to stabilize footprints during subsequent volume additions (e.g., during 'washing').

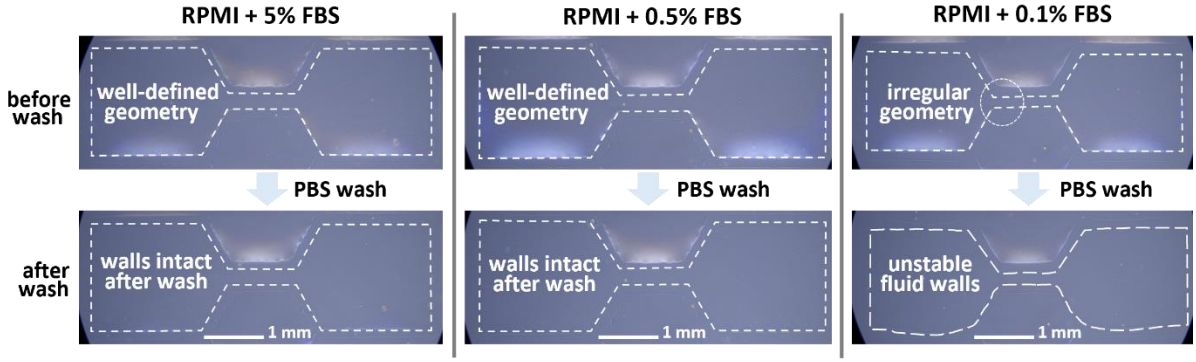

Figure S2. Serum content required for dumbbell fabrication. Dashed white lines mark dumbbell fluid walls. Walls are formed correctly after jetting through RPMI plus three dilutions of FBS (top). After washing each chamber with 600 nL PBS, fluid walls made with RPMI + 0.1% FBS, prove to be unstable (see curved pinning lines at bottom right and notably narrower conduit at top right, highlighted with circle).

Fluid-walled microfluidic dumbbells: pressure dynamics, 2- and 3-D geometries

Fluid-walled dumbbells are bounded by liquid-liquid interfaces. While their 2-D geometry is stable, 3-D geometry morphs when volumes are added or subtracted. Our dumbbell chambers are sufficiently small that interfacial forces dominate and govern their 3-D curvature. To estimate the radius of curvature of chambers, we approximate the Laplace pressure by equating it to that of a circular droplet with an equivalent footprint area. The equivalent footprint radius a_{eq} is defined as:

$$a_{eq} = \sqrt{\frac{chamber\ area}{\pi}} \tag{S1}$$

This approximation allows use of spherical-cap geometry in relating chamber height to volume V:

$$V = \frac{1}{6}\pi h\left(3a_{eq}^2 + h^2\right) \tag{S2}$$

and Laplace pressure:

$$P_L = \frac{2\gamma}{R} = \frac{4\gamma h}{h^2 + a_{eq}^2} \tag{S3}$$

Total pressure in the chamber is then given by summing Laplace and hydrostatic effects due to media and FC40:

$$P = \frac{4\gamma h}{h^2 + a_{eq}^2} + \rho_{media} g h + \rho_{FC40} g h_{FC40} \tag{S4}$$

The height of FC40 is calculated using a dish surface area of 21.5 cm^2 and 3 mL overlay. At equilibrium, the Laplace pressure in the chamber is equal to the pressure in the conduit where $P_{conduit} = \gamma / R_{conduit}$. Furthermore, we assume the height of the conduit to be much less than the height of the drop or conduit width ($h_c \ll a$ and $h_c \ll h$). This gives the relationship between chamber and conduit height:

$$h_c = \frac{2a_c^2 h}{h^2 + a_{eq}^2} - \frac{\Delta\rho g h a_c^2}{2\gamma} \tag{S5}$$

This can be used to calculate the cross-sectional area of the conduit, A_c:

$$A_c = \frac{(a_c^2 + h_c^2)^2}{4h_c^2}\cos^{-1}\left(\frac{a_c^2 - h_c^2}{a_c^2 + h_c^2}\right) - \frac{a_c}{2h_c}(a_c^2 - h_c^2) \tag{S6}$$

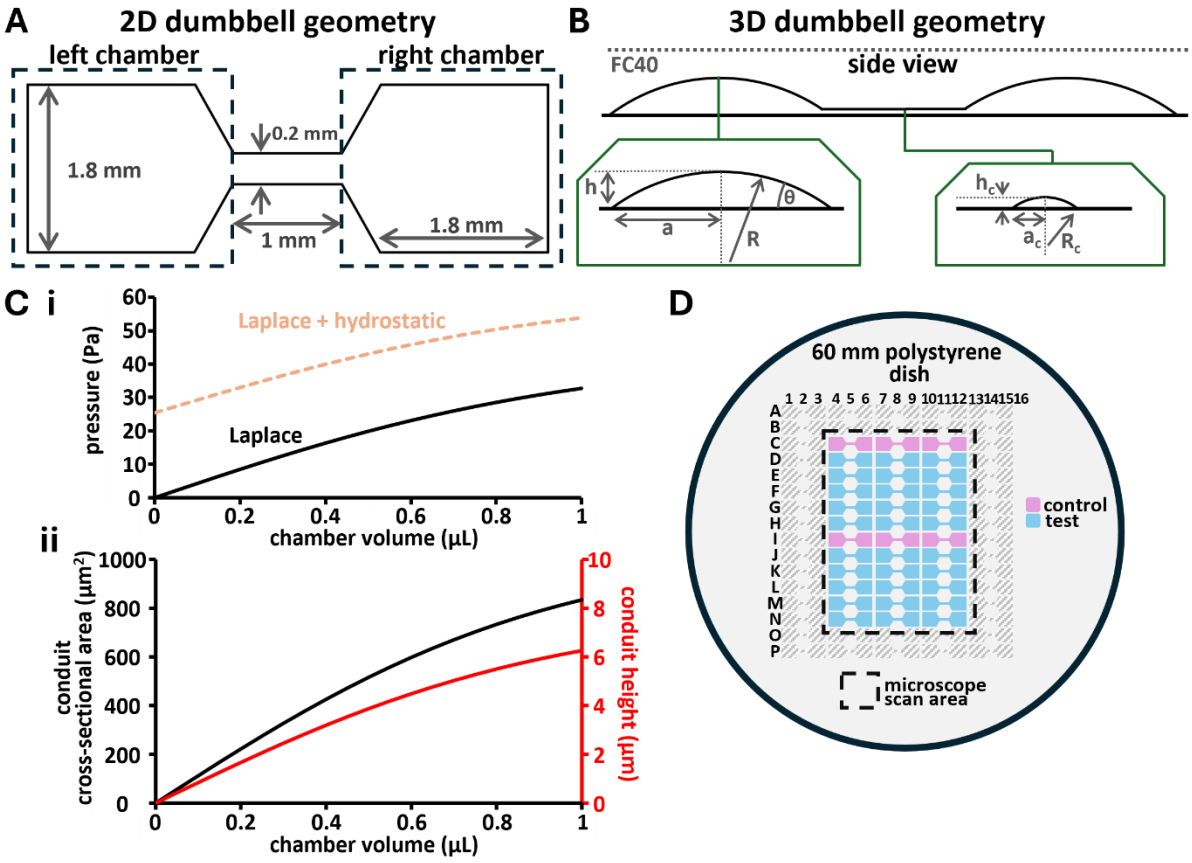

Figure S3. Dumbbell geometry, pressures, and arrays. (A) Single dumbbell with two chambers (1.8 mm x 1.8 mm) connected by a conduit (0.2 mm x 1 mm). **(B)** Side view of a dumbbell with equal volume in chambers. **(C)** Effect of increasing chamber volume on **(i)** chamber pressure, and **(ii)** conduit height and cross-sectional area. **(D)** Array of dumbbells on a 60 mm polystyrene dish. The central 36 dumbbells are within the area scanned by the Incucyte system (test dumbbells + 20% FBS are shown blue, and no-FBS controls pink).

Evaluation of PBS washes for removal of residual FBS

In addition to minimising FBS concentration used in the initial fabrication of fluid walls, dumbbells were rinsed with PBS to further minimise any effect of any residual FBS on chemo-attractant concentration and hence migration. Dumbbells were made using RPMI + green-fluorescent BSA, at the equivalent concentration to 0.5% FBS (0.25 mg/mL BSA) and changes in fluorescent intensity used to assess wash efficiency (**Figure S4**). After collecting fluorescent images at low power, conduits connecting chambers are scarcely visible at this magnification, but green fluorescence is clearly visible in both dumbbells and the hexagonal spaces between conduits. A single PBS wash applied to dumbbells (but not hexagonal spaces) removed

residual FBS from dumbbells (but not spaces); subsequent washes had minimal effect on dumbbell fluorescence.

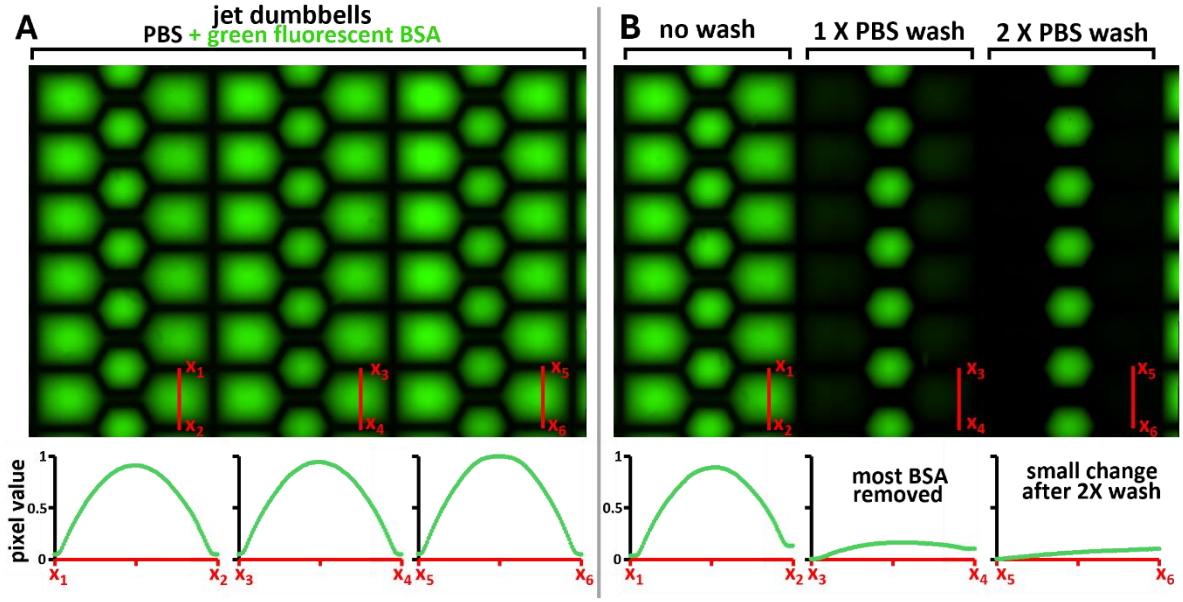

Figure S4. Evaluation of PBS washes for removal of residual FBS. (A) Dumbbells were made by first wetting a 60 mm dish with PBS + green-fluorescent BSA, withdrawing to leave a thin film, overlaying with FC40, and jet-printing dumbbells. Pixel intensities were measured across each chamber, averaged for left and right chambers across six dumbbells per column, and normalized to the maximum value. Intensity profiles are aligned to their corresponding column. **(B)** The middle column was washed once with 600 nL PBS per chamber, and the right washed twice. A single PBS wash removed most of the fluorescent signal, with the second providing only minor additional reduction.

Visualisation of flow between chambers

Flow between chambers was quantified through side-on imaging. Chamber heights were measured and volume estimated using spherical cap geometry, approximating each chamber as a round droplet with an equivalent footprint area. The flow rate was defined as the rate of change in volume, $Q = -dV/dt$, of the higher-volume chamber. To reduce noise, flow rate was calculated from chamber height after fitting a two-term exponential function in MATLAB to the temporal height profile of the larger chamber. Continuous flow was maintained during cell plating thereby confining cells to their respective chambers throughout the attachment phase.

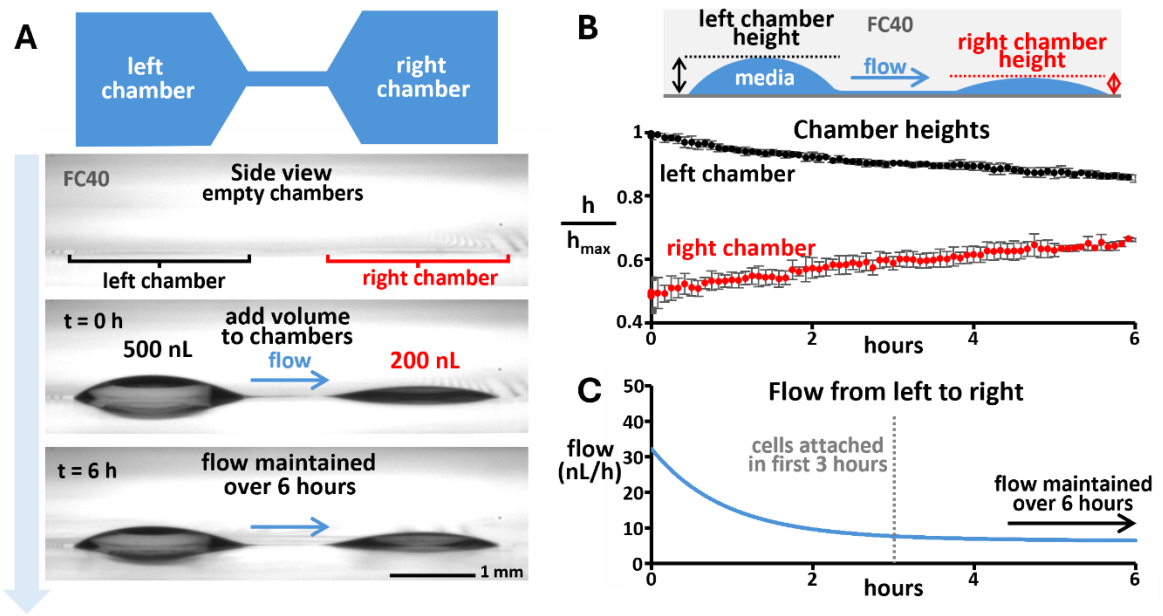

Figure S5. Visualization of flow between chambers. (A) Side-view imaging of a dumbbell follow withdrawal of residual media to leave empty chamber. Media volumes of 200 nL (right)and 500 nL (left) were added, establishing a pressure gradient driving flow from left to right. **(B)** Chamber heights were measured over time (± standard deviation) **(C)** Approximating chambers as spherical caps enables flow-rate estimation. Flow during seeding confined suspended cells within chambers, with attachment occurring after ~3 h.

Optimisation of cell seeding within dumbbells

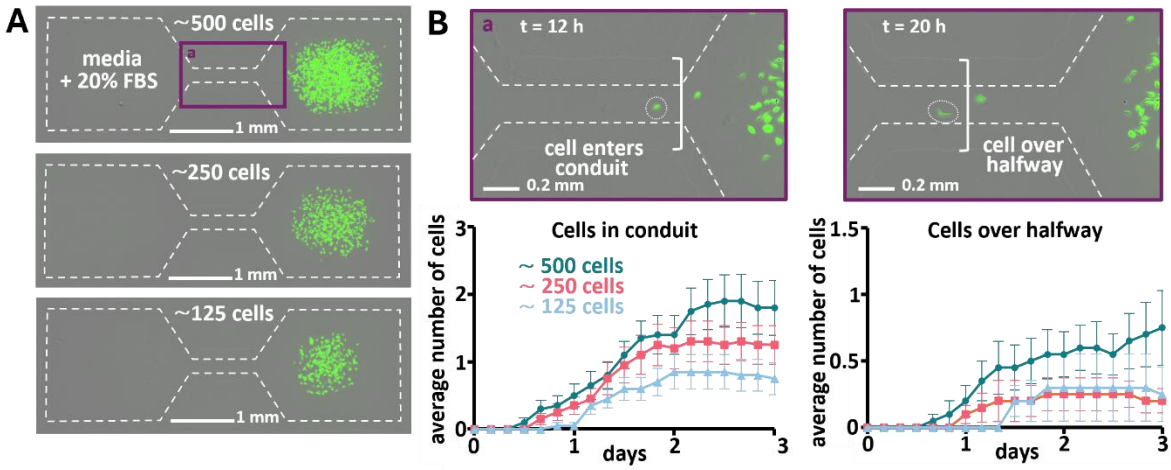

Figure S6. Optimization of cell seeding within dumbbells. (A) Cells were seeded into the right chamber at approximately 500, 250 and 125 cells per dumbbell. Media + 20% FBS was added to the left chamber. **(B)** Zoomed image of purple boxed region in A at two timepoints. The number of cells to enter the conduit and the number of cells over halfway into it for each condition (± SEM).

Diffusive transport of FBS within dumbbells

Determination of diffusion rates through microenvironments is essential in interpreting cellular response to chemical gradients. At equilibrium (no flow; equal chamber volumes), FBS diffuses from the left to the right chamber. The concentration profile along the conduit $c(x,t)$ was approximated using the one-dimensional diffusion equation derived from Fick's 2nd law for a semi-infinite medium and constant boundary concentration [1].

$$c(x,t) = C_o erfc\left(\frac{x}{2\sqrt{D}t}\right) \quad \text{(S7)}$$

where C_0 is the starting concentration in the left chamber, D is the diffusivity, x the distance along the conduit, t time, and $erfc$ the complementary error function. Given that albumin is the principal component of FBS [61] we use green-fluorescent BSA as both a surrogate and a visual aid to confirm initial confinement to the left chamber. The diffusivity is approximated as that of albumin in water (61 μm^2/s [62]).

The time taken to reach steady state, t_s, was estimated as the time required for the concentration at the distal end of the conduit to reach 40% of the left chamber concentration – representing <5% difference between the concentration profile and linear approximation:

$$t_s = \frac{1}{D}\left(\frac{l}{2erfc^{-1}(0.4)}\right)^2 \quad \text{(S8)}$$

At steady state, the gradient is considered linear and stable for a time t_{linear}, defined as the time required for the right chamber to reach 5% of the left chamber concentration. Considering molecular transfer from the left to the right chamber:

$$t_{linear} = 1.05\frac{lm_{transfer}}{DA_cC_0} \quad \text{(S9)}$$

where l is conduit length and $m_{transfer}$ the mass of molecules transferred from the left chamber to the right ($m_{transfer}$ = 1 μg, A_c = 170 μm^2).

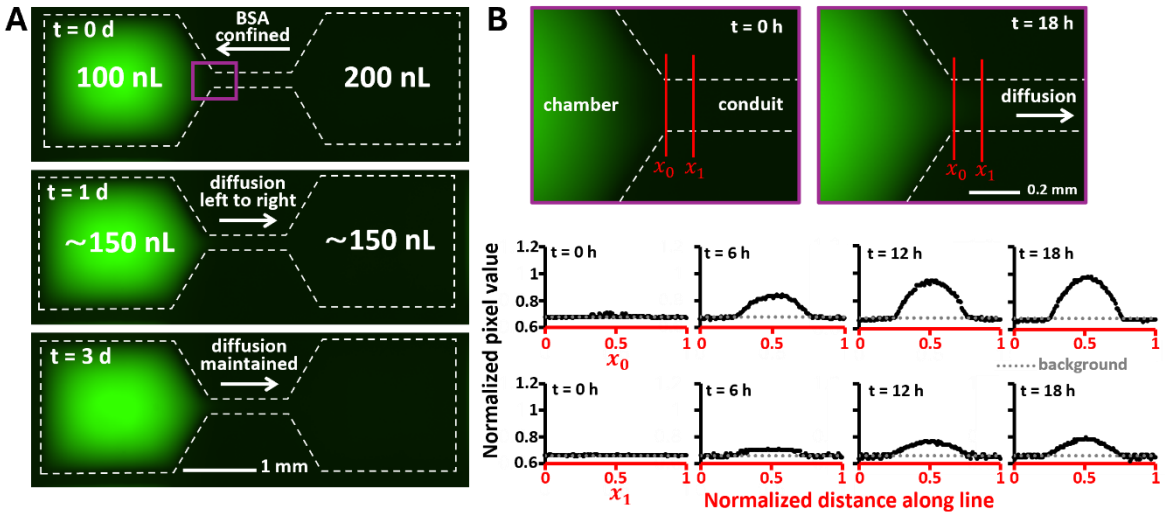

C

Conduit length	1 mm
Conduit cross sectional area at equilibrium	170 μm^2
Serum concentration in left chamber at equilibrium	13.33%
Diffusivity	61 μm^2/s
Time BSA first detected at conduit start	~ 2 h
Time to establish stable diffusion gradient	~ 3.5 h
Duration of stable diffusion gradient	~ 9 d

Figure S7. Visualizing diffusion through dumbbells. (A) Green-fluorescent BSA is used as a surrogate for FBS. Backflow driven by the gradient due to differences in Laplace pressures confines BSA initially to the left chamber. Chamber volumes equilibrate and BSA diffuses from left to right through the conduit. **(B)** Zoomed image of purple boxed region shown in A. Pixel intensity measured across the conduit opening x_0 (first row, 6 h intervals) and at 100 μm (second row, same timepoints) into the conduit, x_1, confirms diffusion of fluorescent BSA. Data is averaged across three reps, normalized to maximum pixel value and background-corrected using average pixel value along first 0.15 mm of line, outside of conduit **(C)** Summary of measured and calculated parameters. Diffusion is sustained for more than 3 d.

Impact of chamber volume and serum concentration on cell migration and proliferation

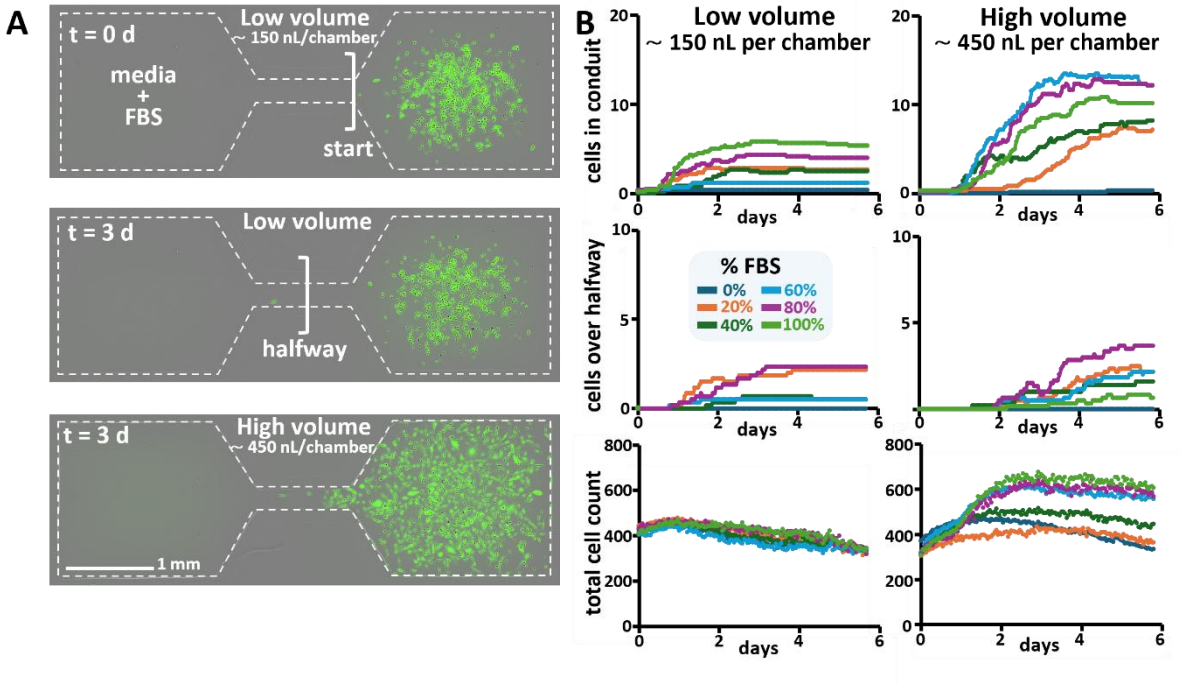

Figure S8. Impact of chamber volume and serum concentration on cell migration and proliferation. (A) Approximately 500 cells were seeded into the right chamber, with media containing varying concentrations of FBS added to the left chamber. In the *low-volume* condition, chamber volume at equilibrium was ~150 nL, and in *high-volume* there was ~450 nL per chamber. **(B)** Cells migrating into the conduit were counted at the entrance and at the halfway point for each serum concentration. Total cell numbers (cells within the conduit and chambers) were quantified to assess the effect of serum content and chamber volume on proliferation. Each line represents the average of 6 dumbbells.

Cell picking optimisation

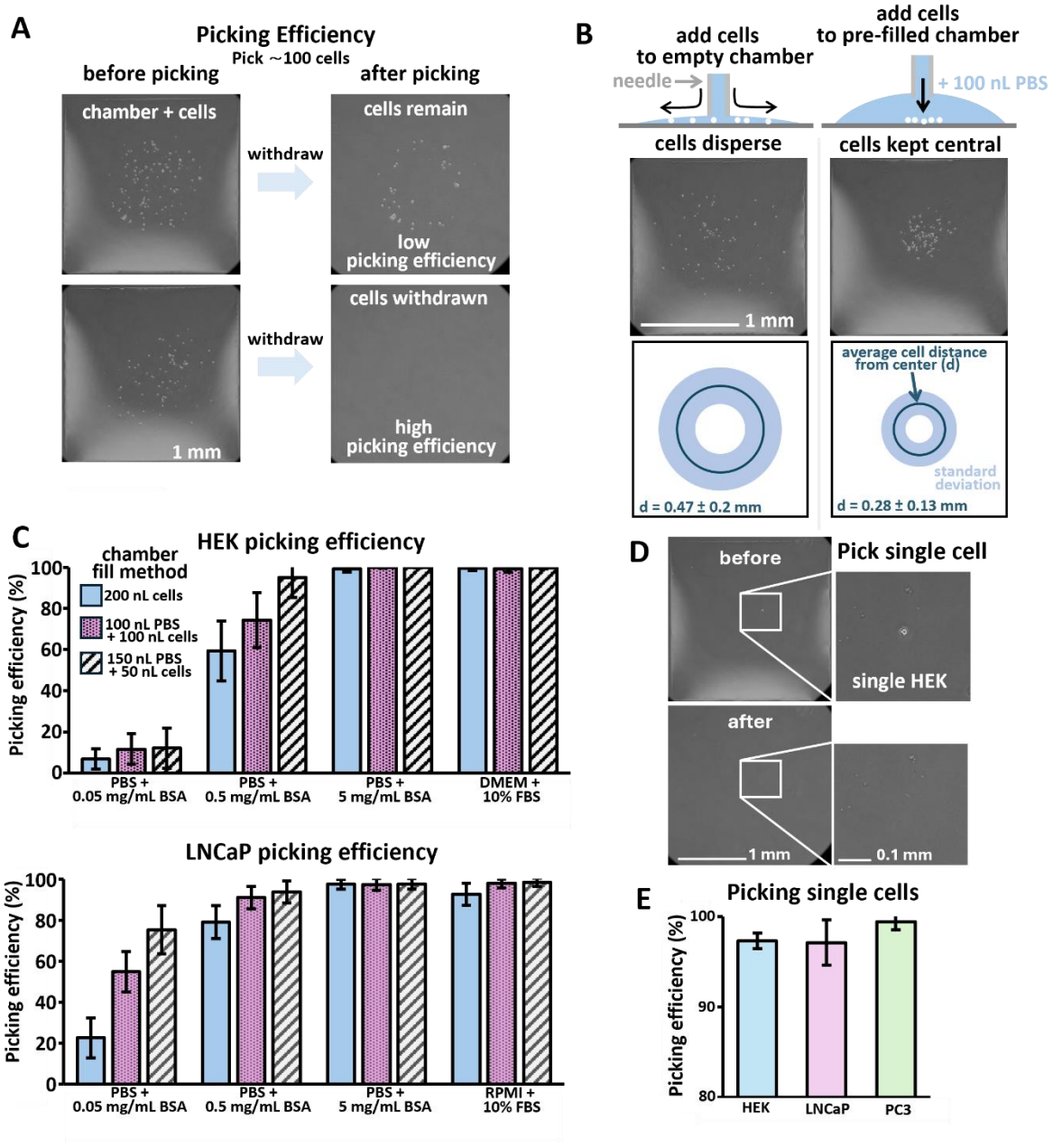

Figure S9. Cell picking optimization. (A) Examples of low and high picking efficiency. Approximately 100 cells were added to a chamber and the entire volume withdrawn. Picking efficiency was defined as the percentage of cells remaining. **(B)** Seeding cells into empty chambers resulted in dispersal, whereas pre-filling with fluid kept cells centralized within the chamber. **(C)** Picking efficiencies for HEK and LNCaP cells under varying conditions (± standard deviation). Chambers were fabricated with increasing BSA concentrations to inhibit adhesion, and the ratio of pre-fill chamber volume to added cell suspension was adjusted to maintain cell centrality and improve efficiency. **(D)** Example showing successful picking of a single cell. **(E)** Picking efficiencies for single HEK, LNCaP, and PC3 cells, using the optimized method.

Automated cell segmentation and tracking using Cellpose and ImageJ

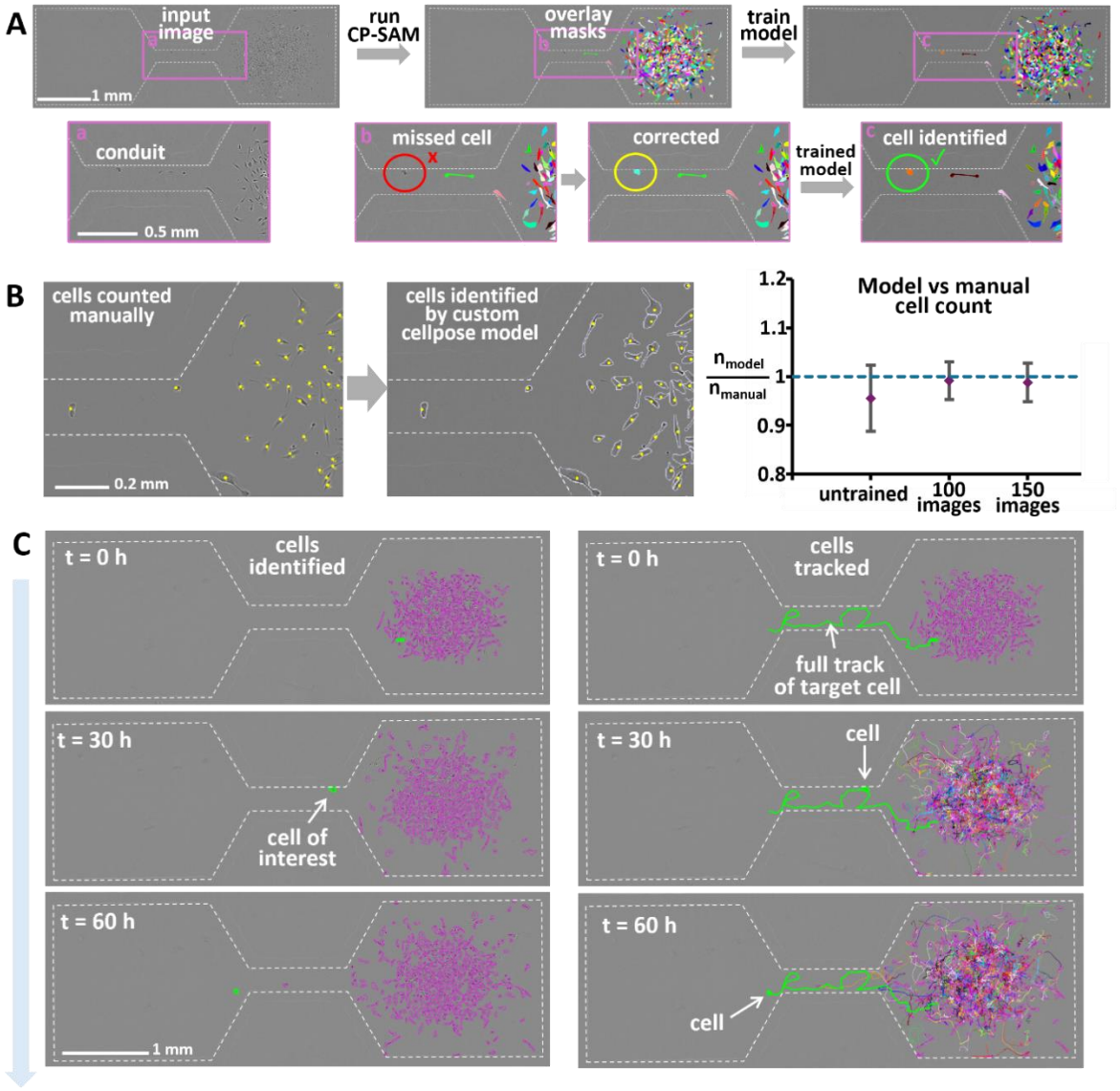

Figure S10. Automated cell segmentation and tracking using Cellpose and ImageJ. (A) Phase-contrast images of dumbbells were processed in Cellpose. Purple rectangles: zoom shown below. The CP-SAM algorithm was used for initial segmentation with missing cells corrected manually. The corrected mask is saved and the procedure repeated to train a custom model, which improved cell detection. **(B)** Segmentation accuracy was evaluated by comparing manual cell counts in 5 representative images with automated counts from the untrained model, after training on 100 images, and after training on 150 images (± standard deviation). **(C)** The custom model was integrated with ImageJ to provide initial cell segmentation, followed by tracking to extract quantitative parameters of interest. Image contrast and brightness have been adjusted for clarity.

Staining for senescence-associated markers

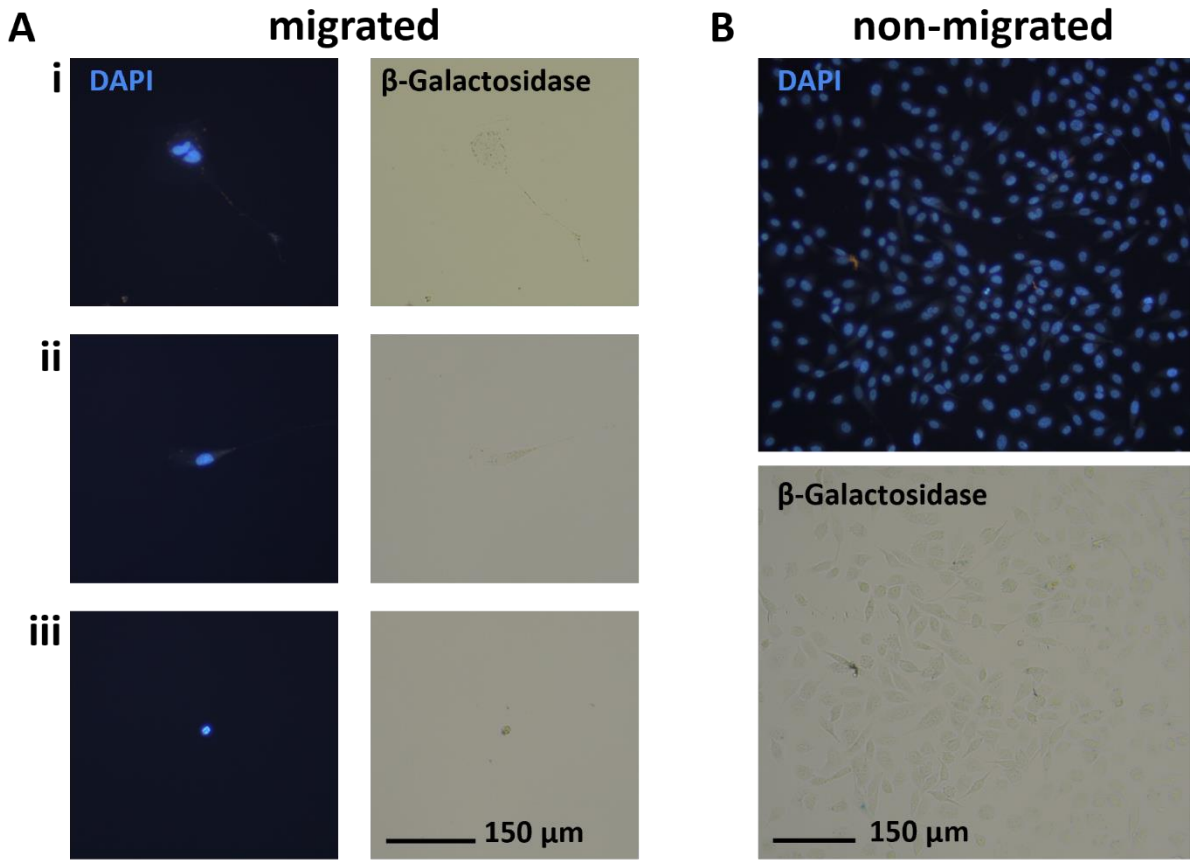

Figure S11. Staining for senescence-associated markers. (A) Representative examples of migrated cells. Each row **(i-iii)** shows a single migrated cell stained using DAPI (left) and β-Galactosidase (right). **(B)** Example images of non-migrated cells stained under the same conditions. Top and bottom panels show the same field of view. All images are 20X magnification. DAPI was imaged using blue channel fluorescence and β-Galactosidase imaged using brightfield.

Description of Supplementary Movies

Movie S1. Time-lapse movies of six representative dumbbells stitched together, each containing a migratory cell. In all cases, a single cell traverses the conduit into the opposing chamber, exhibiting diverse and dynamic morphological changes. Images were acquired hourly; the sequence is shown at increased speed and looped three times.

Movie S2. Magnified view of a single dumbbell showing pronounced morphological changes in the migrating cell over time. Images were acquired and presented as described above.

Movie S3. Magnified view of single dumbbell. In this example, the migrating cell appears more motile, with small morphological changes compared to Movie S2. Images were acquired and presented as described above.

Movie S4. Three example dumbbells where Cellpose was used for cell segmentation. In each case, the migratory cell of interest is highlighted in green. Dumbbells are stitched together from three experiments.

Movie S5. Cell tracks overlaid following segmentation and tracking in ImageJ. The same three dumbbells shown in Move S4 are displayed, with the trajectory of the migratory cell highlighted in green.

Movie S6. Heterogeneity within the migratory subpopulation revealed by cluster analysis, which identified two groups: smaller, faster-moving cells and larger, slower-moving ones. A representative example from each group is shown side-by-side for comparison.

Statement of Authorship for joint/multi-authored papers for PGR thesis

To appear at the end of each thesis chapter submitted as an article/paper

The statement shall describe the candidate's and co-authors' independent research contributions in the thesis publications. For each publication there should exist a complete statement that is to be filled out and signed by the candidate and supervisor **(only required where there isn't already a statement of contribution within the paper itself).**

Title of Paper	Identification and isolation of migratory subpopulations of cancer cells using fluid-walled microfluidics
Publication Status	Unpublished and unsubmitted work written in a manuscript style
Publication Details	Joseph A.E. Morgan, Daniele T. Cotton, Srinivasa R. Rao, Peter R. Cook, James R. Edwards, Alfonso A. Castrejón-Pita, Claire M. Edwards, Edmond J. Walsh

Student Confirmation

Student Name	Joseph Morgan		
Contribution to the Paper	Lead Author Designed experiments in discussion with co-authors. Performed biological experiments in collaboration with Daniele T. Cotton (DPhil student in molecular and cellular medicine), collected and analysed data, prepared figures and manuscript.		
Signature 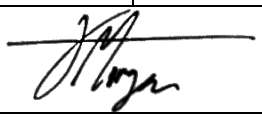		Date	07/01/2026

Supervisor Confirmation

By signing the Statement of Authorship, you are certifying that the candidate made a substantial contribution to the publication, and that the description described above is accurate.

Supervisor name and title: Prof. Edmond J. Walsh		
Supervisor comments		
Signature Ed Walsh	Date	7th Jan 2026

This completed form should be included in the thesis, at the end of the relevant chapter.

Chapter 5: Dynamic interfacial tension effects in microfluidics with fluid walls

Authors: Joseph A.E. Morgan, Federico Nebuloni, Peter R. Cook, Alfonso A. Castrejón-Pita, and Edmond J. Walsh

Abstract

Complex fabrication methods and unfamiliar materials are often blamed for limiting adoption of microfluidics by biologist. Microfluidics with fluid walls provides a solution: microfluidic arrangements are made within standard culture dishes using only cell-culture medium and immiscible fluorocarbon, FC40. Microfluidic 2D geometries are pinned by interfacial forces, and fluid-fluid boundaries allow unrestricted access. A key advantage is the ability to drive flow passively through modulating local volumes, which changes local Laplace pressures. However, predicting flow is challenging as fluid interfaces can freely expand and contract, and adsorption of proteins to the oil-medium interface, i.e. the fluid wall, alters the interfacial tension. A simple and relevant arrangement consists of two drops connected by a conduit, forming a dumbbell shape. During flow, interfaces expand and contract as drops transfer fluid between them. This results in a temporal interfacial tension due to protein absorption/desorption at the interfaces and hence creates spatial variations in interfacial tension. Consequently, when pressures equilibrate and flow stops within a microfluidic dumbbell with fluid walls, drops with equal footprints can have different heights/volumes. In this study, we investigate the impact of dynamic interfacial tension effects on the equilibration behaviour of a microfluidic dumbbell with fluid walls. We present a semi-analytical model for flow between connected drops and validate it using a combination of microfluidic experiments and interfacial tension measurements.

Introduction

Bridging the divide between engineering-driven microfluidic device design and the practical needs of biologists remains a well-recognized challenge [1]. Conventional microfluidic systems are typically bounded by solid polydimethylsiloxane (PDMS), which restricts access to contents. Open-microfluidics, which utilize a fluid-fluid interface as at least one boundary, have emerged as a promising alternative, offering enhanced accessibility for biological studies [2 - 5]. In addition to improved accessibility, the presence of an open interface enables capillarity-driven passive pumping, whereby flow is driven by gradients in Laplace pressure, without requiring external pumps [5 - 11]. Typically, fluid transport in microfluidic devices requires external syringe or peristaltic pumps, pressure controllers, or other mechanical actuators [12], [13]. More sophisticated methods, including magnetic [14] and acoustic manipulation [15], exist to control microvolumes of fluid, but these approaches also require intricate connections, external power supplies, and precise control systems. Although on-chip micropumps have been designed to overcome these challenges, they add substantial complexity to device design and fabrication [16]. These limitations have motivated the development of passive-pumping microfluidics, removing the need for external systems.

A particularly innovative class of open-microfluidics is microfluidics with fluid walls: microfluidic geometries are bound by a continuous fluid-fluid interface, rather than solid plastic [17]. Manipulating fluid volumes within fluid walls generates gradients in Laplace pressure, and can be used to drive flow passively [18], [19]. Compared with other passive-pumping open-microfluidic approaches, fluid walls offer three key advantages: (i) microfluidic arrangements are fabricated in seconds using cell-culture medium and immiscible oil, (ii) all regions are fully accessible and (iii) fluid walls can be reconfigured during an experiment [20]. They are fabricated using the immiscible fluorocarbon FC40, which confines the medium to a desired pattern [17]. FC40 offers several advantages: it is biocompatible, gas-permeable, optically transparent, and supports the culture of a broad range of cell types [21], [22]; indeed, cells exhibit enhanced viability under FC40 compared to other oils [23]. Despite the many

advantages to using FC40, a critical but often overlooked aspect is the interaction with proteins present in cell culture medium. Proteins are amphiphilic and adsorb to the oil-medium interface where they self-assemble to form viscoelastic layers that reduce interfacial tension [24 - 27]. A further complicating factor is the dynamic changes in fluid wall cross section during flow. As local regions expand and contract above a fixed footprint due to exchange of volume, adsorption combined with changes in interfacial area can alter interfacial tension [28 - 30], thereby directly impacting local Laplace pressure and flow dynamics.

This study investigates the influence of dynamic changes in interfacial tension on passive flow in microfluidic dumbbells with fluid walls. Here, dumbbells consist of a source drop and a sink drop with equal circular footprints connected by a narrow fluid conduit, where flow is always from the source to the sink. During flow, interconnected drops undergo local expansion and contraction (e.g., one drop shrinks while the other expands) and we hypothesise that these changes in interfacial area will impact local interfacial tensions, thereby local Laplace pressure and flow dynamics. Consequently, two connected drops with the same footprint geometry and contact angles < 90^{o} could, in principle, have equal pressure but different volume, due to an imbalance in interfacial tension. We use microfluidic dumbbells with fluid walls to investigate flow between drops across a range of conduit widths. We propose a predictive model that accounts for spatial differences in interfacial tension and validate this framework through a combination of microfluidic experiments and direct interfacial tension measurements.

Experimental setup

Microfluidic dumbbells with fluid walls

Fluid walls were fabricated by first coating a polystyrene Petri dish with a thin layer of cell-culture medium, which was then overlaid with FC40. A submerged microjet of FC40 was used to displace the underlying medium, forming FC40 fluid walls stabilized by interfacial

forces [18] (**Figure 1A**). By controlling the jet path, arbitrary two-dimensional geometries can be generated in seconds, bounded by continuous fluid-fluid interfaces.

A particularly useful geometry is two drops connected by a narrow conduit – a "dumbbell" (**Figure 1B**). Such microfluidic arrangements have been used in a variety of biological applications [31], [32], but flow behaviour within these systems is inherently more complex than in most rigid-walled microchannels. Fluid interfaces morph dynamically in response to pressure, making flow rates harder to predict. Recent advances have begun to characterize flow within fluid walls [33], [34] yet the influence of protein adsorption from cell-culture medium to the oil-medium interface and its effect on interfacial tension has not been investigated. This effect is further complicated by dynamic changes in interfacial area which can alter interfacial tension and hence local Laplace pressures and flow dynamics (**Figure 1C**).

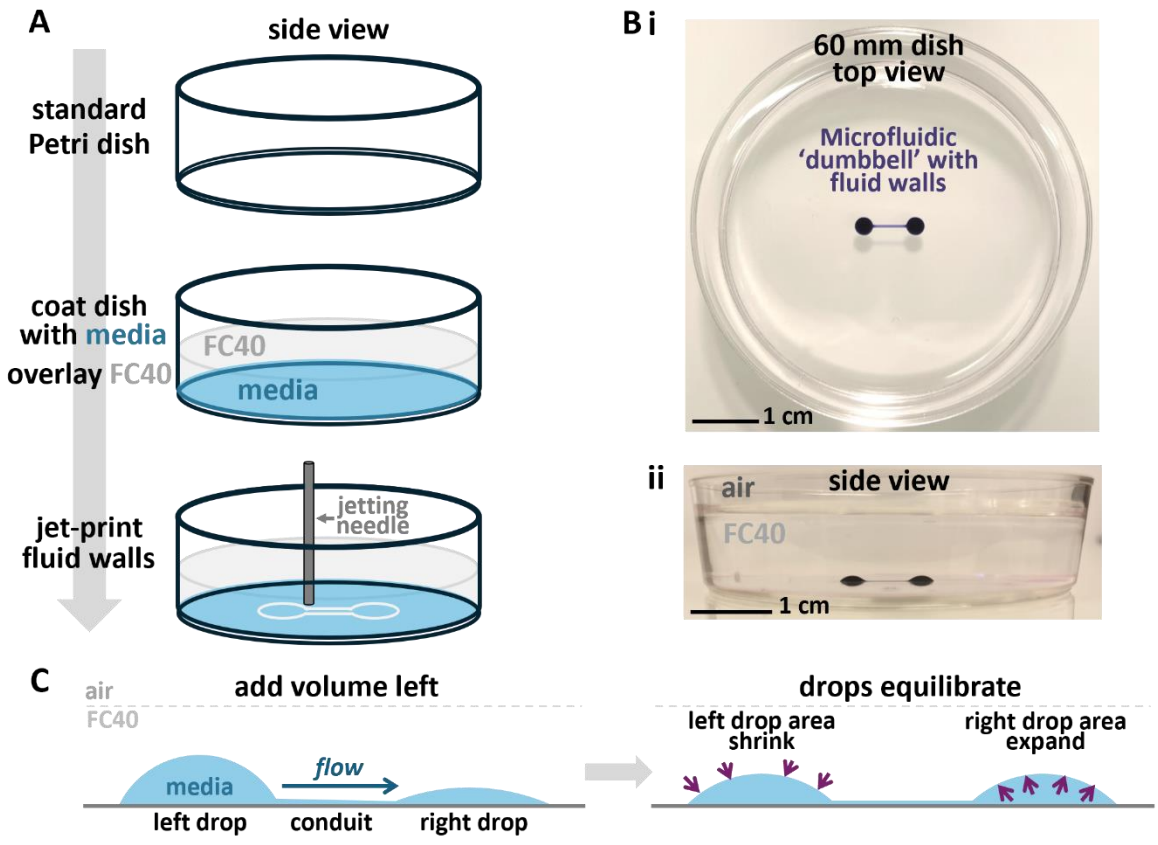

Figure 1. Microfluidic dumbbells with fluid walls. (A) Fluid walls were made by coating a standard polystyrene dish with a thin layer of cell culture medium and overlaying immiscible FC40. A submerged microjet of FC40 was then used to displace underlying media, creating FC40 fluid walls. **(B)** A dumbbell

comprising two drops connected by a conduit, shown from **(i)** above and **(ii)** side-on. **(C)** Dumbbell side view. Two drops with identical footprints are connected, adding volume to one generates a gradient in Laplace pressure that passively drives flow toward the other. During flow, the interfacial area of one drop will shrink while the other drop will expand.

Microfluidic dumbbell geometry and experimental height measurements

Within a dumbbell, each compartment has a Laplace pressure arising from local curvature of the medium-FC40 interface, given by:

$$P_L = \gamma\left(\frac{1}{R_1} + \frac{1}{R_2}\right) \quad (1)$$

Where γ is interfacial tension and $R_{1,2}$ the principal radii of curvature of the interface. If drops are sufficiently small (Bond number $<< 1$) interfacial forces dominate gravitational ones (the Bond number is defined as $Bo = \frac{\Delta\rho g V}{2\pi a\gamma}$ where $\Delta\rho$ is the density difference between medium and FC40, g is gravitational acceleration, V the drop volume and a the footprint radius) and a drop 3-D geometry may be approximated as a spherical cap, giving drop radius of curvature in terms of height h and footprint radius a:

$$R = \frac{a^2 + h^2}{2h} \quad (2)$$

Two drops at equilibrium ($P_{source} = P_{sink}$) with the same footprint radius ($a_{source} = a_{sink}$) and contact angle $\theta < 90^o$ should therefore have the same height when viewed from the side (**Figure 2Ai**). Adding volume to the source drop, up to contact angle of 90°, will increase its height and decrease local radius of curvature ($R_{source} < R_{sink}$) generating a difference in Laplace pressure $P_{source} > P_{sink}$ driving flow from the source drop to the sink (**Figure 2Aii,** assuming no gradient within the drop itself). Conduit cross-sectional geometry also changes in response to pressure gradients: during flow, conduit centre height varies along its length l_c from where it joins the source drop, $h_{c(max)}$, to height where it joins the sink, $h_{c(min)}$[33]. Local heights then change dynamically as volume is exchanged between drops and pressures equilibrate. Spherical cap geometry enables estimation of drop volume V from height measurements:

$$V = \frac{\pi h}{6}(3a^2 + h^2) \tag{3}$$

Flow rate Q is then given by the rate of change in drop volume. We designed a dumbbell with a curved conduit so that both drops fit within the field of view of a camera when imaged from the side (**Figure 2B**). Dumbbells were fabricated within flat-sided polystyrene dishes (**Figure 2C**) and experiments were initiated by adding volume to the source drop. Both drops were imaged regularly and heights variation with time measured.

The flow rate between reservoirs of our dumbbells depends on fluid wall geometry, local volumes, and interfacial tension between medium and oil overlay. We focused on the conduit width, given its relevance to the stability of diffusion gradients in biological experiments [32], [35], and a small change allows large differences in flow rate (previous studies have shown that flow through a conduit with fluid walls scales with the seventh power of conduit half-width [19], [33]). Variables kept constant include the source and sink footprint diameters (both 3 mm), the conduit length (10 mm) and the volume added to the source drop to initiate flow (3.5 µL) giving an initial contact angle of ~ 62°.

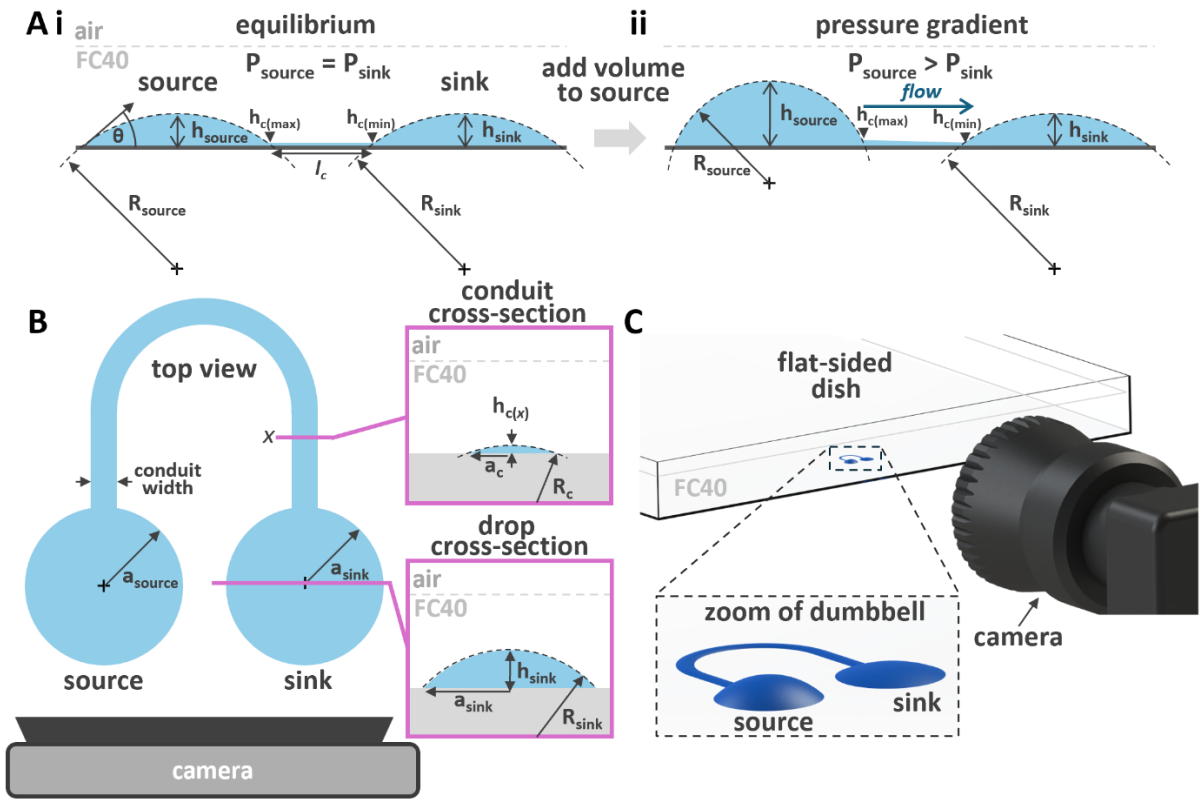

Figure 2. Dumbbell geometry and experimental setup. (A) Dumbbell 3-D geometry viewed side-on. (**i**) Initially at equilibrium, (**ii**) adding volume to the left drop (source) will decrease local radius of curvature and increase Laplace pressure, driving flow from the source drop to the sink. **(B)** A dumbbell with a curved conduit allows both drops to fit within the field of view of a camera without the conduit compromising drop image. **(C)** Dumbbells were jet printed in large rectangular dishes for improved side-on imaging over standard curved Petri dishes (dumbbell shown to scale).

Theory

A model for predicting drop heights

Total pressure P within a pinned drop submerged under FC40 is approximated as the sum of the Laplace and hydrostatic pressures [17]:

$$P = \frac{2\gamma}{R} + \rho_{media} g h + \rho_{FC40} g h_{FC40} \tag{4}$$

Where ρ_{media} and ρ_{FC40} are the densities of media and FC40 respectively, g is gravitational acceleration, and h_{FC40} is the height of the FC40 overlay. Spherical-cap geometry gives Laplace pressure in terms of drop height and footprint radius:

$$P_L = \frac{4\gamma h}{a^2 + h^2} \tag{5}$$

Within the conduit, one radius of curvature is considered infinite such that $P_{L(conduit)} = \gamma / R_c$ where $R_c$is conduit cross-sectional radius. Conduit height is typically much less than conduit half-width ($h_c \ll a_c$) allowing approximation of Laplace pressure $P_{L(conduit)} = 2\gamma h_c / a_c^2$ [33].

We consider pressure within the source equal to the pressure at the conduit opening, and sink pressure equal to the conduit end [19]. Equating pressures at the junction between the source and conduit gives:

$$\frac{4\gamma h_{source}}{a_{source}^2 + h_{source}^2} + \Delta\rho g (h_{max} - h_{source}) = \frac{2\gamma h_{max}}{a_c^2} \tag{6}$$

Where h_{max} and $R_{c(max)}$ are the height and radius of the conduit at the junction with the source drop. A previous study by Deroy et al. [33] found that the height of a fluid-walled conduit $h_{c(x)}$ varies along its length x with flow rate Q, viscosity μ and conduit half-width given by the semi-analytical solution:

$$h_{c(x)}^4 = \frac{26.08 Q \mu a_c x}{\gamma} + h_0^4 \tag{7}$$

Where h_0 is the conduit height at the junction with the sink. Considering total conduit length ($x = l_c$), equations 6 and 7 combine to relate source and sink drop heights:

$$Q = \frac{\gamma}{26.08 \mu a_c l_c} (h_{max}^4 - h_0^4) \tag{8.1}$$

where:

$$h_{max} = \frac{2\gamma}{2\gamma - \Delta\rho g a_c^2} \left[\left(\frac{2 h_{source} a_c^2}{a_{source}^2 + h_{source}^2} \right) - \left(\frac{\Delta\rho g h_{source} a_c^2}{2\gamma} \right) \right] \tag{8.2}$$

and:

$$h_0 = \frac{2\gamma}{2\gamma - \Delta\rho g a_c^2} \left[\left(\frac{2 h_{sink} a_c^2}{a_{sink}^2 + h_{sink}^2} \right) - \left(\frac{\Delta\rho g h_{sink} a_c^2}{2\gamma} \right) \right] \tag{8.3}$$

Experimentally, flow rates are inferred from drop height measurements and spherical-cap geometry:

$$Q = -\frac{\pi}{2} (a_{source}^2 + h_{source}^2) \frac{dh_{source}}{dt} \tag{9}$$

Where flow is from source to sink. Combining components of equation 8 and 9 gives predicted rate of change in height of the source drop:

$$\frac{dh_{source}}{dt} = -\frac{1.2272\gamma^5}{\mu\pi a_c l\left(a_{source}^2 + h_{source(t)}^2\right)(2\gamma - \Delta\rho g a_c^2)^4}\left[\left(\frac{2h_{source(t)}a_c^2}{a_{source}^2 + h_{source(t)}^2} - \frac{\Delta\rho g h_{source(t)}a_c^2}{2\gamma}\right)^4 - \left(\frac{2h_{sink(t)}a_c^2}{a_{sink}^2 + h_{sink(t)}^2} - \frac{\Delta\rho g h_{sink(t)}a_c^2}{2\gamma}\right)^4\right] \quad (10)$$

Given a constant total volume V_T in the system (conduit volume is considered negligible relative to drop volumes), the height of the sink drop is related to the source drop:

$$\frac{\pi}{6}h_{sink(t)}\left(3a_{sink}^2 + h_{sink(t)}^2\right) = V_T - \frac{\pi}{6}h_{source(t)}\left(3a_{source}^2 + h_{source(t)}^2\right) \quad (11)$$

Equations 10 and 11 were solved to give predicted change in source and sink drop heights over time using the forward Euler method in MATLAB (for a more detailed derivation see supplementary **Figure S1** [p. 131]).

Results

Interfacial tension, model prediction, and drop height measurements

Interfacial tension between FC40 and cell-culture medium was obtained through pendant-drop tensiometry. A droplet of FC40 was suspended in a cuvette of medium (10% serum) and the drop profile measured to determine interfacial tension (**Figure 3Ai**). A static pendant drop provided the equilibrium interfacial tension, γ_{eq}, which stabilised at ~ 22.7 mN/m (**Figure 3Aii**). Immediately after droplet formation, the interfacial tension was substantially higher (~45 mN/m, maximum expected value of ~52 mN/m for FC40 and water [36]) and reduced to γ_{eq} over ~ 3 hours, consistent with the time-dependent adsorption of proteins within the medium that lowers interfacial tension [37]. This behaviour was not observed for FC40 in clean water, where the interfacial tension remained constant (supplementary **Figure S2** [p. 136]). The obtained value for γ_{eq} was then used to predict changes in dumbbell drop heights.

Dumbbells were imaged side-on to measure changes in drop heights (**Figure 3B**). During fabrication, medium (supplemented with 10% serum) was displaced by the FC40 jet, giving irregular starting volumes in each drop. This was withdrawn prior to adding volume (supplementary **Figure S3** [p. 137]). First, we examined conduits of width ~ 0.5 mm. Flow was initiated by adding 3.5 µL to the source drop. Dumbbells were imaged side-on every minute for 12 hours and drop heights measured (**Figure 3C**). Model prediction showed that drop heights should equilibrate within ~ 8 hours (**Figure 3D**). We compared a Laplace-only model with one incorporating hydrostatic contributions, both considering a constant interfacial tension. Including hydrostatic forces increased predicted equilibration time due to a reduction in net driving pressure due to the density difference between medium and FC40. Notably, normalised heights at equilibrium should not converge to 0.5 because spherical-cap height and volume are non-linearly related; instead, the model predicts a final normalised height of 0.54 for two drops with equal footprints and volumes.

Interestingly, drop heights did not equilibrate despite identical footprint geometries (**Figure 3D**). We hypothesised that this offset was due to spatial differences in interfacial tension caused by protein adsorption and desorption at the oil-medium interface. Fluorocarbons are exceptionally hydrophobic, resulting in strong interactions with the hydrophobic regions of amphiphilic proteins [38]. Prior studies have shown that adsorption of serum proteins such as albumin at highly non-polar oil interfaces induces partial unfolding and the irreversible formation of viscoelastic films which lower interfacial tension [39], [40]. The effect of protein adsorption on morphing fluid walls is further complicated during flow, as shrinking interfacial area concentrates interfacial proteins [41], [42], and expansion has the opposite effect. Consequently, dumbbells overlaid with fluorocarbon oil could exhibit spatial variations in interfacial tension as reservoirs expand and contract. These differences were hypothesised to explain the observed mismatch in drop heights when flow stops despite equal footprint geometry. An intuitive control experiment would be to fabricate dumbbells using

protein-free fluids. However, this was not possible since adsorption of such molecules is required to stabilize pinning lines and hence enable dumbbell 2D geometry.

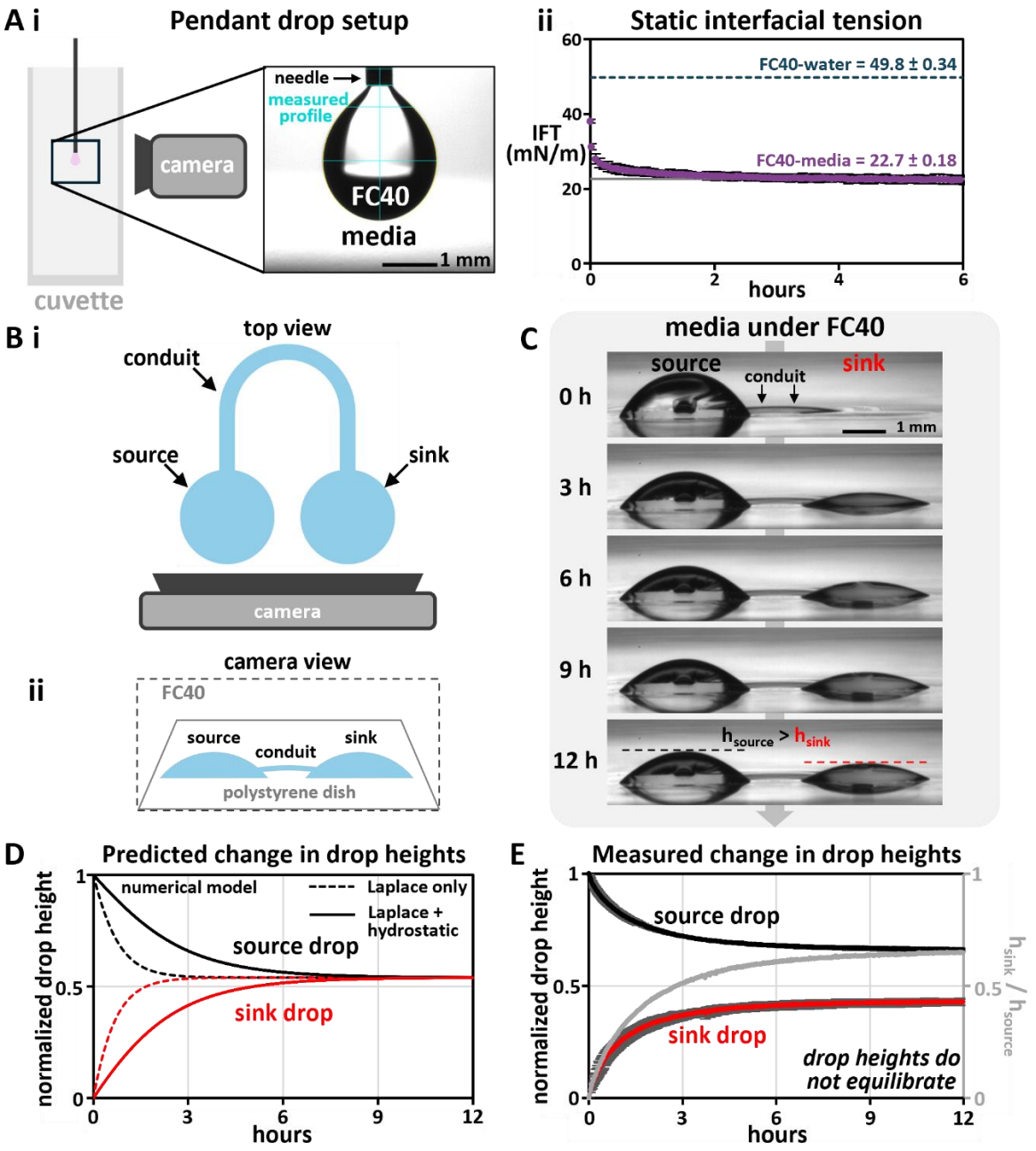

Figure 3. Interfacial tension, model prediction, and drop height measurement. (A) Interfacial tension measurements. **(i)** A pendant drop of FC40 was formed within a cuvette filled with cell culture medium and drop profile analysed to determine interfacial tension. **(ii)** Static interfacial tension between FC40 and medium. Interfacial tension decreased to an equilibrium value of 22.7 mN/m (mean ± s.d., n=3). No such decrease was observed between FC40 and water. **(B)** Dumbbells were imaged from side-on to measure changes in drop heights, shown from **(i)** top and **(ii)** side-on. **(C)** Camera view of dumbbells. Adding volume to the source drop drives flow through the conduit into the sink. **(D)** Predicted change in drop heights for a representative dumbbell geometry, comparing Laplace-only driven flow

and hydrostatic contributions. Heights are normalized to the initial maximum height of the source drop **(E)** Measured drop heights over time. Drop heights did not equilibrate under FC40, contrary to model predictions (mean ± s.d., n=3, normalized to max height of the source drop).

Dynamic interfacial tension effects using pendant drop tensiometry

To study the effect of expanding/contracting interfacial area, a programmable syringe pump was used to withdraw volume from the pendant drop at controlled rates (**Figure 4Ai**). The acceptable volume range for accurate interfacial tension measurement was determined from the Worthington number [43]:

$$Wo = \frac{\Delta\rho g V_d}{\pi\gamma d_n} \tag{12}$$

which captures the balance between gravitational and capillary forces acting on a pendant drop. Here, V_d is drop volume and d_n the wetted needle diameter ($\sim$ 0.42 mm). Initial drop volumes were between 0.8 and 0.4 calculated using γ_{eq}, and confirmed that static drops of both sizes exhibited the same decrease in interfacial tension to γ_{eq} (supplementary **Figure S4** [p. 138]). A large drop was created, equilibrated, and volume withdrawn at various rates (**Figure 4Aii**). In all cases, interfacial tension reduced with interfacial area (**Figure 4Aiii**) due to protein packing at the interface [41], [42]. The magnitude of reduction in interfacial tension was proportional to the total area reduction; however, the rate of contraction had little effect on the rate of change in interfacial tension, as all conditions collapsed onto approximately the same curve.

Next, drops were expanded between the same limits (**Figure 4Bi**). Volume was added at various rates (**Figure 4Bii**) and interfacial tension generally increased proportional to the rate of expansion (**Figure 4Biii**). When expansion was sufficiently slow, the increase in interfacial tension was negligible, consistent with adsorption kinetics outpacing the creation of new interfacial area. For all conditions where expansion produced a measurable increase in

interfacial tension, drops returned to γ_{eq} once expansion ceased, with recovery closely matching that of a static drop (supplementary **Figure S5** [p. 139]).

Comparison between expanding and contracting drops revealed a pronounced asymmetry in interfacial behaviour (**Figure 4C**). Expanding drops relaxed to γ_{eq} once expansion ceased, whereas shrinking drops did not recover over experimental timescales. This is consistent with previous reports of irreversible adsorption and saturation of proteins at oil-water interfaces, thereby maintaining a reduced interfacial tension [44], [45], lower than γ_{eq}.

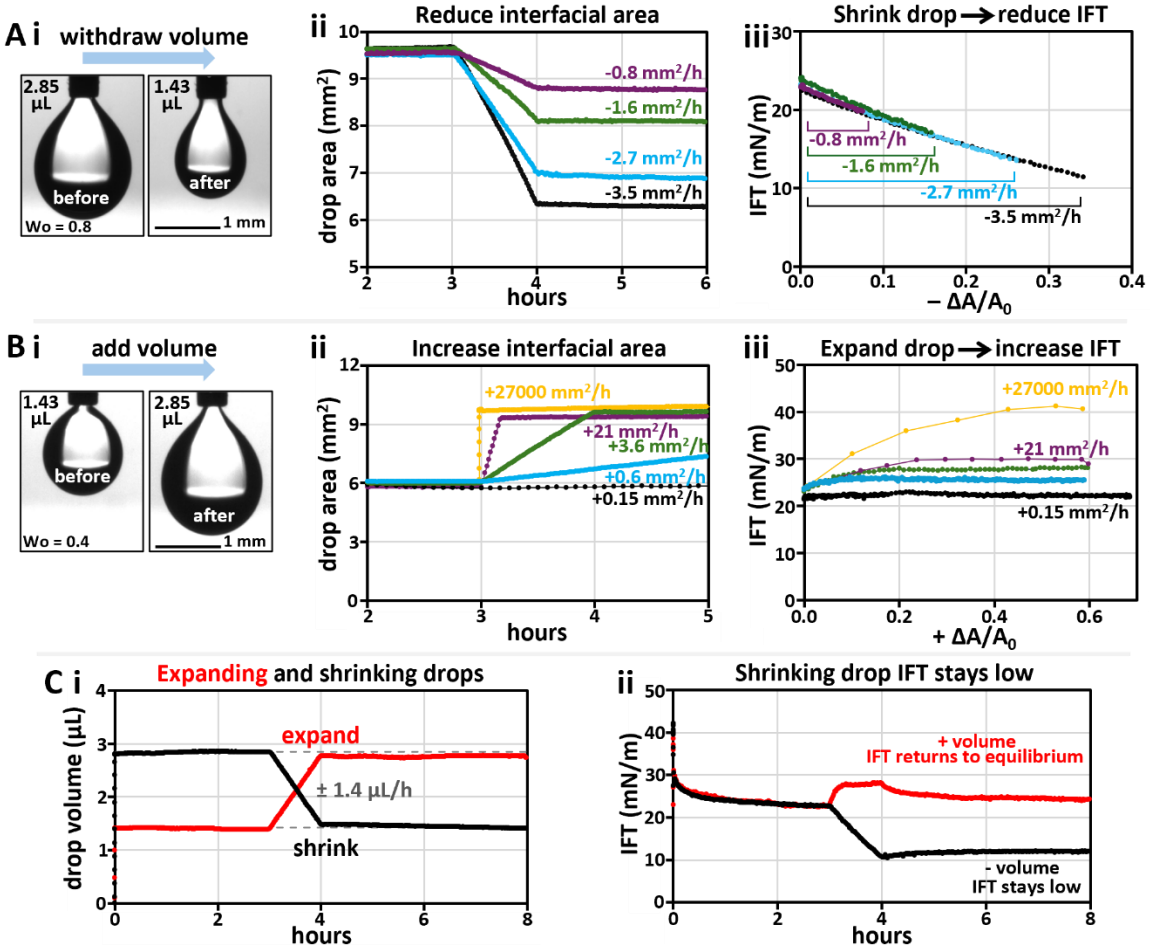

Figure 4. Dynamic interfacial tension effects measured using pendant drop tensiometry. (A) Effect of withdrawing volume. **(i)** A large drop (Wo = 0.8) was created and **(ii)** volume withdrawn to reduce interfacial area both at varying rates and amounts. **(iii)** Contraction of interfacial area lowered interfacial tension. **(B)** Effect of adding volume. **(i)** A small drop was created (Wo = 0.4) and **(ii)** volume added, increasing interfacial area different rates. **(iii)** Increasing interfacial area raised interfacial tension proportionally to expansion rate, while very slow expansion caused negligible change. **(C)** An analogy

for drops in a dumbbell. Expansion of interfacial area increases interfacial tension, which relaxes towards equilibrium, whereas contraction decreases interfacial tension, which does not recover.

Modelling microfluidic dumbbell behaviour using a pendant drop

As changes in interfacial tension were shown to be minimal for slow expansion rates, it is therefore assumed no change from γ_{eq} during expansion of the sink drop or conduit (average expansion rate of ~ 0.08 mm^2/h for the condition under FC40 shown in **Figure 3E**). In contrast, the contracting source drop exhibits an irreversible reduction in interfacial tension. Over the relevant experimental range (i.e. between Wo = 0.4 – 0.8), pendant-drop interfacial area was approximately linearly correlated with volume ($A \approx 2.64V + 2.32$, supplementary **Figure S6** [p. 140]). This enabled use of drop volume as a reliable proxy for pendant drop area. Using the programmable syringe pump, drop volume was adjusted to produce equivalent percentage changes in interfacial area to those estimated for the source drop using spherical-cap geometry:

$$A = \pi(a^2 + h^2) \tag{13}$$

Experimentally there were four stages from dumbbell fabrication to equilibration (**Figure 5Ai**), (1) the source drop is initially empty, (2) 3.5 µL medium added, increasing drop area ~35%, (3) volume drains from the source to sink and (4) drops equilibrate after ~ 3 hours. Initially, we assume source and sink drops equilibrate to the same height giving an area reduction of the source drop of ~ 18%. The changing surface area was replicated with the pendant drop to experimentally determine the expected temporal interfacial tension. First a drop was formed and allowed to reach γ_{eq} and then subjected to equivalent percentage changes in area (**Figure 5Aii**), while changes in interfacial tension were recorded (**Figure 5Aiii**). Upon expansion, γ exhibits a transient spike before decreasing as the interface contracts, falling below γ_{eq}. The change in interfacial tension with the reduction of interfacial area can be linearly approximated:

$$\frac{\gamma(A)}{\gamma_{eq}} = a\left(\frac{\Delta A}{A_0}\right) + b \tag{14}$$

Where A_0 is the initial interfacial area and $\Delta A = A(t) - A_0$ (the ratio $\Delta A/A_0$ is referred to as area strain [46]). Pendant drop experiments yielded constant values of $a = 2$ and $b = 1.13$. The small initial inflection reflects simultaneous transient adsorption and area reduction, whereas the subsequent linear region is driven by removal of interfacial area during contraction (**Figure 5Aiv**). This linear γ-area relationship was incorporated into an updated height-prediction model in which the interfacial tension of the source drop varies with area. The rate of change in source drop height becomes:

$$\frac{dh_{source}}{dt} = -\frac{1.2272\gamma_{eq}^5}{\mu\pi a_c l\left(a_{source}^2 + h_{source(t)}^2\right)\left(2\gamma_{eq} - \Delta\rho g a_c^2\right)^4}\left[\left(\left(\frac{\gamma_{source(A)}}{\gamma_{eq}}\right)\left(\frac{2h_{source(t)}a_c^2}{a_{source}^2 + h_{source(t)}^2}\right)\right.\right.$$
$$\left.\left. - \left(\frac{\Delta\rho g h_{source(t)}a_c^2}{2\gamma_{eq}}\right)\right)^4 - \left(\left(\frac{2h_{sink(t)}a_c^2}{a_{sink}^2 + h_{sink(t)}^2}\right) - \left(\frac{\Delta\rho g h_{sink(t)}a_c^2}{2\gamma_{eq}}\right)\right)^4\right] \tag{15}$$

Equations 14 and 15 were solved numerically in MATLAB. The model predicts that the interfacial tension of the contracting source drop falls below that of the expanding sink (**Figure 5Bi**). Consequently, two drops with identical footprint geometries can equilibrate to the same Laplace pressure while maintaining different spherical-cap heights (**Figure 5Bii**), consistent with experimental findings.

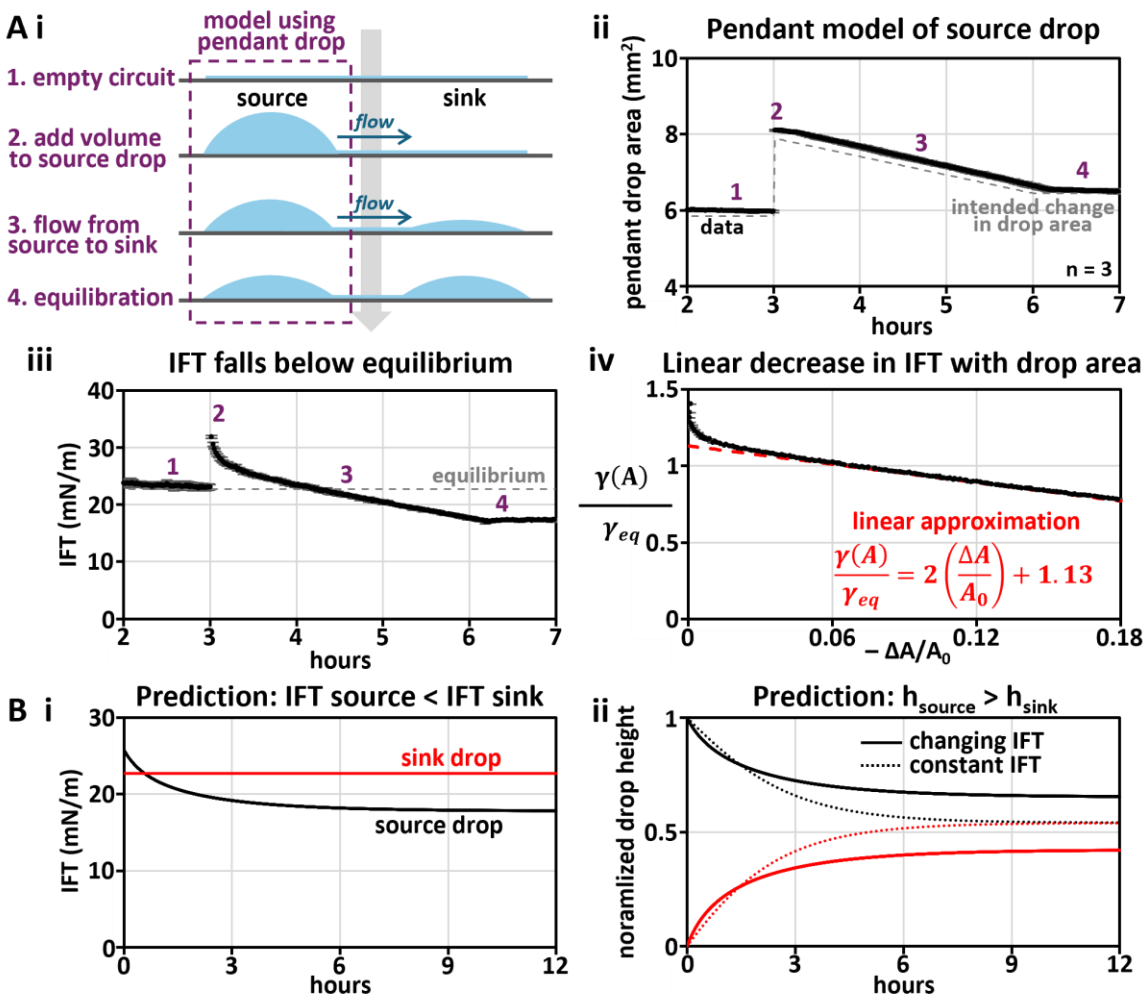

Figure 5. Experimental analogy between pendant drop dynamics and dumbbells. (A) A pendant-drop model of the source drop in a dumbbell. **(i)** Initially empty, adding volume causes flow to the sink. **(ii)** Changes in interfacial area equivalent to the source drop were imposed on a pendant drop using a programmable syringe pump. **(iii)** Starting at equilibration, increasing area caused a transient rise in interfacial tension. As area decreases, interfacial tension falls below equilibrium. Stages correspond to the same as previous panels. **(iv)** Interfacial tension decreased approximately linearly as interfacial area reduced (mean ± s.d., n=3). **(B)** Model incorporating dynamic interfacial tension. **(i)** Interfacial tension of the sink drop remains approximately constant, while the source drop decreases below that of the sink due to contraction. Predicted decrease in interfacial tension becomes nonlinear because the source drop area changes nonlinearly as the pressure gradient between drops diminishes. **(ii)** This interfacial tension difference causes a height difference between the drops when flow stops.

Comparison between data and model considering dynamic changes in interfacial tension

We compared the predictive model incorporating dynamic interfacial tension of the source drop against experimental data from three dumbbell geometries, all overlaid with FC40. Conduit half-width-to-length ratios of 0.033, 0.023 and 0.018, representing conduit widths of 0.65 mm, 0.46 mm and 0.36 mm respectively, were examined (**Figure 6Ai, ii, iii**).

Alignment between model prediction and experimental data improved as equilibration time increased. Under these slower-flow condition, transient adsorption effects diminish and dynamic changes in interfacial tension are dominated by interfacial area loss, yielding improved model accuracy at lower a_c/l ratios (<5% average error between prediction and source drop height data for ratios of 0.023 and 0.018). In the narrowest condition, average agreement between prediction and measured change in source drop height was within 98%. In the widest geometry, drops equilibrated within ~ 1 hour with a greater average mismatch of 10% between source drop data and prediction – likely due to transient adsorption having a greater effect on interfacial tension over shorter timescales. Agreement between prediction and data was generally improved in the source drop than the sink, with average error of ~ 8% across all tests for the sink. This is attributed to the predictive model only considering dynamic interfacial tension changes in the source. Changes in the sink and conduit are considered negligible but may be sufficient to inflict a small offset between predicted and measured sink height during flow. This was not observed at equilibrium where there was strong alignment between predicted sink height and data (within 3%, excluding the widest conduit condition).

The equilibration time was defined here as the time taken for the flow rate to decrease to below 10% of the initial maximum value, where flow rate was calculated from the rate of change in volume of the source drop ($Q = -dV_{source}/dt$) found from drop height using spherical-cap geometry (**Figure 6B**). Equilibration time was then predicted numerically using equation 15 and agreement between prediction and data increased as conduit width

decreased, with averaged errors of 40%, 17% and 7% for the widest to narrowest conduits, respectively. In each case, a two-term exponential function was fitted to the experimental change in volume over time to smooth the data and estimate flow rate from the source drop (performed using MATLAB curve-fitting toolbox, supplementary **Figure S7** [p. 141]).

Together, these results show that (i) dynamic changes in interfacial tension during flow result in height differences between two drops connected by a conduit that would otherwise be equal, and (ii) the developed model provides a practical tool for estimating equilibration times in microfluidic dumbbells with fluid walls, which will aid users designing passive perfusion assays or confinement-based chemotaxis experiments [32].

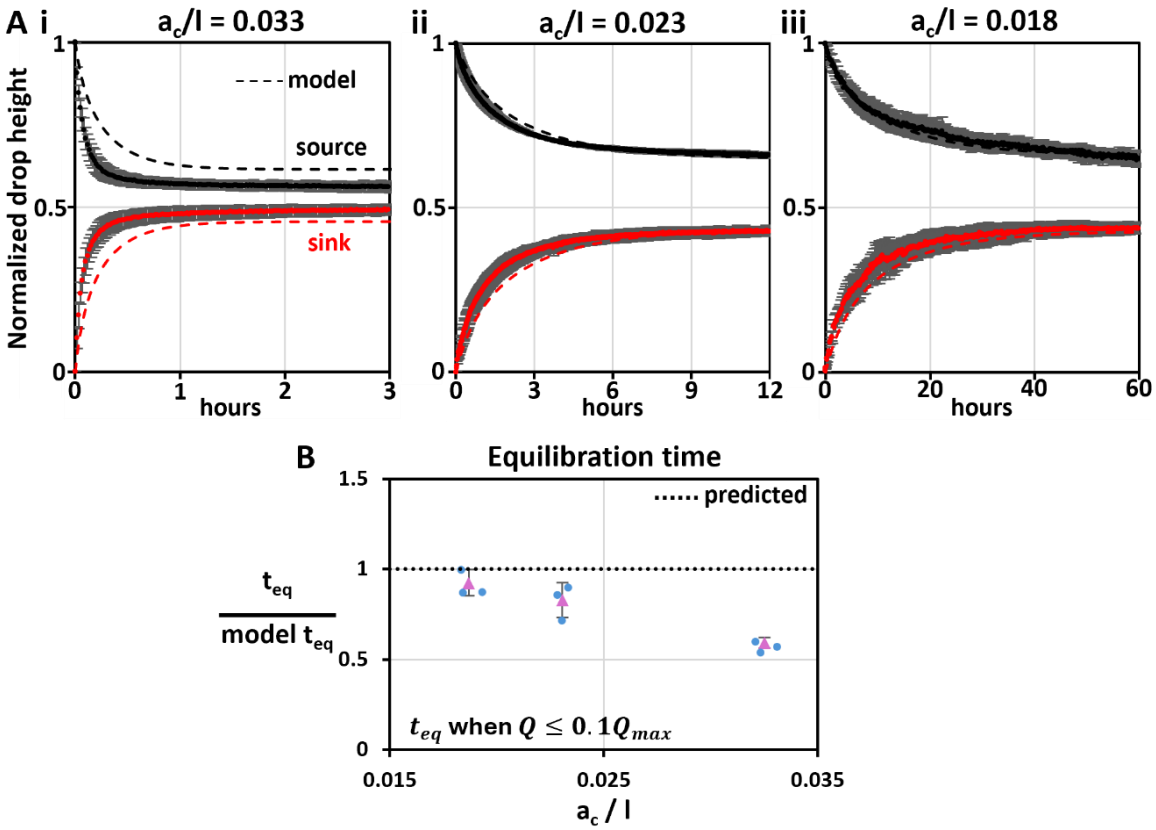

Figure 6. Varying conduit width and equilibration time. (A) Comparison between predictive model incorporating dynamic interfacial tension of the source drop with experimental measurements. Three conduit geometries were examined, corresponding to conduit half-width-to-length ratio of **(i)** 0.065, **(ii)** 0.046, and **(iii)** 0.037 (mean ± s.d., n = 3). **(B)** Predicted dumbbell equilibration time. As conduit width decreased, equilibration times increased, and model-experiment agreement improved.

Discussion

The adsorption of proteins to the oil-medium interface and its impact on flow within microfluidics with fluid walls has remained largely unexplored. We studied two circular drops connected by a conduit (**Figure 1**) and tracked drop heights to derive flow rates between them (**Figure 2**). Drop heights did not equilibrate when overlaid with FC40 – contrary to model predictions assuming a constant interfacial tension (**Figure 3**). Fluorocarbon oils are exceptionally hydrophobic [38], leading to strong protein adsorption and denaturation at the oil-medium interface. This reduces interfacial tension, and reduction is irreversibly enhanced as interfacial area shrinks (**Figure 4**). Therefore, drops with different interfacial tensions may equilibrate while maintaining different heights, supporting our hypothesis. Since fluid walls comprise a continuous fluid-fluid interface, it would be reasonable to assume that spatial gradients in interfacial tension would relax through lateral redistribution of interfacial species, for example via Marangoni stress. However, protein adsorption produces viscoelastic films that suppresses surfactant mobility [47]. Consequently, different regions of a dumbbell can maintain different interfacial tensions, despite being part of the same continuous interface.

Pendant drop experiments revealed two key properties of the FC40-medium interface; (i) as interfacial area decreased, interfacial tension decreased proportionally to the reduction in interfacial area and did not recover, and (ii) as interfacial area increased, so did interfacial tension, in proportion to the rate of expansion, and returned to γ_{eq} once expansion ceased. Interfacial changes in the contracting source drop were modelled by subjecting a pendant drop to similar percentage changes in interfacial area (**Figure 5Ai, ii**), and interfacial tension decreased below γ_{eq} during contraction (**Figure 5Aiii**). This provided an approximately linear relationship between the decrease in interfacial tension and the relative reduction in interfacial area, which was incorporated into a new predictive model (**Figure 5B**). While a single pendant drop size is presented here, the linear relationship was also validated for a second, smaller drop (supplementary **Figure S8** [p. 143]) supporting the robustness of the approximation. The predicted equilibrated source height was greater than the sink – consistent with experimental

observations. This was compared to experimental data for three conduit widths, and agreement improved for narrower conduits and longer timescales (**Figure 6A**). We also proposed a practical definition for equilibration time based on decay of flow rate and showed that model predictions improved for narrower conduits (**Figure 6B**).

Some limitations should be noted. The model only accounts for interfacial tensions changes due to area reduction of the source drop, which dominate over longer timescales. Transient adsorption, or dynamic increases in interfacial tension during expansion, are not yet incorporated. Additionally, applications using higher or lower serum concentrations within cell culture medium may exhibit different interfacial changes. Finally, an assumption is that the source interface is always contracting, and the sink always expanding. For larger features (Bond number > 1) or systems with contact angles > 90°, the direction of flow may be reversed, and the model would require adjustment accordingly.

This work demonstrates that dynamic changes in interfacial tension – driven by protein adsorption to contracting interfaces – can govern flow within fluid walls. Agreement between prediction and experiments indicate that these interfacial effects underlie the mismatched drop heights at equilibrium, while providing a practical way to estimate equilibration times, especially at low a_c/l ratios. These findings will be useful in any open or under-oil microfluidic systems with evolving interfaces where significant protein adsorption is present, help inform design of future microfluidic assays with fluid walls, and stimulate new studies where dynamic interfacial area changes influence protein adsorption.

Materials and methods

Cell culture medium and oil

Cell culture medium consisted of high glucose Dulbecco's modified eagle medium (DMEM, Sigma-Aldrich) supplemented with 10% foetal bovine serum (FBS, Sigma-Aldrich). After adding FBS, medium was filtered through a 0.2 μm filter (Nalgene™, Thermo Fisher), aliquoted into 15 mL centrifuge tubes (Sarstedt) and stored at 5°C. FC40 (Fluorinert™, 3M) was used as the oil overlay and was stored at room temperature.

Fluid printer

The fluid printer (iotaSciences) comprised a custom three-axis traverse that provided spatial control of a jetting needle (70 μm internal diameter, iotaSciences). The needle was connected via Teflon tubing to a syringe pump (KD Scientific) fitted with a 2.5 mL glass syringe (Hamilton) containing FC40. Printer commands were written in GCMC and compiled to G-code.

Microfluidic dumbbell fabrication

Microfluidic dumbbells were made by first adding 4 mL medium to a rectangular polystyrene petri dish (Nunc™, Thermo Scientific) followed by manual withdrawal of medium (1 mL pipette) to leave a thin film. For the dumbbells shown in Figure 1, 60 mm dishes (Corning) were used. This was quickly overlaid with ~ 20 mL FC40 (or silicon oil/tetradecane) to prevent evaporation of the underlying medium. The fluid printer was then used to jet FC40 through the overlay and thin film of medium (jet rate 480 μL/min, positioned ~0.3 mm above dish surface) displacing the underlying medium to form FC40 fluid walls that define the dumbbell geometry. Dumbbell geometry was verified using an inverted microscope (Olympus CKX53). After jetting, dishes were left for ~ 30 mins with one side elevated such that excess medium would accumulate and was removed manually.

Dumbbell chamber height measurements

To investigate flow dynamics, dishes containing dumbbells were imaged side-on (Point Grey camera, First Ten Angstroms). Dishes were aligned after jetting and the small volume of media swept into dumbbells used to focus on both drops. Fluid handling was via a dispensing needle (25 gauge) connected to a 50 µL syringe (Hamilton) filled with medium via Teflon tubing and controlled via programmable syringe pump (PhD Ultra, Harvard Apparatus). Prior to filling, the dispensing needle (held by a 3D printed mount) was lowered through the overlaying oil so that the needle tip just touched the media-oil interface, and any residual medium was withdrawn from the chambers, ensuring a unform start point across experiments. To start each experiment, 3.5 µL medium was then added to the left drop. As medium flowed from the left drop to the right, drop heights were recorded and measured using FTA32 software (First Ten Angstroms) using the outer diameter of the needle (0.51 mm) as a scale reference. After experiments, dumbbells were imaged from below using the microscope and geometry measured using ImageJ.

Interfacial tension measurements

Static and dynamic interfacial tension measurements were taken using the FTA1000 B Class drop shape instrument (First Ten Angstroms). Pendant drops of FC40 were created on the end of a needle (25 gauge), connected to a 50 µL syringe (Hamilton) filled with FC40 via Teflon tubing and controlled via programmable syringe pump (PhD Ultra, Harvard Apparatus). The needle was lowered into a cuvette filled with either deionized water (Sigma Aldrich) or medium and then FC40 pumped through the needle to create the pendant drop. To enable dynamic interfacial tension measurement, addition and withdrawal of volume from the drop was programmed into the syringe pump using the inbuilt interface. The drop profile was then measured in FTA32 software, using the dispensing needle outer diameter as scale reference.

Calculations and statistical analysis

All calculations and statistical analysis were performed using MATLAB (2023a, MathWorks) and Excel (version 2404, Microsoft).

Acknowledgements

The authors thank iotaSciences (iota Sciences Ltd, Begbroke Science Park, Oxfordshire, OX5 1PF) who provided support to J.A.E.M and F.N and equipment for the study.

References

[1] E. Berthier, E. W. K. Young, and D. Beebe, 'Engineers are from PDMS-land, Biologists are from Polystyrenia', *Lab Chip*, vol. 12, no. 7, pp. 1224–1237, Mar. 2012.

[2] W.-Q. Ye, X.-P. Liu, R.-F. Ma, C.-G. Yang, and Z.-R. Xu, 'Open-channel microfluidic chip based on shape memory polymer for controllable liquid transport', *Lab Chip*, vol. 23, no. 8, pp. 2068–2074, Apr. 2023.

[3] Q. Chen, H. Zhai, D. J. Beebe, C. Li, and B. Wang, 'Visualization-enhanced under-oil open microfluidic system for in situ characterization of multi-phase chemical reactions', *Nat Commun*, vol. 15, no. 1, p. 1155, Feb. 2024.

[4] T. E. de Groot, K. S. Veserat, E. Berthier, D. J. Beebe, and A. B. Theberge, 'Surface-tension driven open microfluidic platform for hanging droplet culture', *Lab Chip*, vol. 16, no. 2, pp. 334–344, Jan. 2016.

[5] C. Li *et al.*, 'Under oil open-channel microfluidics empowered by exclusive liquid repellency', *Science Advances*, vol. 6, no. 16, p. eaay9919, Apr. 2020.

[6] G. M. Walker and D. J. Beebe, 'A passive pumping method for microfluidic devices', *Lab Chip*, vol. 2, no. 3, pp. 131–134, Aug. 2002.

[7] C. Ren, S. G. Subramanian, S. Jain, A. L. Hazel, F. Box, and A. Juel, 'Dynamics of evaporating, interconnected droplets', *Soft Matter*, Oct. 2025.

[8] K. Javadi, H. Moezzi-Rafie, V. Goodarzi-Ardakani, A. Javadi, and R. Miller, ‘Flow physics exploration of surface tension driven flows’, *Colloids and Surfaces A: Physicochemical and Engineering Aspects*, vol. 518, pp. 30–45, Apr. 2017.

[9] E. Berthier and D. J. Beebe, ‘Flow rate analysis of a surface tension driven passive micropump’, *Lab on a Chip*, vol. 7, no. 11, pp. 1475–1478, 2007.

[10] J. W. Khor, U. N. Lee, J. Berthier, E. Berthier, and A. B. Theberge, ‘Interfacial Tension Driven Open Droplet Microfluidics’, *Advanced Materials Interfaces*, vol. 10, no. 7, p. 2202234, 2023.

[11] J. J. Lee, J. Berthier, K. E. Kearney, E. Berthier, and A. B. Theberge, ‘Open-Channel Capillary Trees and Capillary Pumping’, *Langmuir*, vol. 36, no. 43, pp. 12795–12803, Nov. 2020.

[12] ‘Flow control in microfluidics: are the workhorse flows adequate?’, *Lab on a Chip*, vol. 8, no. 3, pp. 383–387, 2008.

[13] P. Skafte-Pedersen, D. Sabourin, M. Dufva, and D. Snakenborg, ‘Multi-channel peristaltic pump for microfluidic applications featuring monolithic PDMS inlay’, *Lab Chip*, vol. 9, no. 20, pp. 3003–3006, Oct. 2009.

[14] L. J. Love, J. F. Jansen, T. E. McKnight, Y. Roh, and T. J. Phelps, ‘A magnetocaloric pump for microfluidic applications’, *IEEE Transactions on NanoBioscience*, vol. 3, no. 2, pp. 101–110, June 2004.

[15] X. Ding *et al.*, ‘Surface acoustic wave microfluidics’, *Lab Chip*, vol. 13, no. 18, pp. 3626–3649, Sept. 2013.

[16] X. Luo, L. Yang, and Y. Cui, ‘Micropumps: Mechanisms, fabrication, and biomedical applications’, *Sensors and Actuators A: Physical*, vol. 363, p. 114732, Dec. 2023.

[17] E. J. Walsh *et al.*, ‘Microfluidics with fluid walls’, *Nat Commun*, vol. 8, no. 1, p. 816, Oct. 2017.

[18] C. Soitu, N. Stovall-Kurtz, C. Deroy, A. A. Castrejón-Pita, P. R. Cook, and E. J. Walsh, ‘Jet-Printing Microfluidic Devices on Demand’, *Advanced Science*, vol. 7, no. 23, Art. no. 23, 2020.

[19] F. Nebuloni, P. R. Cook, and E. J. Walsh, ‘Flows in fluid-walled conduits driven by Laplace pressure’, *Journal of Fluid Mechanics*, vol. 969, p. A28, Aug. 2023.

[20] C. Deroy *et al.*, ‘Reconfigurable Microfluidic Circuits for Isolating and Retrieving Cells of Interest’, *ACS Appl. Mater. Interfaces*, vol. 14, no. 22, Art. no. 22, June 2022.

[21] C. Soitu *et al.*, ‘Microfluidic chambers using fluid walls for cell biology’, *PNAS*, vol. 115, no. 26, Art. no. 26, June 2018.

[22] C. Soitu, C. Deroy, A. A. Castrejón-Pita, P. R. Cook, and E. J. Walsh, ‘Using Fluid Walls for Single-Cell Cloning Provides Assurance in Monoclonality’, *SLAS TECHNOLOGY: Translating Life Sciences Innovation*, vol. 25, no. 3, Art. no. 3, June 2020.

[23] A. Prastowo, P. R. Cook, and E. J. Walsh, ‘Biocompatibility of Sessile Drops as Chambers for Cell Culture’, in *2019 2nd International Conference on Bioinformatics, Biotechnology and Biomedical Engineering (BioMIC) - Bioinformatics and Biomedical Engineering*, Sept. 2019, pp. 1–5.

[24] J. Bergfreund, P. Bertsch, and P. Fischer, ‘Adsorption of proteins to fluid interfaces: Role of the hydrophobic subphase’, *Journal of Colloid and Interface Science*, vol. 584, pp. 411–417, Feb. 2021.

[25] C. J. Beverung, C. J. Radke, and H. W. Blanch, ‘Protein adsorption at the oil/water interface: characterization of adsorption kinetics by dynamic interfacial tension measurements’, *Biophysical Chemistry*, vol. 81, no. 1, pp. 59–80, Sept. 1999.

[26] S. G. Baldursdottir, M. S. Fullerton, S. H. Nielsen, and L. Jorgensen, ‘Adsorption of proteins at the oil/water interface—Observation of protein adsorption by interfacial shear stress measurements’, *Colloids and Surfaces B: Biointerfaces*, vol. 79, no. 1, pp. 41–46, Aug. 2010.

[27] W. Lyu *et al.*, ‘Manipulating the Dynamic Adaptivity of a Fluid Interface to Maintain the Multipotency of Mesenchymal Stromal Cells’, *Advanced Healthcare Materials*, vol. 12, no. 24, p. 2300666, 2023.

[28] C. A. MacLeod and C. J. Radke, ‘A growing-drop technique for measuring dynamic interfacial tension’, Lawrence Berkeley National Lab. (LBNL), Berkeley, CA (United States), DOE/BC-94000102, Oct. 1993.

[29] P. A. Rühs, N. Scheuble, E. J. Windhab, and P. Fischer, ‘Protein adsorption and interfacial rheology interfering in dilatational experiment’, *Eur. Phys. J. Spec. Top.*, vol. 222, no. 1, pp. 47–60, May 2013.

[30] A. I. Romoscanu and R. Mezzenga, ‘Cross Linking and Rheological Characterization of Adsorbed Protein Layers at the Oil−Water Interface’, *Langmuir*, vol. 21, no. 21, pp. 9689–9697, Oct. 2005.

[31] F. Nebuloni, Q. B. Do, P. R. Cook, E. J. Walsh, and R. Wade-Martins, ‘A fluid-walled microfluidic platform for human neuron microcircuits and directed axotomy’, *Lab on a Chip*, vol. 24, no. 13, pp. 3252–3264, 2024.

[32] C. Deroy *et al.*, ‘Assaying Macrophage Chemotaxis Using Fluid-Walled Microfluidics’, *Advanced Materials Technologies*, vol. 7, no. 9, p. 2200279, 2022.

[33] C. Deroy, N. Stovall-Kurtz, F. Nebuloni, C. Soitu, P. Cook, and E. Walsh, ‘Predicting flows through microfluidic circuits with fluid walls’, *Microsystems & Nanoengineering*, vol. 7, Dec. 2021.

[34] S. N. Calver, E. A. Gaffney, E. J. Walsh, W. M. Durham, and J. M. Oliver, ‘On the thin-film asymptotics of surface tension driven microfluidics’, *Journal of Fluid Mechanics*, vol. 901, Oct. 2020.

[35] F. Nebuloni, C. Deroy, P. R. Cook, and E. J. Walsh, ‘Stable diffusion gradients in microfluidic conduits bounded by fluid walls’, *Microsyst Nanoeng*, vol. 10, no. 1, p. 79, June 2024.

[36] H. Murasiewicz, A. W. Nienow, M. P. Hanga, K. Coopman, C. J. Hewitt, and A. W. Pacek, ‘Engineering considerations on the use of liquid/liquid two-phase systems as a cell culture platform’, *Journal of Chemical Technology & Biotechnology*, vol. 92, no. 7, pp. 1690–1698, 2017.

[37] B. Zhou, J. T. Tobin, S. Drusch, and S. A. Hogan, ‘Dynamic adsorption and interfacial rheology of whey protein isolate at oil-water interfaces: Effects of protein concentration, pH and heat treatment’, *Food Hydrocolloids*, vol. 116, p. 106640, July 2021.

[38] V. H. Dalvi and P. J. Rossky, ‘Molecular origins of fluorocarbon hydrophobicity’, *Proceedings of the National Academy of Sciences*, vol. 107, no. 31, pp. 13603–13607, Aug. 2010.

[39] S. G. Baldursdottir, M. S. Fullerton, S. H. Nielsen, and L. Jorgensen, ‘Adsorption of proteins at the oil/water interface—Observation of protein adsorption by interfacial shear stress measurements’, *Colloids and Surfaces B: Biointerfaces*, vol. 79, no. 1, pp. 41–46, Aug. 2010.

[40] L.-H. Lin, J. Bergfreund, P. Fischer, and P. Bertsch, ‘Plant protein adsorption at oil–water interfaces: A mapping review using alternate subphase tensiometry’, *Current Opinion in Colloid & Interface Science*, vol. 77, p. 101920, June 2025.

[41] F. Ravera, G. Loglio, and V. I. Kovalchuk, ‘Interfacial dilational rheology by oscillating bubble/drop methods’, *Current Opinion in Colloid & Interface Science*, vol. 15, no. 4, pp. 217–228, Aug. 2010.

[42] E. H. Lucassen-Reynders, J. Benjamins, and V. B. Fainerman, ‘Dilational rheology of protein films adsorbed at fluid interfaces’, *Current Opinion in Colloid & Interface Science*, vol. 15, no. 4, pp. 264–270, Aug. 2010.

[43] J. D. Berry, M. J. Neeson, R. R. Dagastine, D. Y. C. Chan, and R. F. Tabor, ‘Measurement of surface and interfacial tension using pendant drop tensiometry’, *Journal of Colloid and Interface Science*, vol. 454, pp. 226–237, Sept. 2015.

[44] C. J. Beverung, C. J. Radke, and H. W. Blanch, ‘Protein adsorption at the oil/water interface: characterization of adsorption kinetics by dynamic interfacial tension measurements’, *Biophysical Chemistry*, vol. 81, no. 1, pp. 59–80, Sept. 1999.

[45] D. M. Small, L. Wang, and M. A. Mitsche, ‘The adsorption of biological peptides and proteins at the oil/water interface. A potentially important but largely unexplored field’, *Journal of Lipid Research*, vol. 50, pp. S329–S334, Apr. 2009.

[46] B. A. Noskov and A. G. Bykov, 'Dilational surface rheology of polymer solutions', *Russ. Chem. Rev.*, vol. 84, no. 6, p. 634, June 2015.

[47] B.-G. Han and R. M. Glaeser, 'Simple assay for adsorption of proteins to the air–water interface', *Journal of Structural Biology*, vol. 213, no. 4, p. 107798, Dec. 2021.

Supplementary information

Predicting changes in drop heights over time

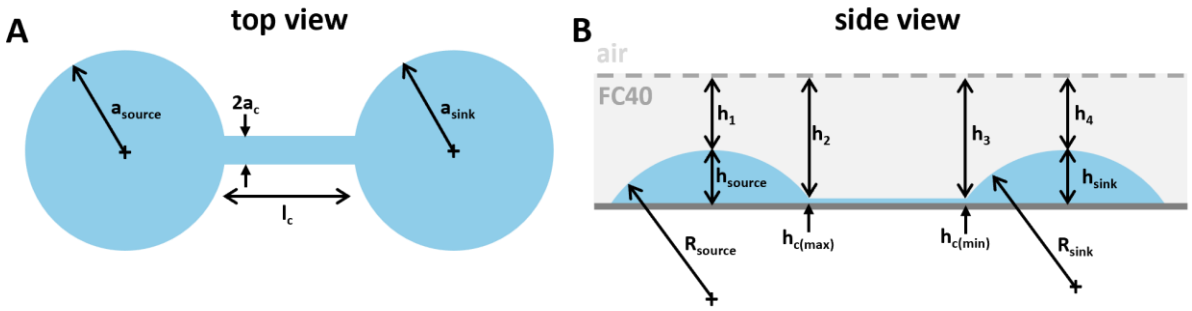

Figure S1. Predicting changes in drop heights over time. (A) Microfluidic dumbbell with fluid walls fabricated from cell-culture medium and immiscible FC40 viewed from above. **(B)** The same dumbbell viewed from side-on.

Pressure P within each drop is the sum of Laplace P_L and hydrostatic pressures P_h:

$$P = P_L + P_{h(medium)} + P_{h(FC40)} \tag{S1}$$

The Laplace pressure is given by $P_L = \gamma\left({}^{1}/_{R_2} + {}^{1}/_{R_2}\right)$ where γ is interfacial tension and $R_{1,2}$ the principal radii of curvature. Drops are sufficiently small to be shaped like spherical caps, therefore orthogonal curvatures are equal, giving $P_L = 2\gamma/R$. Considering the source drop (left), the pressure is given by:

$$P_{source} = \frac{2\gamma_{source}}{R_{source}} + \rho_m g h_{source} + \rho_{FC40} g h_1 \tag{S2}$$

Where $\rho_{m,FC40}$ are the densities of medium and FC40 respectively. The Laplace pressure in the conduit is determined assuming the radius of curvature along its length to be infinite such that $P_{L(con)} = \gamma/R_c$ where R_c is the radius of curvature of the conduit cross section.

Considering the source drop, we assume the pressure at the junction between the drop and conduit to be equal:

$$\frac{2\gamma_{source}}{R_{source}} + \rho_m g h_{source} + \rho_{FC40} g h_1 = \frac{\gamma_{eq}}{R_{c(max)}} + \rho_m g h_{c(max)} + \rho_{FC40} g h_2 \quad \text{(S3)}$$

Here, γ_{eq} is the equilibrium interfacial tension, which is assumed constant in the conduit and distinct from interfacial tensions of the source and sink drops, allowing local changes to be incorporated. We assume the height of the FC40 overlay to be equal to the height of the source drop ($h_1 = 0$) since additional FC40 will act equally everywhere. Using $h_2 = h_{source} - h_{c(max)}$ equation S3 can be rewritten:

$$\frac{2\gamma_{source}}{R_{source}} + \Delta\rho g\left(h_{c(max)} - h_{source}\right) = \frac{\gamma_{eq}}{R_{c(max)}} \quad \text{(S4)}$$

Here $\Delta\rho = \rho_{FC40} - \rho_m$

Using spherical cap geometry, we can express drop radius of curvature in terms of footprint radius, a and height using $R = (a^2 + h^2)/2h$. In the conduit, typically $a \gg h$ allowing for the approximation $R_c = a_c^2/2h_c$ where a_c is the conduit half-width. Substituting into equation S4 gives:

$$\frac{4\gamma_{source} h_{source}}{a_{source}^2 + h_{source}^2} + \Delta\rho g\left(h_{c(max)} - h_{source}\right) = \gamma_{eq}\left(\frac{2h_{c(max)}}{a_c^2}\right) \quad \text{(S5)}$$

This is rearranged to give the height of the conduit at the junction with the source drop:

$$h_{c(max)} = \frac{2\gamma_{eq}}{2\gamma_{eq} - \Delta\rho g a_c^2}\left[\left(\frac{\gamma_{source}}{\gamma_{eq}}\right)\left(\frac{2h_{source}a_c^2}{a_{source}^2 + h_{source}^2}\right) - \left(\frac{\Delta\rho g h_{source}a_c^2}{2\gamma_{eq}}\right)\right] \quad \text{(S6)}$$

The same steps are then applied to the junction between the conduit and the sink drop:

$$P_{sink} = \frac{2\gamma_{sink}}{R_{sink}} + \rho_m g h_{sink} + \rho_{FC40} g h_4 \quad \text{(S7)}$$

Which is considered equal to the pressure in the conduit at the junction:

$$\frac{2\gamma_{sink}}{R_{sink}} + +\rho_m g h_{sink} + \rho_{FC40} g h_4 = \frac{\gamma_{eq}}{R_{c(min)}} + \rho_w g h_{c(min)} + \rho_F g h_3 \quad \text{(S8)}$$

Using existing assumptions, heights can be expressed $h_3 = h_{source} - h_{c(min)}$ and $h_4 = h_{source} - h_{sink}$ giving:

$$\frac{2\gamma_{sink}}{R_{sink}} + \Delta\rho g(h_0 - h_{sink}) = \frac{\gamma_{eq}}{R_{c(min)}} \quad \text{(S9)}$$

Using spherical cap geometry this becomes:

$$\frac{4\gamma_{sink}h_{sink}}{a_{sink}^2 + h_{sink}^2} + \Delta\rho g\left(h_{c(min)} - h_{sink}\right) = \gamma_{eq}\left(\frac{2h_{c(min)}}{a_c^2}\right) \quad \text{(S10)}$$

Rearranging for the height of the conduit at the junction with the sink drop:

$$h_{c(min)} = \frac{2\gamma_{eq}}{2\gamma_{eq-}\Delta\rho g a_c^2}\left[\left(\frac{\gamma_{sink}}{\gamma_{eq}}\right)\left(\frac{2h_{sink}a_c^2}{a_{sink}^2 + h_{sink}^2}\right) - \left(\frac{\Delta\rho g h_{sink}a_c^2}{2\gamma_{eq}}\right)\right] \quad \text{(S11)}$$

A previous study by Deroy et al. [33] found that the height of a fluid walled conduit $h_{c(x)}$ varies along its length such that:

$$h_{c(x)}^4 = \frac{26.08 Q \mu a_c x}{\gamma} + h_{c(min)}^4 \tag{S12}$$

Considering total conduit length ($x = l_c$), this is easily rearranged to obtain flow rate in terms of conduit heights at each end:

$$Q = \frac{\gamma}{26.08 \mu a_c l_c} \left(h_{c(max)}^4 - h_{c(min)}^4 \right) \tag{S13}$$

Combining equations S6, S11 and S13 gives flow rate in terms of source and sink drop heights:

$$Q = \frac{\gamma_{eq}}{26.08 \mu a_c l} \left[\left(\frac{2\gamma_{eq}}{2\gamma_{eq} - \Delta\rho g a_c^2} \left[\left(\frac{\gamma_{source}}{\gamma_{eq}} \right) \left(\frac{2 h_{source} a_c^2}{a_{source}^2 + h_{source}^2} \right) - \left(\frac{\Delta\rho g h_{source} a_c^2}{2\gamma_{eq}} \right) \right] \right)^4 - \left(\frac{2\gamma_{eq}}{2\gamma_{eq} - \Delta\rho g a_c^2} \left[\left(\frac{\gamma_{sink}}{\gamma_{eq}} \right) \left(\frac{2 h_{sink} a_c^2}{a_{sink}^2 + h_{sink}^2} \right) - \left(\frac{\Delta\rho g h_{sink} a_c^2}{2\gamma_{eq}} \right) \right] \right)^4 \right] \tag{S14}$$

The flow rate is defined as the rate of change in volume of the source drop:

$$Q = -\frac{dV_{source}}{dt} \tag{S15}$$

Using spherical cap geometry:

$$V_{source} = \frac{\pi}{6} h_{source} (3a_{source}^2 + h_{source}^2) \tag{S16}$$

$$Q = -\frac{\pi}{2} (a_{source}^2 + h_{source}^2) \frac{dh_{source}}{dt} \tag{S17}$$

Equation S17 is equated to equation S14 to give expected rate in change in source drop height:

$$\frac{dh_{source}}{dt} = -\frac{1.2272\gamma_{eq}^5}{\mu\pi a_c l(a_{source}^2 + h_{source}^2)(2\gamma_{eq} - \Delta\rho g a_c^2)^4}\left[\left(\left(\frac{\gamma_{source}}{\gamma_{eq}}\right)\left(\frac{2h_{source}a_c^2}{a_{source}^2 + h_{source}^2}\right) - \left(\frac{\Delta\rho g h_{source}a_c^2}{2\gamma_{eq}}\right)\right)^4 - \left(\left(\frac{\gamma_{sink}}{\gamma_{eq}}\right)\left(\frac{2h_{sink}a_c^2}{a_{sink}^2 + h_{sink}^2}\right) - \left(\frac{\Delta\rho g h_{sink}a_c^2}{2\gamma_{eq}}\right)\right)^4\right] \quad \text{(S19)}$$

This represents the governing equation used to predict changes in drop height over time. However, an additional relationship is required to related $h_{source(t)}$ to $h_{sink(t)}$. This is obtained assuming constant total volume in the system:

$$V_{sink(t)} = V_{T(0)} - V_{source(t)} \quad \text{(S20)}$$

Heights are then obtained using spherical-cap geometry:

$$\frac{\pi}{6}h_{sink(t)}\left(3a_{sink}^2 + h_{sink(t)}^2\right) = V_{T(0)} - \frac{\pi}{6}h_{source(t)}\left(3a_{source}^2 + h_{source(t)}^2\right) \quad \text{(S21)}$$

Equations S19 and S21 are solved numerically in MATLAB using the Forward Euler Method.

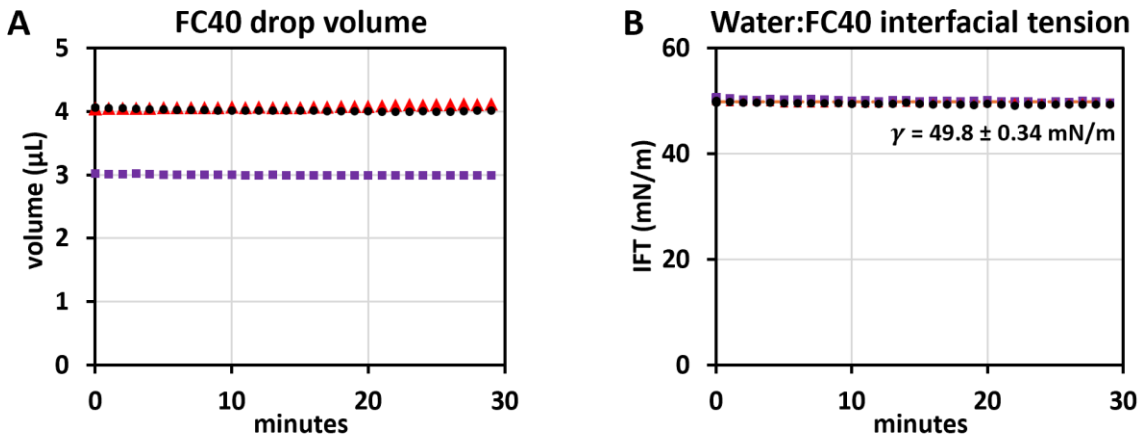

Figure S2. Interfacial tension between FC40 and water. (A) Pendant drops of FC40 were suspended in a pool of deionized water. Two different drop volumes were tested. **(B)** Interfacial tension between FC40 and water. Both drop volumes exhibited the same interfacial tension with the average value shown (n = 3, ± s. d.). Drops were imaged every minute for 30 minutes. Unlike protein-rich medium, there is no decrease in interfacial tension over time.

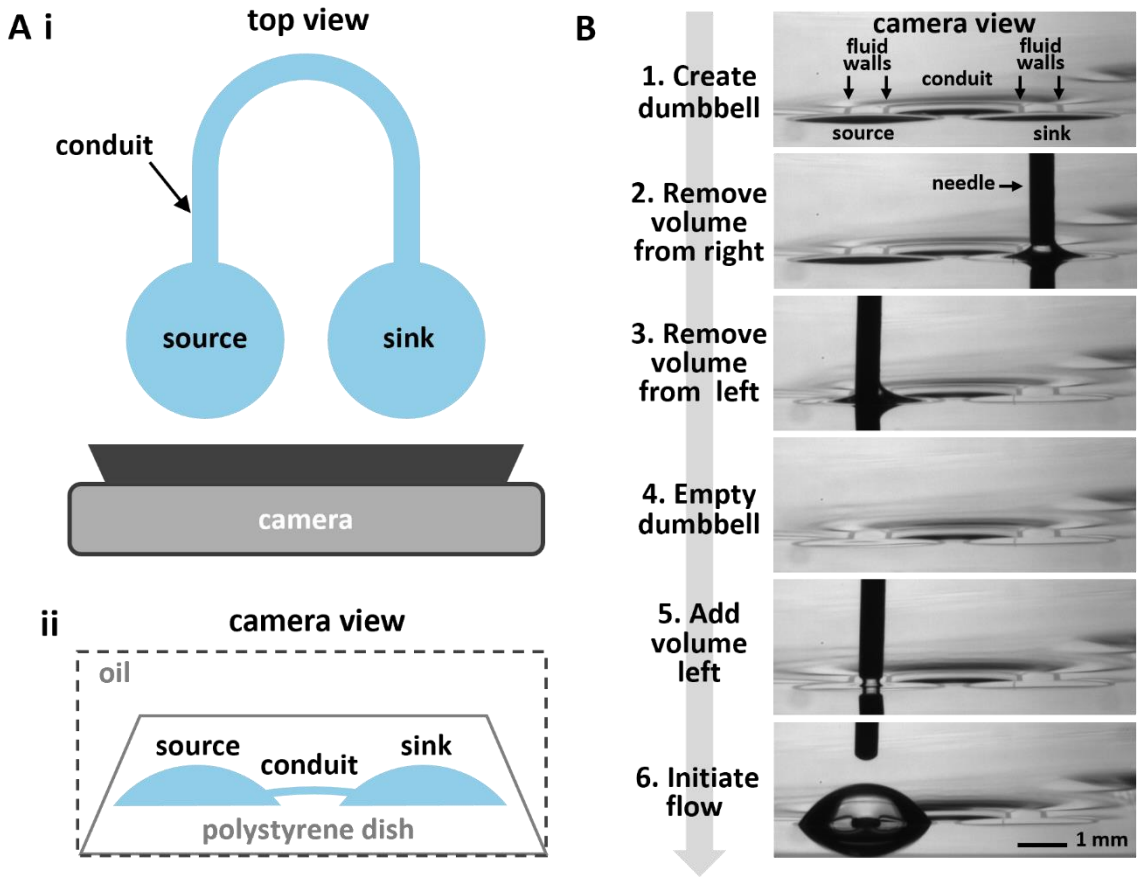

Figure S3. Dumbbell preparation workflow. **(A)** Cartoon illustration of dumbbell view from **(i)** above and **(ii)** viewed through camera. **(B)** Side view of a dumbbell shortly after fabrication. (1) Medium displaced by the micro-jet of FC40 is swept into each drop, causing irregular starting volumes. (2) A dispensing needle is lowered through the overlaid FC40 so that it just touches the FC40-medium interface, and volume is withdrawn from the drop using a syringe pump. (3) The process is repeated to remove volume from both drops. (4) Residual medium has been withdrawn, leaving a near-empty dumbbell. (5) The dispensing needle is once again lowered through the FC40 so that it just touches the FC40-medium interface. (6) Medium is infused into the left (source) drop to initiate flow.

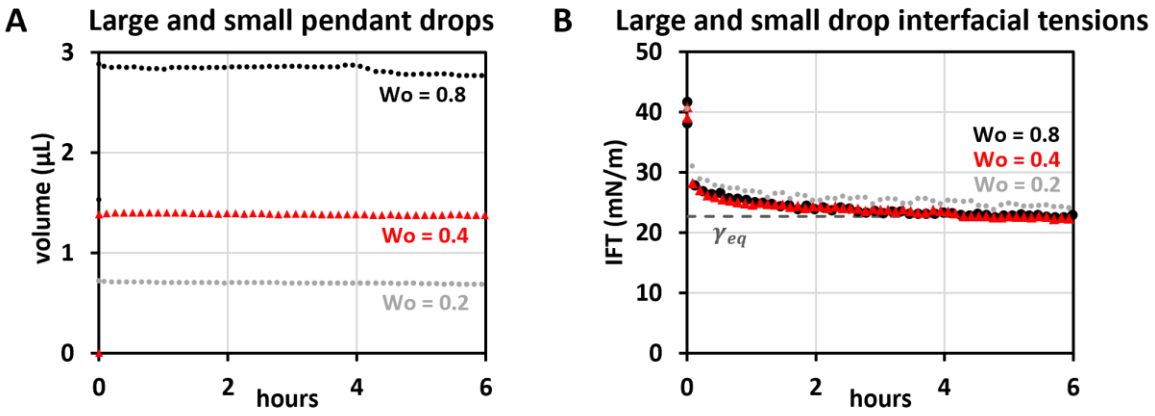

Figure S4. Volume limits for dynamic pendant drop interfacial tensiometry. (A) Three pendant drop volumes were tested, representing Worthington numbers of 0.8, 0.4 and 0.2 (corresponding volumes of 2.85 µL, 1.43 µL and 0.71 µL respectively). **(B)** Both larger drops (0.8 and 0.4) exhibited a similar decrease in interfacial tension over time, which approached the equilibrium value. The smallest drop (0.2) equilibrated to an interfacial tension slightly higher than the equilibrium value (24.8 vs 22.7 mN/m). Therefore, pendant drops volumes were kept between Worthington numbers of 0.8 and 0.4.

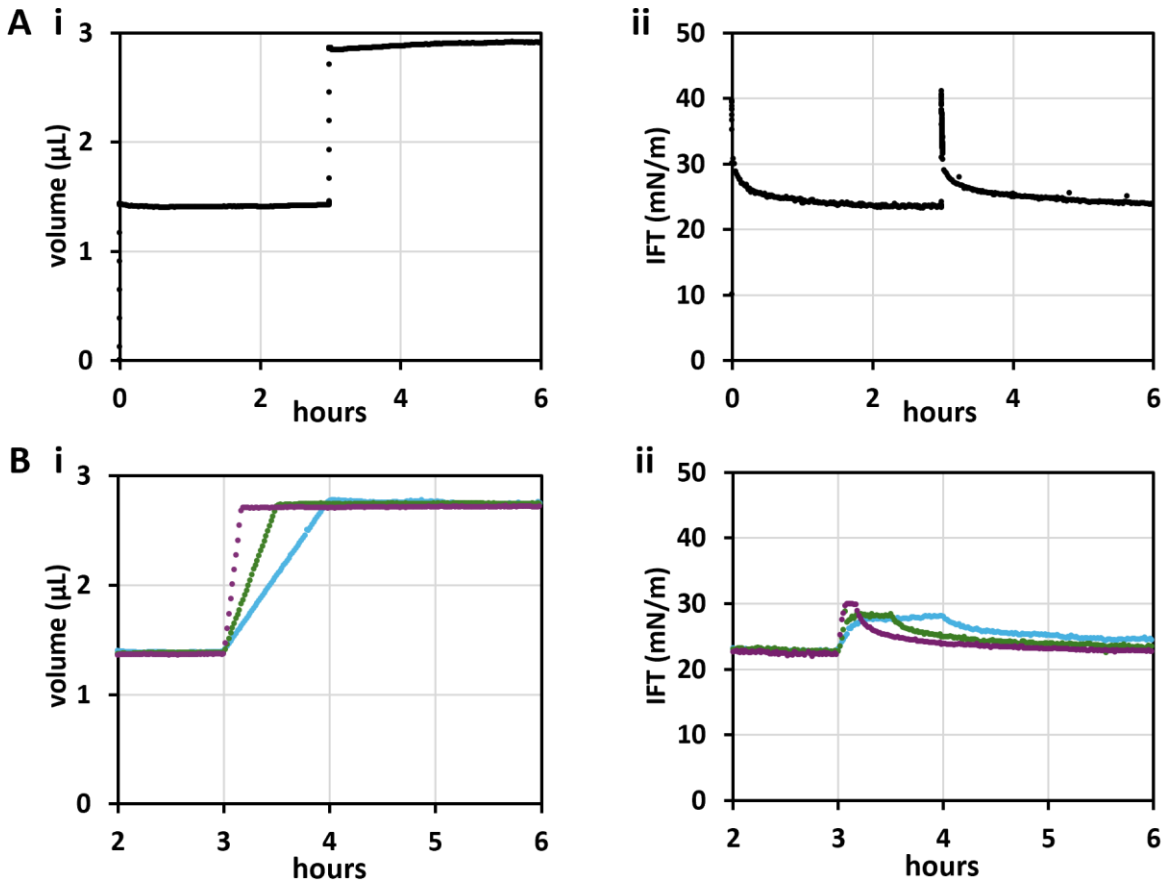

Figure S5. Relaxation of expanding pendant drops to equilibrium. (A) Rapid expansion. **(i)** A 1.43 µL pendant drop of FC40 (Wo ≈ 0.4) in a cuvette of medium supplemented with 10% serum was held static for 3 hours to allow interfacial tension to reach equilibrium. Volume was then increased to 2.85 µL over ~ 0.5 seconds. During initial equilibration, images were acquired every minute. Shortly before and during expansion, imaging frequency was increased to every 0.1 seconds for 1 minute, then returned to 1-minute intervals for the following 3 hours. **(ii)** A rapid increase in volume caused a sharp rise in interfacial tension, which relaxed back to equilibrium following a trajectory similar to the initial static drop. **(B)** Changing expansion rate. **(i)** Pendant drop volume was increased over the same range as (A), over 10 minutes, 30 minutes and 1 hour. **(ii)** The magnitude of the interfacial tension increase scaled with the rate of expansion, plateaued, and then relaxed to equilibrium once expansion ceased. All relaxion curves followed a similar trend regardless of expansion rate.

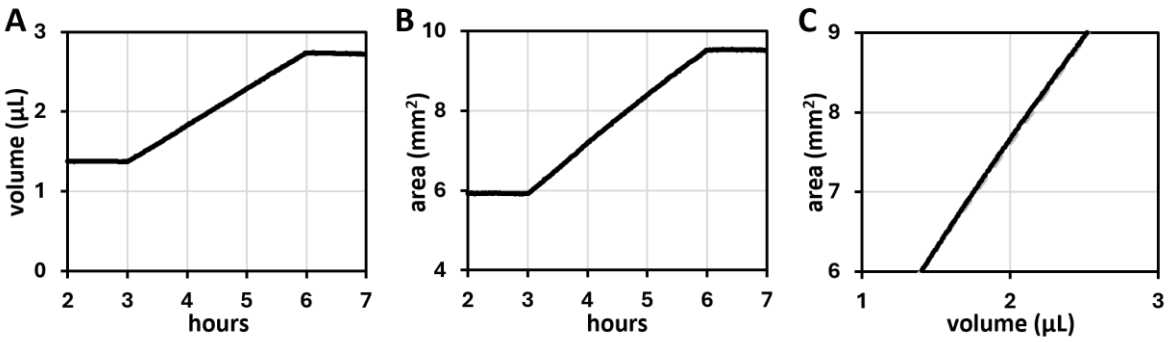

Figure S6. Linear relationship between pendant drop volume and area. (A) Drop volume was increased from ~ 1.43 µL to ~ 2.85 µL over 3 hours. **(B)** Pendant drop area increased with volume. **(C)** Plotting pendant drop area against volume within the working range yielded an approximately linear relationship, $A \approx 2.64V + 2.32$, where A is in mm^2 and V in µL (R-square = 0.99942, linear fit performed in MATLAB). This enabled control of interfacial area changes via prescribed volume changes.

A

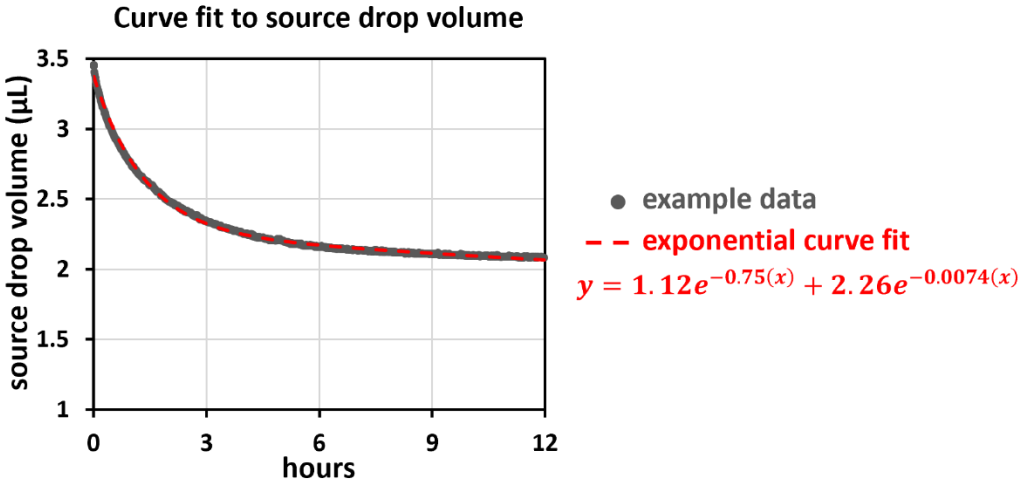

B

Fit equation:		$a \cdot e^{-b} + c \cdot e^{-d}$				
Conduit width (mm)	**Rep**	**a**	**b**	**c**	**d**	**R-Square**
0.36	1	0.8643	0.1809	2.5336	0.0031	0.9966
	2	1.1548	0.2067	2.5236	0.0027	0.9973
	3	0.9124	0.1730	2.8275	0.0039	0.9866
0.46	1	1.2536	0.8111	2.44531	0.0056	0.9984
	2	1.1184	0.7502	2.2572	0.0074	0.9968
	3	0.9589	0.9556	2.1099	0.0065	0.9961
0.65	1	1.6872	13.1594	1.8843	0.0023	0.9967
	2	1.2190	8.5868	1.4756	0.0018	0.9947
	3	1.4004	11.6064	1.5050	0.0024	0.9952

Figure S7. Exponential curve fit to change in source drop volume over time. (A) Example curve fit to change in source drop volume over time. In each experiment, a two-term exponential curve fit was used to smooth data and hence estimate flow rate in a dumbbell. **(B)** Table of curve fit parameter values found in each experiment for varying conduit widths. Curve fits were preformed using MATLAB.

Change in interfacial tension as pendant drop area decreases: comparing two drop sizes

To assess the validity of the linear approximation between the decrease in interfacial tension and reduction of interfacial area across varying drop sizes, results were compared to unpublished data independently obtained by another research student. Here, a 'small' drop of FC40 was suspended on a smaller 0.4 mm diameter needle in a pool of the same medium (relative to the 'large' drop shown in **Figure 5** of the main text). Initially, 1.8 µL was infused, and 1.3 µL withdrawn over 30 mins. Next, 1.3 µL was quickly re-infused (20 µL/min) and the process repeated cyclically 6 times per experiment.

Data for the large drop was first compared to a single cycle which aligned with the ratio $\gamma(A)/\gamma_{eq}$ at $\Delta A/A_0$ of - 0.18 obtained independently across experiments. There was excellent agreement (94%) in gradient across experiments for varying drop sizes (**Figure S8Ai**). Next, averaged data was compared across cycles (omitting the first) for two independent small-drop experiments against the original large drop (**Figure S8Aii**). In each case, the gradient aligned with that of the larger drop, within 97% for small drop 1 and 88% for small drop 2. There was excellent alignment between average y intercept for large and small drop 2 (99%) and an offset in small drop 1 of 11%. The average gradient across both experiments, compared to that of the larger drop was within 95% (both small drop experiments averaged as test 2 in **Figure S8B**). In all cases, linear curve fits were obtained using MATLAB, omitting data points below $\Delta A/A_0$ of 0.02. Together, this agreement across drop sizes supports the robustness of the linear approximation between drop interfacial tension and area decrease.

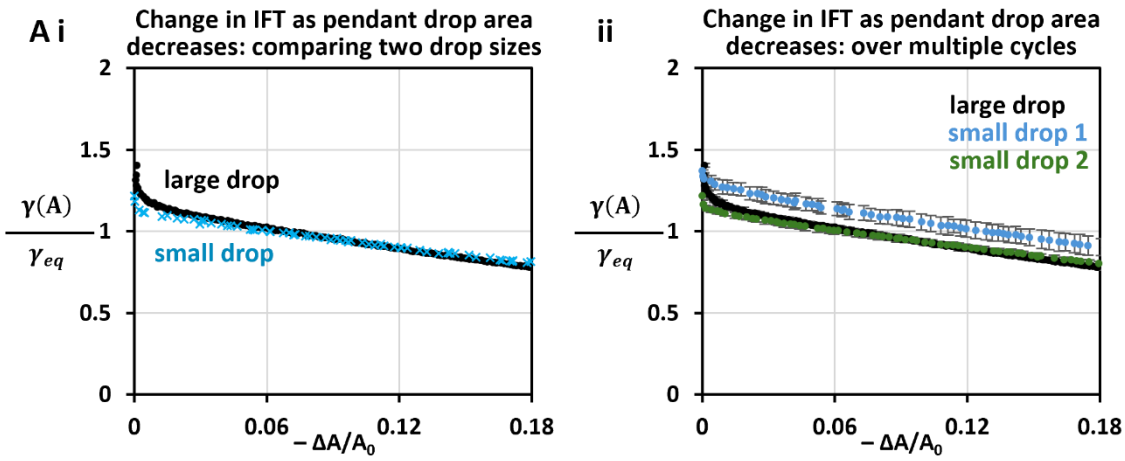

B

Test	Needle OD (mm)	Reps	Cycles	Start volume (µL)	End volume (µL)	Remove time (h)	Linear approximation	
							Gradient	Y intercept
1	0.51	3	1	2.85	1.43	3.0	1.99	1.13
2	0.40	2	6	1.80	0.50	0.5	1.90	1.19

Figure S8. Reducing interfacial area causes a linear reduction in interfacial tension for two different pendant drop sizes. (A) Comparison between a large and small pendant drop**. (i)** Both drop sizes exhibited similar reduction in interfacial tension as area decreased. **(ii**) Small drops were infused quickly and volume withdrawn cyclically in each experiment (n = 6 cycles, ± s. d., large drop n = 3 ± s. d.). In each case, there was strong agreement between gradient of small and large drops, with some offset observed in small drop 1. **(B)** Table of values for each test (test 2 representing the average of small drops 1 and 2). The gradient of the linear approximation relating reduction in interfacial area to interfacial tension shows strong agreement with that found in the original larger drop.

Statement of Authorship for joint/multi-authored papers for PGR thesis

To appear at the end of each thesis chapter submitted as an article/paper

The statement shall describe the candidate's and co-authors' independent research contributions in the thesis publications. For each publication there should exist a complete statement that is to be filled out and signed by the candidate and supervisor **(only required where there isn't already a statement of contribution within the paper itself).**

Title of Paper	Dynamic interfacial tension effects in microfluidics with fluid walls
Publication Status	Unpublished and unsubmitted work written in a manuscript style
Publication Details	Joseph A.E. Morgan, Federico Nebuloni, Peter R. Cook, Alfonso A. Castrejón-Pita, Edmond J. Walsh

Student Confirmation

Student Name	Joseph Morgan		
Contribution to the Paper	Lead Author Designed experiments in discussion with co-authors, performed experiments, collected and analysed data, prepared figures and manuscript. Comparative data in supplementary Figure S8 was provided by FN.		
Signature 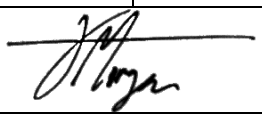		Date	07/01/2026

Supervisor Confirmation

By signing the Statement of Authorship, you are certifying that the candidate made a substantial contribution to the publication, and that the description described above is accurate.

Supervisor name and title: Prof. Edmond J. Walsh		
Supervisor comments		
Signature Ed Walsh	Date	7th Jan 2026

This completed form should be included in the thesis, at the end of the relevant chapter.

Chapter 6: Discussion

Discussion

This thesis advances the understanding of the static and dynamic behaviour of microfluidics with fluid walls and demonstrates how these systems enable new approaches to studying single cells. The work provides new experimental and analytical tools for both biologists and engineers, supporting future implementation and offering a deeper appreciation for the underlying physical behaviour of these systems.

This thesis begins by developing a static microfluidic system – a sessile drop – and characterises the physical behaviour of fluid drops on polystyrene. **Chapter 3** demonstrates how pinned drops with low contact angles provide excellent optical clarity, enabling reliable verification of monoclonality within microtiter wells and overcoming the common problem of detecting single cells at the well periphery. Several approaches have been developed to address this challenge. For example, inkjet-style single-cell printing systems use automated imaging to identify single cells before confining them to discrete droplets that are dispensed into wells [77], [78]. However, this does not fully eliminate the need for in-well verification, as the presence of exactly one cell per well cannot be guaranteed [79]. An alternative method is to deposit a drop within a well followed by z-stack imaging to identify single-cell occupancy [80], but such systems are costly and technically complex. In contrast, the use of flat drops provides a simpler and more accessible approach for in-well verification of monoclonality, suited to routine laboratory applications. The biocompatibility of this workflow is demonstrated through high cloning efficiencies across multiple cell types, including induced pluripotent stem cells. Although this method provides a robust means of confirming the presence of a single cell, the overall yield remains limited by Poisson statistics. Several strategies could be pursued to overcome this limitation. For example, cell suspension could be reinfused into wells that initially receive no cells, while wells containing multiple could be reset by withdrawing volume followed by reinfusion. Alternatively, methods could be developed to identify single cells

upstream, prior to infusion, within the dispensing system itself. For example, automated single-cell printing systems verify the presence of a single cell prior to deposition within an inkjet-like dispensing nozzle, enabling plating efficiencies exceeding 95% [81], [82]. Identification of single cells in flat drops would be greatly facilitated by integrating automated imaging and cell-detection, which would reduce operator burden, shorten workflows, and increase the feasibility of iterative infusions and withdrawals to improve the yield of single cells.

Going beyond a static sessile drop, this thesis next considers two drops connected by a thin fluid conduit, forming a dumbbell shape. This created a dynamic system since modulating the volume in each drop alters local Laplace pressure and drives flow between them. A similar configuration has previously been used to study macrophage migration [13]. This work pioneered the use of microfluidics with fluid walls for studying cell migration and demonstrated that modulating chamber volumes – and hence internal pressure – can be used to control flow between chambers enabling spatial confinement of cells and chemoattractants which diffuse through conduits generating stable chemical gradients. These principles have also been used to support the long-term culture of neurons [14]. In this case, spatial separation of axons and somas was achieved within a similar dumbbell-shaped arrangement, while the reconfigurability of fluid walls was leveraged to perform directed axotomy by ‘cutting’ the conduit. The work presented in **Chapter 4** builds upon these principles to investigate the application of microfluidics with fluid walls to study cancer cell migration.

Cancer cell migration is a key process underlying metastasis. A wide range of assays have been developed to study this behaviour, with microfluidic platforms proving useful for monitoring directed migration within microchannels [83]. These approaches enable precise control over cellular microenvironments and have, in many cases, revealed distinct migratory subpopulations alongside non-migratory cells [84], [85], [86]. While some platforms allow isolation and retrieval of migratory cells, they are often limited to binary classification (migratory vs non-migratory) as cells are typically pooled during retrieval [84], [85], [87].

Chapter 4 extends this capability through the application of microfluidics with fluid walls. By exploiting their reconfigurability, single migratory cells can be isolated and retrieved, enabling comparison between individual distinct migratory phenotypes (e.g. differing morphologies) and establishing a framework for analysing heterogeneity within migratory subpopulations. It also represents a step toward high-throughput fluid-walled assays, with up to 80 dumbbells fabricated within a standard Petri dish.

A notable feature of microfluidic dumbbells with fluid walls is the ability to generate very shallow conduits (< 5 μm), smaller than some adherent PC3 cells [88]. Similar geometries have been reported in comparable systems employing silicone oil-medium interfaces [66] where deformation of the interface during cell transit was observed. In that context, migrating neutrophils experienced compressive forces as they traversed the channel, mimicking aspects of migration through confined tissue environments and eliciting distinct migratory behaviours. A comparable interaction is likely to occur in the present system with migrating PC3 cells, where deformation of the interface may impose mechanical constraints. This could be advantageous in creating a more physiologically relevant model, as confined migration through dense tissue is a key step in metastasis [89]. However, further work is required to quantify the extent of interfacial deformation and to determine its influence on migratory behaviour, including potential effects on relevant processes such as the epithelial-mesenchymal transition.

The strong optical properties of fluid walls enabled quantification of migration at single-cell resolution and supported the use of machine-learning-based analysis of morphology, revealing distinct migratory subpopulations. Importantly, this work establishes methods to isolate and retrieve the most migratory cells, expand them to clonal cultures, and obtain comparative non-migratory clones, providing a framework for downstream analyses. These advances open numerous future directions, including single-cell sequencing of migratory subpopulations, drug-response migration assays, and co-culture studies using cancer cells within dumbbells with fluid walls.

While investigating the dynamic behaviour of dumbbells with fluid walls, a curious phenomenon was observed. Increasing the volume of one chamber relative to the other initiated flow between them; however, when flow ceased, the chambers did not equilibrate to the same height despite identical footprint geometries. Adsorption of proteins to oil-aqueous interfaces is known to reduce interfacial tension [90], [91]. It was therefore hypothesised that the observed height mismatch arose from spatial variations in interfacial tension caused by differences in protein adsorption as interfaces locally expand and contract during flow. Dynamic interfacial tension was investigated using pendant-drop tensiometry, which revealed an approximately linear relationship between decreasing interfacial area and tension. Incorporating this relationship into a predictive model for dumbbell behaviour enabled accurate prediction of changes in drop height, within 5% for dumbbells with narrow conduits. These results demonstrate that dynamic changes in interfacial tension play a critical role in governing flow within fluid walls, and the predictive model provides a practical tool for anticipating dumbbell behaviour and equilibration times which previously relied on empirical measurement. Future work is required to determine the extent to which these findings can be generalised to other oil-medium interfaces or to medium containing different serum concentrations. Advancing understanding of protein adsorption to expanding and contracting interfaces may also create opportunities to use fluid walls as model platforms for biological processes in which interfacial dynamics are central, such as the adsorption of pulmonary surfactants within alveoli in the lung [92].

Throughout this thesis, key limitations are discussed within each research chapter. However, there are also more general limitations of microfluidics with fluid walls which warrant consideration. First, a known limitation of PDMS-based microfluidic systems is the absorption of small molecules from culture media, which can restrict their suitability for sensitive biological applications [4]. In systems with fluid walls, amphiphilic molecules are adsorbed to the oil-medium interface, suggesting that similar sequestration effects may occur. Further investigation is required to quantify these effects and to determine whether established

mitigation strategies (for example, pre-saturation using PEG [93]) can also be applied to fluid walls. Second, dumbbell chambers are connected by a thin fluid conduit whose width is typically constrained to ≥ 100 μm. Narrower conduits are prone to evaporation, limiting the accessible range of conduit widths achievable using fluid walls. Third, the work presented here is restricted to two-dimensional cell cultures. There is growing demand for three-dimensional biological models, such as spheroids or organoids, which are yet to be integrated within a fluid-walled microfluidic platform, representing an important avenue for future research. Fourth, perfluorocarbon oils are classified as 'forever chemicals' and face increasing global regulatory scrutiny [94]. Developing strategies to reduce consumption and enable recycling of FC40 used in fabrication of fluid walls will be important for the long-term sustainability of this technology. In addition, a key assumption underlying fluid walls is the bio-inert nature of FC40. It is widely regarded as bio-inert due to its chemical stability and established use (or of closely-related oils) in diverse biological applications, including blood substitution [95], liquid ventilation in preterm neonates [96], and the culture of a wide range of cell types that exhibit normal cell growth when overlaid with FC40 [12]. However, more rigorous validation – such as genomic or transcriptomic comparisons between cells cultured under FC40 and standard conditions – would be valuable to confirm its bio-inertness.

Finally, although this thesis advances the understanding of the behaviour of fluid-walled systems and provides practical tools for their application, the design and operation of such systems requires technical expertise and a sophisticated understanding of the underlying physical mechanisms. This may present a barrier to adoption by biologists; however, continued development is expected to improve accessibility and facilitate wider uptake of fluid-walled microfluidics in biological research.

Conclusions

The key contributions of this thesis are summarised below, structured around the objectives defined in **Chapter 1.**

Chapter 2 presents a literature review outlining the emergence and evolution of microfluidic technologies. It highlights key challenges and limitations of traditional microfluidic systems, particularly with respect to single-cell manipulation, and describes how these limitations motivated the development of microfluidics with fluid walls, which addresses many of the constraints associated with conventional microfluidic platforms.

Chapter 3 investigates a static microfluidic system and presents a method for using sessile drops with low contact angles to verify monoclonality within a single-cell cloning workflow. This approach was extensively validated using adhesion and suspension cells, including iPSCs, on treated and untreated polystyrene surfaces achieving average cloning efficiencies between 62% - 78%. Furthermore, ~ 87% of adherent HEK colonies formed in the optically clear well centre after imaging in drops, away from dark regions at the periphery. A range of matrix coatings were used to create flat drops for imaging iPSCs, all of which supported high cloning efficiencies and cells were shown to retain their pluripotency after cloning. Using drops of matrix coatings reduced reagent consumption by 75% compared to normal coating. This approach was incorporated into a CRISPR gene-editing workflow where edited iPSCs were imaged in flat drops of Biolaminin coating and achieved 75% cloning efficiency. This technique overcomes the long-standing challenge of identifying single cells at the periphery of microtiter wells and provides a simple, easily integrated method for confirming monoclonality.

Chapter 4 advances to a dynamic system and presents the first application of microfluidics with fluid walls to study cancer cell migration. A dumbbell-shaped arrangement was used to confine PC3 cancer cells and chemoattractant (medium supplemented with 20% FBS) to separate chambers, after which cell migration was monitored over 3 days and

quantified. This approach revealed heterogenous subpopulations of migratory cancer cells, ranging from small round cells to larger, irregularly-shaped phenotypes. Successful migration through the dumbbell was a rare occurrence, with a dish containing 36 dumbbells yielding on average 3 migratory cells, representing 0.03% of the total cell population averaged across 7 independent replicates. Fluid walls were reconfigured to isolate the migrated cell which was picked and transferred to a microtiter well. Single migrated cells proliferated successfully in medium supplemented with 30% FBS, yielding 12% cloning efficiency. A complementary method was developed to obtain a single non-migratory cell, in which non-migrated cells were extracted from dumbbells and distributed across a grid of micro-chambers with fluid walls, and an optimised method used to pick single cells from chambers with > 97% picking efficiency. The excellent optical properties of fluid walls enabled use of machine learning tools to evaluate cell morphology during migration. This indicated two subgroups: small fast-moving cells, and larger slow-moving cells. Of the 58 cells tracked, the majority fell within the first group, with 11 cells in the second.

Chapter 5 examines the influence of dynamic changes in interfacial tension on flow within fluid walls. As chambers expand and contract during flow, spatial and temporal variations in interfacial tension arise. Consequently, dumbbell chambers may equilibrate with different heights, despite equal footprints. Dynamic interfacial tension measurements between a pendant drop of FC40 and cell culture medium revealed an approximately linear relationship between decreasing interfacial area and interfacial tension. Furthermore, if expansion was sufficiently slow, interfacial tension remained approximately constant. This was used to develop a predictive model for changes in dumbbell chamber heights and compared against microfluidic experiments for varying conduit widths, showing agreement within 5%. Equilibration time between drops was defined as the duration required for flow to fall below 10% if the initial maximum value. The accuracy of predicted equilibration times improved with decreasing conduit width and increasing timescales, achieving agreement within 7% for the narrowest conduit condition.

Advancing the adoption of microfluidic technologies by biologists remains a central challenge for engineers. Microfluidics with fluid walls addresses many of the limitations that have hindered uptake of conventional microfluidic systems for biological applications. Although significant scope for further development remains, this thesis represents a significant step forward in improving understanding the physical behaviour of microfluidic systems with fluid walls while broadening their application in studying single cells. Together, the finding presented here aim to encourage wider adoption of microfluidics with fluid walls by biologists and to foster closer alignment between engineers and biologists in the design of impactful single-cell research platforms.

Future works

Sessile drops under FC40 as monoclonal cell culture vessels

The work presented in Chapter 3 demonstrates how sessile drops with low contact angles can serve as temporary imaging vessels to verify monoclonality within microtiter wells. In the current implementation, cells are held within drops for a few minutes before the well is flooded with culture medium. A natural extension of this work would be to develop sessile drops not merely as temporary containment tools, but as miniature monoclonal culture vessels within microtiter wells. Such an approach could substantially reduce medium used throughout a cloning workflow – a benefit that is particularly relevant to culturing induced pluripotent stem cells, where expensive growth factors are often required.

A proposed workflow is illustrated in **Figure 1**: the initial steps mirror those described in Chapter 3 for verification of monoclonality, but instead of flooding with medium, the drop would be overlaid with FC40. Additional medium could then be infused into the drop (increasing the contact angle beyond 90^{o} if necessary) to sustain cell growth.

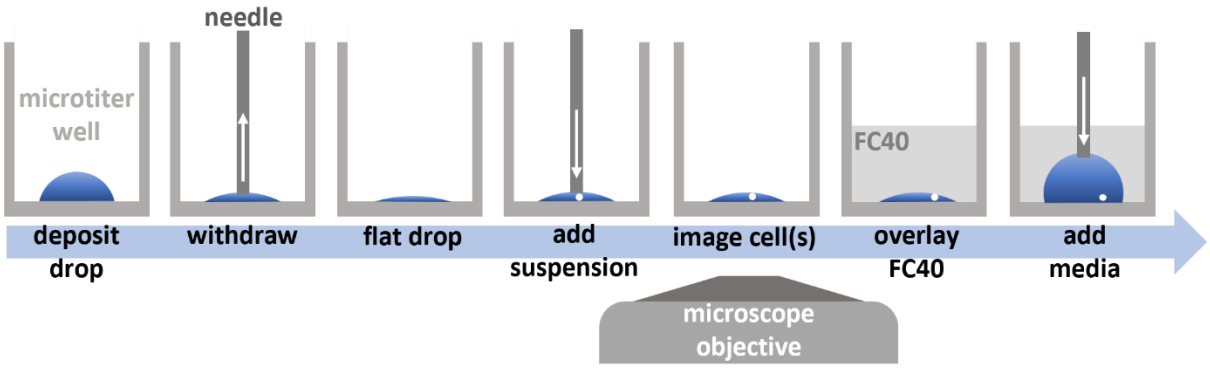

Figure 1. Workflow for using sessile drops as monoclonal cell culture vessels. A sessile drop is deposited centrally within a microtiter well, volume withdrawn to reduce the contact angle, and a small volume of cell suspension infused into the flat drop. The drop is imaged to verify monoclonality and overlaid with FC40. Medium can be infused into the submerged drop to sustain cell growth.

Single-cell sequencing and in vivo studies of migratory cancer cells

Chapter 4 demonstrates how microfluidics with fluid walls can be used to identify, isolate, and retrieve the most migratory cancer cells from a heterogenous population. It also presents a method to obtain a single non-migratory cell and hence establish a comparative framework. This capability creates many opportunities for downstream comparative analyses between migratory and non-migratory subpopulations. A clear potential next step would be to perform single-cell genomic or transcriptomic sequencing, which could reveal genetic or transcriptional differences underlying migratory behaviour. Such insights would deepen understanding of metastatic processes and guide future studies.

Beyond sequencing, further studies could involve generating clonal cultures from the isolated migratory cells, which could then be replated into dumbbells to assess whether enhanced migratory behaviour represents a stable, heritable phenotype. Furthermore, co-culture with other cell types known to influence migratory behaviour – for example, fibroblasts or macrophages – could enhance the physiological relevance of the model by better recapitulating key aspects of the metastatic microenvironment.

Cells from both migratory and non-migratory subpopulations could also be evaluated in *in vivo* models. Implanting cells from each subpopulation into mice would help establish whether the enhanced migration observed *in vitro* correlates with increased metastatic potential, thereby strengthening the link between single-cell migratory behaviour and disease progression. However, the necessity of such experiments should be carefully considered given the ethical and financial burdens associated with animal models. *In vivo* studies should only be pursued where *in vitro* or alternative approaches cannot provide sufficient insight.

Dynamic interfacial tension of varying serum concentrations and oil overlays

This thesis has demonstrated that dynamic changes in interfacial tension at the FC40-medium interface play a central role in governing flow within microfluidic systems with fluid walls. The work in Chapter 5 focused specifically on medium supplemented with 10% serum, a widely used condition in cell culture. However, many biological workflows employ different serum concentrations; for example, the migration assay in Chapter 4 operates between 20% and 0.5% serum. Future research could therefore be to quantify dynamic interfacial tension changes at the FC40-medium interface across a range of serum concentrations. Such measurements would determine to what extent the linear relationship between interfacial-tension reduction and interfacial-area contraction is conserved, and how the relationship might vary with serum content.

In addition, further studies could extend the dynamic interfacial tension analyses presented here beyond the FC40-medium interface, used in the fabrication of fluid walls. As the field of open microfluidics continues to grow, an increasing number of systems employ alternative oil-aqueous interfaces – for example silicone oils or hydrocarbons – to achieve an open system and hence interfacial areas in such systems will change in response to the addition or withdrawal of fluid [7], [97], [98]. It would therefore be valuable to determine whether comparable relationships between interfacial tension and interfacial area hold for these alternative oil-medium combinations, broadening the general applicability of the findings presented here.

References

[1] S. Battat, D. A. Weitz, and G. M. Whitesides, ‘An outlook on microfluidics: the promise and the challenge’, *Lab Chip*, vol. 22, no. 3, pp. 530–536, Feb. 2022.

[2] A. Gross, J. Schoendube, S. Zimmermann, M. Steeb, R. Zengerle, and P. Koltay, ‘Technologies for Single-Cell Isolation’, *Int J Mol Sci*, vol. 16, no. 8, pp. 16897–16919, July 2015.

[3] C. Wang *et al.*, ‘Microfluidic Biochips for Single-Cell Isolation and Single-Cell Analysis of Multiomics and Exosomes’, *Adv Sci (Weinh)*, vol. 11, no. 28, p. 2401263, May 2024.

[4] K. J. Regehr *et al.*, ‘Biological implications of polydimethylsiloxane-based microfluidic cell culture’, *Lab Chip*, vol. 9, no. 15, pp. 2132–2139, Aug. 2009.

[5] E. Berthier, E. W. K. Young, and D. Beebe, ‘Engineers are from PDMS-land, Biologists are from Polystyrenia’, *Lab Chip*, vol. 12, no. 7, Art. no. 7, Mar. 2012.

[6] E. Berthier, A. M. Dostie, U. N. Lee, J. Berthier, and A. B. Theberge, ‘Open Microfluidic Capillary Systems’, *Anal. Chem.*, vol. 91, no. 14, Art. no. 14, July 2019.

[7] Q. Chen, H. Zhai, D. J. Beebe, C. Li, and B. Wang, ‘Visualization-enhanced under-oil open microfluidic system for in situ characterization of multi-phase chemical reactions’, *Nat Commun*, vol. 15, no. 1, p. 1155, Feb. 2024.

[8] A. Yrjänäinen *et al.*, ‘Barrier-free, open-top microfluidic chip for generating two distinct, interconnected 3D microvascular networks’, *Sci Rep*, vol. 14, no. 1, p. 22916, Oct. 2024.

[9] J. H. Schrope *et al.*, ‘Confinement by Liquid-Liquid Interface Replicates In Vivo Neutrophil Deformations and Elicits Bleb-Based Migration’, *Advanced Science*, vol. 12, no. 21, p. 2414024, 2025.

[10] E. J. Walsh *et al.*, ‘Microfluidics with fluid walls’, *Nat Commun*, vol. 8, no. 1, p. 816, Oct. 2017.

[11] C. Deroy *et al.*, ‘Reconfigurable Microfluidic Circuits for Isolating and Retrieving Cells of Interest’, *ACS Appl. Mater. Interfaces*, vol. 14, no. 22, Art. no. 22, June 2022.

[12] C. Soitu *et al.*, ‘Microfluidic chambers using fluid walls for cell biology’, *PNAS*, vol. 115, no. 26, Art. no. 26, June 2018.

[13] C. Deroy *et al.*, ‘Assaying Macrophage Chemotaxis Using Fluid-Walled Microfluidics’, *Advanced Materials Technologies*, vol. 7, no. 9, p. 2200279, 2022.

[14] F. Nebuloni, Q. B. Do, P. R. Cook, E. J. Walsh, and R. Wade-Martins, ‘A fluid-walled microfluidic platform for human neuron microcircuits and directed axotomy’, *Lab on a Chip*, vol. 24, no. 13, pp. 3252–3264, 2024.

[15] C. Deroy, N. Stovall-Kurtz, F. Nebuloni, C. Soitu, P. R. Cook, and E. J. Walsh, ‘Predicting flows through microfluidic circuits with fluid walls’, *Microsyst Nanoeng*, vol. 7, no. 1, Art. no. 1, Nov. 2021.

[16] F. Nebuloni, P. R. Cook, and E. J. Walsh, ‘Flows in fluid-walled conduits driven by Laplace pressure’, *Journal of Fluid Mechanics*, vol. 969, p. A28, Aug. 2023.

[17] P. L. Chen, R. S. Muller, and A. P. Andrews, ‘Integrated silicon pi-fet accelerometer with proof mass’, *Sensors and Actuators*, vol. 5, no. 2, Art. no. 2, Feb. 1984.

[18] K. E. Petersen, A. Shartel, and N. F. Raley, ‘Micromechanical accelerometer integrated with MOS detection circuitry’, *IEEE Transactions on Electron Devices*, vol. 29, no. 1, Art. no. 1, Jan. 1982.

[19] B. E. Rapp, ‘Chapter 1 - Introduction’, in *Microfluidics: Modelling, Mechanics and Mathematics*, B. E. Rapp, Ed., in Micro and Nano Technologies. , Oxford: Elsevier, 2017, pp. 3–7.

[20] G. Whitesides, ‘Microfluidics in Late Adolescence’, Jan. 10, 2018, *arXiv*: arXiv:1802.05595.

[21] F. C. Jammes and S. J. Maerkl, ‘How single-cell immunology is benefiting from microfluidic technologies’, *Microsyst Nanoeng*, vol. 6, no. 1, Art. no. 1, July 2020.

[22] M. Akbar, M. Restaino, and M. Agah, ‘Chip-scale gas chromatography: From injection through detection’, *Microsyst Nanoeng*, vol. 1, no. 1, Art. no. 1, Dec. 2015.

[23] D. Zhang, H. Bi, B. Liu, and L. Qiao, ‘Detection of Pathogenic Microorganisms by Microfluidics Based Analytical Methods’, *Anal. Chem.*, vol. 90, no. 9, pp. 5512–5520, May 2018.

[24] V. Ortseifen, M. Viefhues, L. Wobbe, and A. Grünberger, ‘Microfluidics for Biotechnology: Bridging Gaps to Foster Microfluidic Applications’, *Frontiers in Bioengineering and Biotechnology*, vol. 8, 2020, Accessed: July 21, 2022. [Online]. Available: https://www.frontiersin.org/articles/10.3389/fbioe.2020.589074

[25] D. J. B. Glenn M. Walker, ‘Physics and Applications of Microfluidics in Biology’. Accessed: July 21, 2022. [Online]. Available: https://www.annualreviews.org/doi/epdf/10.1146/annurev.bioeng.4.112601.125916

[26] A. Guenther and K. Jensen, ‘Multiphase microfluidics: From flow characteristics to chemical and materials synthesis’, *Lab on a chip*, vol. 6, pp. 1487–503, Jan. 2007.

[27] B. Lin and A. Levchenko, ‘Spatial Manipulation with Microfluidics’, *Front Bioeng Biotechnol*, vol. 3, p. 39, Apr. 2015.

[28] M. Gonidec and J. Puigmartí-Luis, ‘Continuous- versus Segmented-Flow Microfluidic Synthesis in Materials Science’, *Crystals*, vol. 9, no. 1, p. 12, Dec. 2018.

[29] L. Kim, Y.-C. Toh, J. Voldman, and H. Yu, ‘A practical guide to microfluidic perfusion culture of adherent mammalian cells’, *Lab Chip*, vol. 7, no. 6, pp. 681–694, May 2007.

[30] N. Shembekar, C. Chaipan, R. Utharala, and C. A. Merten, ‘Droplet-based microfluidics in drug discovery, transcriptomics and high-throughput molecular genetics’, *Lab Chip*, vol. 16, no. 8, Art. no. 8, Apr. 2016.

[31] I. Kobayashi, K. Uemura, and M. Nakajima, ‘Formulation of monodisperse emulsions using submicron-channel arrays’, *Colloids and Surfaces A: Physicochemical and Engineering Aspects*, vol. 296, no. 1, pp. 285–289, Mar. 2007.

[32] S. Sohrabi, N. Kassir, and M. K. Moraveji, ‘Droplet microfluidics: fundamentals and its advanced applications’, *RSC Adv.*, vol. 10, no. 46, pp. 27560–27574, July 2020.

[33] S. Huang, J. Connolly, A. Khlystov, and R. B. Fair, ‘Digital Microfluidics for the Detection of Selected Inorganic Ions in Aerosols’, *Sensors*, vol. 20, no. 5, Art. no. 5, Jan. 2020.

[34] M. J. Jebrail, M. S. Bartsch, and K. D. Patel, ‘Digital microfluidics: a versatile tool for applications in chemistry, biology and medicine’, *Lab Chip*, vol. 12, no. 14, pp. 2452–2463, June 2012.

[35] B. Yılmaz and F. Yılmaz, ‘Chapter 8 - Lab-on-a-Chip Technology and Its Applications’, in *Omics Technologies and Bio-Engineering*, D. Barh and V. Azevedo, Eds, Academic Press, 2018, pp. 145–153.

[36] D. Huh, B. D. Matthews, A. Mammoto, M. Montoya-Zavala, H. Yuan Hsin, and D. E. Ingber, ‘Reconstituting Organ-Level Lung Functions on a Chip’, *Science*, vol. 328, no. 5986, Art. no. 5986, June 2010.

[37] Q. Wu *et al.*, ‘Organ-on-a-chip: recent breakthroughs and future prospects’, *BioMedical Engineering OnLine*, vol. 19, no. 1, p. 9, Feb. 2020.

[38] Y. Quan *et al.*, ‘Organ-on-a-chip: the next generation platform for risk assessment of radiobiology’, *RSC Advances*, vol. 10, no. 65, pp. 39521–39530, 2020.

[39] A. Alrifaiy, O. Lindahl, and K. Ramser, ‘Polymer-Based Microfluidic Devices for Pharmacy, Biology and Tissue Engineering’, *Polymers*, vol. 4. July 03, 2012.

[40] G. Bruno *et al.*, ‘Unexpected behaviors in molecular transport through size-controlled nanochannels down to the ultra-nanoscale’, *Nat Commun*, vol. 9, no. 1, Art. no. 1, Apr. 2018.

[41] A. Mata, A. J. Fleischman, and S. Roy, ‘Characterization of Polydimethylsiloxane (PDMS) Properties for Biomedical Micro/Nanosystems’, *Biomed Microdevices*, vol. 7, no. 4, pp. 281–293, Dec. 2005.

[42] A. Sengupta, S. Herminghaus, and C. Bahr, ‘Liquid crystal microfluidics: Surface, elastic and viscous interactions at microscales’, *Liquid Crystals Reviews*, vol. 2, Sept. 2014.

[43] C. Iliescu, H. Taylor, M. Avram, J. Miao, and S. Franssila, ‘A practical guide for the fabrication of microfluidic devices using glass and silicon’, *Biomicrofluidics*, vol. 6, no. 1, pp. 016505-016505–16, Mar. 2012.

[44] M. E. Wilson *et al.*, ‘Fabrication of circular microfluidic channels by combining mechanical micromilling and soft lithography’, *Lab Chip*, vol. 11, no. 8, pp. 1550–1555, Apr. 2011.

[45] S. M. Scott and Z. Ali, ‘Fabrication Methods for Microfluidic Devices: An Overview’, *Micromachines (Basel)*, vol. 12, no. 3, p. 319, Mar. 2021.

[46] R. Su, F. Wang, and M. C. McAlpine, ‘3D printed microfluidics: advances in strategies, integration, and applications’, *Lab Chip*, vol. 23, no. 5, pp. 1279–1299, Mar. 2023.

[47] C. Soitu, C. Deroy, A. A. Castrejón-Pita, P. R. Cook, and E. J. Walsh, ‘Using Fluid Walls for Single-Cell Cloning Provides Assurance in Monoclonality’, *SLAS TECHNOLOGY: Translating Life Sciences Innovation*, vol. 25, no. 3, pp. 267–275, June 2020.

[48] A. Sapkota, ‘Serial Dilution- Definition, Formula, Calculator, Procedure, Uses’, Microbe Notes. Accessed: Nov. 15, 2022. [Online]. Available: https://microbenotes.com/serial-dilution/

[49] P. F. F. Dimond, ‘Single-Cell Cloning Remains a Challenge’, GEN - Genetic Engineering and Biotechnology News. Accessed: July 30, 2022. [Online]. Available: https://www.genengnews.com/magazine/322/single-cell-cloning-remains-a-challenge-2/

[50] A. Citri, Z. P. Pang, T. C. Sudhof, M. Wernig, and R. C. Malenka, ‘Comprehensive qPCR profiling of gene expression in single neuronal cells’, *Nat Protoc*, vol. 7, no. 1, pp. 118–127, Dec. 2011.

[51] S. P. Mathupala and A. E. Sloan, ‘An agarose-based cloning-ring anchoring method for isolation of viable cell clones’, *Biotechniques*, vol. 46, no. 4, pp. 305–307, Apr. 2009.

[52] P. Hu, W. Zhang, H. Xin, and G. Deng, ‘Single Cell Isolation and Analysis’, *Frontiers in Cell and Developmental Biology*, vol. 4, 2016, Accessed: July 21, 2022. [Online]. Available: https://www.frontiersin.org/articles/10.3389/fcell.2016.00116

[53] A. Gross, J. Schoendube, S. Zimmermann, M. Steeb, R. Zengerle, and P. Koltay, ‘Technologies for Single-Cell Isolation’, *Int J Mol Sci*, vol. 16, no. 8, pp. 16897–16919, July 2015.

[54] ‘Microfluidic chips for single-cell analysis and isolation’, uFluidix. Accessed: Nov. 15, 2022. [Online]. Available: https://www.ufluidix.com/microfluidics-applications/single-cell-analysis/

[55] W. Zhou *et al.*, ‘Microfluidics applications for high-throughput single cell sequencing’, *Journal of Nanobiotechnology*, vol. 19, no. 1, p. 312, Oct. 2021.

[56] V. Narayanamurthy, S. Nagarajan, A. Y. F. Khan, F. Samsuri, and T. M. Sridhar, ‘Microfluidic hydrodynamic trapping for single cell analysis: mechanisms, methods and applications’, *Anal. Methods*, vol. 9, no. 25, pp. 3751–3772, June 2017.

[57] E. Berthier, A. M. Dostie, U. N. Lee, J. Berthier, and A. B. Theberge, ‘Open Microfluidic Capillary Systems’, *Anal. Chem.*, vol. 91, no. 14, pp. 8739–8750, July 2019.

[58] S. Xing, R. S. Harake, and T. Pan, ‘Droplet-driven transports on superhydrophobic-patterned surface microfluidics’, *Lab on a Chip*, vol. 11, no. 21, pp. 3642–3648, 2011.

[59] J. J. Lee, J. Berthier, K. A. Brakke, A. M. Dostie, A. B. Theberge, and E. Berthier, ‘Droplet Behavior in Open Biphasic Microfluidics’, *Langmuir*, vol. 34, no. 18, pp. 5358–5366, May 2018.

[60] Q. Zhang, S. Feng, L. Lin, S. Mao, and J.-M. Lin, ‘Emerging open microfluidics for cell manipulation’, *Chem. Soc. Rev.*, vol. 50, no. 9, pp. 5333–5348, May 2021.

[61] J. H. Schrope *et al.*, ‘Confinement by Liquid-Liquid Interface Replicates In Vivo Neutrophil Deformations and Elicits Bleb-Based Migration’, *Advanced Science*, vol. 12, no. 21, p. 2414024, 2025.

[62] C. Li *et al.*, ‘Combining Top-Down and Bottom-Up: An Open Microfluidic Microtumor Model for Investigating Tumor Cell-ECM Interaction and Anti-Metastasis’, *Small*, vol. 21, no. 9, p. 2402499, 2025.

[63] J. Yu *et al.*, ‘Reconfigurable open microfluidics for studying the spatiotemporal dynamics of paracrine signalling’, *Nat Biomed Eng*, vol. 3, no. 10, pp. 830–841, Oct. 2019.

[64] T. E. de Groot, K. S. Veserat, E. Berthier, D. J. Beebe, and A. B. Theberge, ‘Surface-tension driven open microfluidic platform for hanging droplet culture’, *Lab on a Chip*, vol. 16, no. 2, pp. 334–344, 2016.

[65] G. M. Walker and D. J. Beebe, ‘A passive pumping method for microfluidic devices’, *Lab Chip*, vol. 2, no. 3, pp. 131–134, Aug. 2002.

[66] J. H. Schrope *et al.*, ‘Confinement by Liquid-Liquid Interface Replicates In Vivo Neutrophil Deformations and Elicits Bleb-Based Migration’, *Advanced Science*, vol. 12, no. 21, p. 2414024, 2025.

[67] Q. Chen, H. Zhai, D. J. Beebe, C. Li, and B. Wang, ‘Visualization-enhanced under-oil open microfluidic system for in situ characterization of multi-phase chemical reactions’, *Nat Commun*, vol. 15, no. 1, p. 1155, Feb. 2024.

[68] V. V. Berejnov, ‘Self-pinning protein-laden drops’, *Journal of Colloid and Interface Science*, vol. 322, no. 1, pp. 246–251, Jun. 2008.

[69] C. Soitu, N. Stovall-Kurtz, C. Deroy, A. A. Castrejón-Pita, P. R. Cook, and E. J. Walsh, ‘Jet-Printing Microfluidic Devices on Demand’, *Advanced Science*, vol. 7, no. 23, p. 2001854, 2020.

[70] A. Prastowo, P. R. Cook, and E. J. Walsh, ‘Biocompatibility of Sessile Drops as Chambers for Cell Culture’, in *2019 2nd International Conference on Bioinformatics, Biotechnology and Biomedical Engineering (BioMIC) - Bioinformatics and Biomedical Engineering*, Sept. 2019, pp. 1–5.

[71] A.-G. Niculescu, C. Chircov, A. C. Bîrcă, and A. M. Grumezescu, ‘Fabrication and Applications of Microfluidic Devices: A Review’, *International Journal of Molecular Sciences*, vol. 22, no. 4, p. 2011, Jan. 2021.

[72] J. Friend and L. Yeo, ‘Fabrication of microfluidic devices using polydimethylsiloxane’, *Biomicrofluidics*, vol. 4, no. 2, p. 026502, Mar. 2010.

[73] N. M. Oliveira *et al.*, ‘Suicidal chemotaxis in bacteria’, *Nat Commun*, vol. 13, no. 1, p. 7608, Dec. 2022.

[74] C. Soitu *et al*., 'Creating wounds in cell monolayers using micro-jets.' *Biomicrofluidics*, vol. 15, Feb. 2021.

[75] S. N. Calver, E. A. Gaffney, E. J. Walsh, W. M. Durham, and J. M. Oliver, ‘On the thin-film asymptotics of surface tension driven microfluidics’, *Journal of Fluid Mechanics*, vol. 901, Oct. 2020.

[76] C. Deroy, N. Stovall-Kurtz, F. Nebuloni, C. Soitu, P. Cook, and E. Walsh, 'Predicting flows through microfluidic circuits with fluid walls', Microsystems & Nanoengineering, vol. 7, Dec. 2021.

[77] A. Yusof *et al.*, 'Inkjet-like printing of single-cells', *Lab Chip*, vol. 11, no. 14, pp. 2447–2454, Jun. 2011.

[78] F. Stumpf *et al.*, 'Single-cell PCR of genomic DNA enabled by automated single-cell printing for cell isolation', *Biosensors and Bioelectronics*, vol. 69, pp. 301–306, Jul. 2015.

[79] Y. Wang, X. Wang, T. Pan, B. Li, and J. Chu, 'Label-free single-cell isolation enabled by microfluidic impact printing and real-time cellular recognition', *Lab Chip*, vol. 21, no. 19, pp. 3695–3706, Sep. 2021.

[80] V. Tejwani, M. Chaudhari, T. Rai, and S. T. Sharfstein, 'High-throughput and automation advances for accelerating single-cell cloning, monoclonality and early phase clone screening steps in mammalian cell line development for biologics production', *Biotechnology Progress*, vol. 37, no. 6, p. e3208, 2021.

[81] J. Riba, J. Schoendube, S. Zimmermann, P. Koltay, and R. Zengerle, 'Single-cell dispensing and "real-time" cell classification using convolutional neural networks for higher efficiency in single-cell cloning', *Sci Rep*, vol. 10, no. 1, p. 1193, Jan. 2020.

[82] M. Yim and D. Shaw, 'Achieving greater efficiency and higher confidence in single-cell cloning by combining cell printing and plate imaging technologies', *Biotechnology Progress*, vol. 34, no. 6, pp. 1454–1459, 2018.

[83] F. Sala, C. Ficorella, R. Osellame, J. A. Käs, and R. Martínez Vázquez, 'Microfluidic Lab-on-a-Chip for Studies of Cell Migration under Spatial Confinement', *Biosensors (Basel)*, vol. 12, no. 8, p. 604, Aug. 2022.

[84] C. L. Yankaskas *et al.*, 'A microfluidic assay for the quantification of the metastatic propensity of breast cancer specimens', *Nat Biomed Eng*, vol. 3, no. 6, pp. 452–465, Jun. 2019.

[85] S. Ding *et al.*, ‘Sorting and characterization of cancer cells with different migration phenotypes using a microfluidic platform’, *Sensors and Actuators B: Chemical*, vol. 440, p. 137875, Oct. 2025.

[86] N. Gural and D. Irimia, ‘Microfluidic devices for precise measurements of cell directionality reveal a role for glutamine during cell migration’, *Sci Rep*, vol. 13, no. 1, p. 23032, Dec. 2023.

[87] Y.-C. Chen *et al.*, ‘Functional Isolation of Tumor-Initiating Cells using Microfluidic-Based Migration Identifies Phosphatidylserine Decarboxylase as a Key Regulator’, *Sci Rep*, vol. 8, no. 1, p. 244, Jan. 2018.

[88] X. Tang *et al.*, ‘Effects of substrate stiffness on the viscoelasticity and migration of prostate cancer cells examined by atomic force microscopy’, *Beilstein J Nanotechnol*, vol. 13, pp. 560–569, Jun. 2022.

[89] S. P. H. Chiang, R. M. Cabrera, and J. E. Segall, ‘Tumor cell intravasation’, *Am J Physiol Cell Physiol*, vol. 311, no. 1, pp. C1–C14, Jul. 2016.

[90] S. G. Baldursdottir, M. S. Fullerton, S. H. Nielsen, and L. Jorgensen, ‘Adsorption of proteins at the oil/water interface—Observation of protein adsorption by interfacial shear stress measurements’, *Colloids and Surfaces B: Biointerfaces*, vol. 79, no. 1, pp. 41–46, Aug. 2010.

[91] C. J. Beverung, C. J. Radke, and H. W. Blanch, ‘Protein adsorption at the oil/water interface: characterization of adsorption kinetics by dynamic interfacial tension measurements’, *Biophysical Chemistry*, vol. 81, no. 1, pp. 59–80, Sep. 1999.

[92] F. Possmayer, Y. Y. Zuo, R. A. W. Veldhuizen, and N. O. Petersen, ‘Pulmonary Surfactant: A Mighty Thin Film’, *Chem. Rev.*, vol. 123, no. 23, pp. 13209–13290, Dec. 2023.

[93] A. Gokaltun, M. L. Yarmush, A. Asatekin, and O. B. Usta, ‘Recent advances in nonbiofouling PDMS surface modification strategies applicable to microfluidic technology’, *Technology (Singap World Sci)*, vol. 5, no. 1, pp. 1–12, Mar. 2017.

[94] D. Klingelhöfer, M. Braun, D.A. Groneberg, D. Brüggmann. ‘The “forever” per- and polyfluoroalkyl substances (PFAS): A critical accounting of global research on a major threat under changing regulations.’ *Chemosphere*, vol. 354, 141694, April. 2024.

[95] J. G. Riess and M. P. Krafft, ‘Fluorinated materials for in vivo oxygen transport (blood substitutes), diagnosis and drug delivery’, *Biomaterials*, vol. 19, no. 16, pp. 1529–1539, Aug. 1998.

[96] J. S. Greenspan, M. R. Wolfson, S. D. Rubenstein, and T. H. Shaffer, ‘Liquid ventilation of human preterm neonates’, *The Journal of Pediatrics*, vol. 117, no. 1, Part 1, pp. 106–111, Jul. 1990.

[97] C. Li *et al.*, ‘Under oil open-channel microfluidics empowered by exclusive liquid repellency’, *Science Advances*, vol. 6, no. 16, Art. no. 16, Apr. 2020.

[98] S. Feng, S. Mao, J. Dou, W. Li, H. Li, and J.-M. Lin, ‘An open-space microfluidic chip with fluid walls for online detection of VEGF via rolling circle amplification’, *Chem. Sci.*, vol. 10, no. 37, pp. 8571–8576, Sept. 2019.